STRATOSPHERE TROPOSPHERE EXCHANGE AND ITS INFLUENCE ON SURFACE OZONE CONCENTRATIONS IN THE LOWER FRASER VALLEY

by

Paul E. Bovis

BSc., University of British Columbia, 2001

A THESIS SUBMITTED IN PARTIAL FULFILMENT OF
THE REQUIREMENTS FOR THE DEGREE OF

MASTER OF SCIENCE

in

THE FACULTY OF GRADUATE STUDIES

(Atmospheric Science)

We accept this thesis as conforming
to the required standard

THE UNIVERSITY OF BRITISH COLUMBIA

August 28, 2003

In presenting this thesis in partial fulfillment for the requirements for an advanced degree at the University of British Columbia, I agree that the library shall make it freely available for reference and study. I further agree that permission for extensive copying of this thesis for scholarly purposes may be granted by the head of my department or by his or her representatives. It is understood that copying and publication of this thesis for financial gain shall not be allowed without my written permission.

Atmospheric Science

The University of British Columbia
Vancouver, Canada

Date August 29, 2003

Abstract

^{7}Be activity concentration data collected at the University of British Columbia and ozone data collected throughout the Lower Fraser Valley (LFV), British Columbia, Canada from April 1996 – March 2001 were used to investigate the frequency, magnitude and source regions of possible stratosphere-troposphere exchange (STE) episodes that may have influenced surface ozone concentrations in the LFV. With the aid of synoptic and back trajectory analysis, it was determined that the bulk of the intruded stratospheric ozone, which resulted in elevated surface ozone concentrations in the LFV, originated within intense Eastern Asian/Western Pacific cutoff low pressure systems and troughs. This stratospheric air was then transported by the synoptic scale flow to the LFV region where it descended to the surface via synoptic scale high pressure systems. During these STE episodes, it was estimated that stratospheric ozone concentrations of up to 40 ppb (depending on the season and time of day) were contributing to the total surface ozone concentrations in the LFV. Since anthropogenic ozone production is already a major concern of air quality management programs in the LFV, this stratospheric contribution cannot be ignored when decisions are being made with regards to surface ozone reduction initiatives in this region.

Table of Contents

Abstract ii
Table of Contents iii
List of Tables v
List of Figures vi
Acknowledgements ix
1 Introduction 1
1.1 In-Situ Aircraft Studies 4
1.2 High Altitude Studies 5
1.3 Sea Level Studies 6
1.4 Research Goals 8

2 Data 10
2.1 ^{7}Be in the Atmosphere 10
2.1.1 Radionuclide Measurements as Part of the CTBT 13
2.1.2 ^{7}Be Measurements in Vancouver, Canada 14
2.2 Ozone 17
2.2.1 Ozone Formation in the Stratosphere 17
2.2.2 Ozone Formation in the Troposphere 19
2.2.3 The GVRD Air Quality Monitoring Network 19
2.3 Temperature and Precipitation 25
2.4 Satellite Data 25

3 Data Analysis 25
3.1 80th Percentile Algorithm 26
3.1.1 80th Percentile Algorithm Using All Data 27
3.1.2 80th Percentile Algorithm Excluding June to August 33
3.1.3 80th Percentile Algorithm Excluding May to September 35
3.1.4 Disadvantages of the 80th Percentile Algorithm 35
3.2 ^{7}Be Only Algorithm 36
3.3 Summary 47

4 Trajectories and Case Studies 50
4.1 Previous Research 51
4.2 Trajectory Models and Procedures Used in the Current Research 54
4.2.1 HYSPLIT 54
4.2.2 CANERM 54
4.2.3 Trajectory Model Procedure 55
4.3 Case Studies 55
4.3.1 Case Study #1 – 28 October 1996 – 31 October 1996 57
4.3.1.1 Synoptic Overview 57
4.3.1.2 Surface O_3 and ^{7}Be Concentrations and Temperature in the LFV 58
4.3.1.3 Back Trajectory Analysis 63
4.3.2 Case Study #2 – 20 December 1996 – 01 January 1997 65
4.3.2.1 Synoptic Overview 65
4.3.2.2 Surface O_3 and ^{7}Be Concentrations and Temperature in the LFV 70
4.3.2.3 Back Trajectory Analysis 71
4.3.3 Case Study #3 – 22 January 1997 – 29 January 1997 73
4.3.3.1 Synoptic Overview 73
4.3.3.2 Surface O_3 and ^{7}Be Concentrations and Temperature in the LFV 79
4.3.3.3 Back Trajectory Analysis 80
4.3.4 Case Study #4 – 05 January 2001 – 11 January 2001 83

4.3.4.1 Synoptic Overview 83
4.3.4.2 Surface O_3 and ^7Be Concentrations and Temperature in the LFV 91
4.3.4.3 Back Trajectory Analysis 92

5 Discussion 96
5.1 Possible Source Regions of Ozone 96
5.2 General Trajectory Error – A Brief Discussion 98
5.3 CANERM and HYSPLIT Model Comparison 100
5.4 Precipitation and its Influence on ^7Be Concentrations 106

6 Conclusion 108
6.1 Future Research 111

7 References 113

List of Tables

Table 1 - Episodes based on the 80th percentile detection algorithm (all data).
Table 2 - Episodes based on the 80th percentile detection algorithm (excluding June - August).
Table 3 - Episodes based on the 80th percentile detection algorithm (excluding May-September).
Table 4 - Episodes based on the ^{7}Be detection algorithm.
Table 5 - GVRD Air Quality Monitoring stations used in the hourly ozone concentration graphs in Figure 16.

List of Figures

Figure 1 - A modeled north-south section through the atmosphere showing the surfaces of constant ^{7}Be production.

Figure 2 - The modeled vertical concentration profiles of ^{7}Be at 45°N for settling velocities (1) $\upsilon_s = 0$ ms^{-1}, (2) $\upsilon_s = 0.02$ ms^{-1} and (3) $\upsilon_s = 1$ ms^{-1}.

Figure 3 - Map of the Comprehensive Nuclear Test Ban Treaty Internaional Montoring System radionuclide network.

Figure 4 - Daily ^{7}Be activity concentrations measured at the CTBTO IMS station CA002 from 9 April 1996 - 12 March 2002.

Figure 5 - Cumulative distribution of the ^{7}Be activity concentrations at the CTBTO IMS station CA002 during the period 9 April 1996 - 12 March 2002.

Figure 6 - Monthly average ^{7}Be concentration at the CTBTO IMS station CA002 during the period 9 April 1996 - 12 March 2002.

Figure 7 - Average number of days in a month in which ^{7}Be activity concentration exceeds the 80th percentile at the CTBTO IMS station CA002 during the period 9 April 1996 - 12 March 2002.

Figure 8 - Chemical reactions of Chapman's mechanism, a static pure oxygen photochemical steady state model.

Figure 9 - A generic sequence of reactions for the loss of odd oxygen by way of a catalytic cycle.

Figure 10 - Observed (solid line) and calculated (dashed line) vertical concentration profiles of ozone as a function of latitude in the Northern Hemisphere for mid-spring.

Figure 11 - Greater Vancouver Regional District Continuous Air Quality Monitoring Network.

Figure 12 - Composite diurnal ozone concentration graphs for Downtown Vancouver (T001), Kitsilano (T002), Chilliwack Airport (T012), Surrey East (T015), Richmond (T017), Langley Central (T027), Hope Airport (T029) and Port Coquitlam North (T032).

Figure 13 - ^{7}Be activity concentration, average daily maximum temperature, average daily maximum ozone concentration and coefficient of variance of ozone for 3 May 1996 – 22 May 1996, 13 July 1997 – 25 July 1997, 13 April 2000 – 25 April 2000 and 11 February 2001 – 20 February 2001 from the 80th percentile detection algorithm (all data).

Figure 14 - Average number of days in a month in which the average daily maximum temperature exceeded 20°C in the Lower Fraser Valley during the period 10 April 1996 – 31 December 2001.

Figure 15 - ^{7}Be activity concentration, average daily maximum temperature, average daily maximum ozone concentration and coefficient of variance of ozone for 25 October 1996 – 5 November 1996, 21 December 1996– 1 January 1997, 22 January 1997 – 1 February 1997 and 4 January 2001 – 12 January 2001 from the ^{7}Be only detection algorithm.

Figure 16 - Hourly ozone concentrations measured at Kitsilano, Richmond South, Port Coquitlam North and Downtown Vancouver urban air quality monitoring stations and Hope Airport, Chilliwack Airport, Surrey East and Langley Central rural air quality monitoring stations in the Greater Vancouver Regional District for 28 October 1996 – 1 November 1996, 20 December 1996 – 7 January 1997, 21 January 197 – 28 January 1997 and 6 January 2001 – 9 January 2001.
Figure 17 - Hourly ozone concentrations measured Hope Airport, Chilliwack Airport, Surrey East and Langley Central rural air quality monitoring stations in the Greater Vancouver Regional District for 20 July 1996 – 29 July 1996.
Figure 18 - Hourly ozone concentrations measured Hope Airport, Chilliwack Airport, Surrey East and Langley Central rural air quality monitoring stations in the Greater Vancouver Regional District for 2 November 1998 – 11 November 1998.
Figure 19 - Total number of days in a month in which both the daily ^{7}Be activity concentration and the average daily maximum ozone concentration exceeded the 80^{th} percentile (all data) at the CTBTO IMS station CA002 during the period 9 April 1996 - 12 March 2002.
Figure 20 - Total number of days in a month in which both the daily ^{7}Be activity concentration and the average daily maximum ozone concentration exceeded the 80^{th} percentile (excluding June - August) at the CTBTO IMS station CA002 during the period 9 April 1996 - 12 March 2002.
Figure 21 - Total number of days in a month in which both the daily ^{7}Be activity concentration and the average daily maximum ozone concentration exceeded the 80^{th} percentile (excluding May - September) at the CTBTO IMS station CA002 during the period 9 April 1996 - 12 March 2002.
Figure 22 - Total number of days in a month in which the daily ^{7}Be activity concentration exceeded 6000 μBqm^{-3} at the CTBTO IMS station CA002 during the period 9 April 1996 - 12 March 2002.
Figure 23 - 500 mb geopotential chart for 25 October 1996 at 1800 UTC.
Figure 24 - 250 mb geopotential chart for 25 October 1996 at 1800 UTC.
Figure 25 - Surface isobaric chart for 28 October 1996 at 0000 UTC.
Figure 26 - Three dimensional back trajectories arriving over the LFV area on 31 October 1996 at 0600 UTC using the CANERM model.
Figure 27 - 500 mb geopotential chart for 23 December 1996 at 0600 UTC.
Figure 28 - 250 mb geopotential chart for 23 December 1996 at 0600 UTC.
Figure 29 - Surface isobaric chart for 28 December 1996 at 1800 UTC.
Figure 30 - Three dimensional back trajectories arriving over the LFV area on 26 December 1996 at 1200 UTC using the CANERM model.
Figure 31 - 500 mb geopotential chart for 20 January 1997 at 0600 UTC.
Figure 32 - Surface isobaric chart for 18 January 1997 at 1800 UTC.
Figure 33 - Surface isobaric chart for 25 January 1997 at 1800 UTC.

Figure 34 - Three dimensional back trajectories arriving over the LFV area on 23 January 1997 at 0000 UTC using the CANERM model.
Figure 35 - Three dimensional back trajectories arriving over the LFV area on 23 January 1997 at 1800 UTC using the CANERM model.
Figure 36 - Three dimensional back trajectories arriving over the LFV area on 26 January 1997 at 1200 UTC using the CANERM model.
Figure 37 - 500 mb geopotential chart for 1 January 2001 at 0000 UTC.
Figure 38 - 250 mb geopotential chart for 2 January 2001 at 1200 UTC.
Figure 39 - 500 mb geopotential chart for 7 January 2001 at 1200 UTC.
Figure 40 - Surface isobaric chart for 1 January 2001 at 0000 UTC.
Figure 41 - Surface isobaric chart for 6 January 2001 at 1200 UTC.
Figure 42 - Three dimensional back trajectories arriving over the LFV area on 6 January 2001 at 1800 UTC using the CANERM model.
Figure 43 - Three dimensional back trajectories arriving over the LFV area on 7 January 2001 at 1800 UTC using the CANERM model.
Figure 44 - GOES water vapor satellite image for 1 January 2001 at 0000 UTC.
Figure 45 - Possible stratospheric and tropospheric source regions of ozone that arrived in the LFV during the four case studies in Section 4.3.
Figure 46 - Absolute latitudinal, longitudinal and height differences between the CANERM and HYSPLIT models for back trajectory runs starting at 100 m a.g.l, 500 m a.g.l. and 1000 m a.g.l. over the LFV.
Figure 47 - Daily ^{7}Be activity concentrations measured at the CTBTO IMS station CA002 and total daily precipitation measured at Vancouver International Airport during October 1996.
Figure 48 - Daily 7Be activity concentrations measured at the CTBTO IMS station CA002 and total daily precipitation measured at Vancouver International Airport during August 1997.

Acknowledgements

I would like to thank all of those who provided me with funding for the current research. Firstly, I would like to thank my supervisor, Dr. Douw Steyn, who provided me with funds from the National Science and Engineering Research Council (NSERC) and the Canadian Foundation for Climate and Atmospheric Sciences (CFCAS). I would also like to thank the Radiation Protection Bureau (RPB) at Health Canada for ^{7}Be data and additional funding. I am also grateful to Ken Reid at the Air Quality Department of the Greater Vancouver Regional District (GVRD) for the ozone data and the Environment Canada (EC) Meteorological Service of Canada's Pacific Yukon Region and Canadian Meteorologial Center offices for supplying me with temperature and precipitation data for Abbotsford and Vancouver International Airports and the meteorological back trajectory data. During the course of my research I had the opportunity to share research ideas and receive advice from a number of people. They are, in no particular order: Dr. Kurt Ungar, Dr. Bliss Tracy and Sonia Johnson at RPB, Dr. Douw Steyn, Dr. David Measday and Dr. Alberto Martilli at UBC, Rene Servranckx and Michel Jean at the EC Canadian Meteorological Center in Dorval, PQ. During the darker climbs, I would like to thank my parents, my girlfriend, Sara and my housemates, who tolerated me and offered me kind words of encouragment.

1. Introduction

Ozone plays an important dual role in the Earth's atmosphere. In the stratosphere, the ozone layer protects animal and plant life on the Earth's surface by absorbing shortwave electromagnetic radiation in the 0.2-0.4 μm wavelength range. Without the shielding effect of the stratospheric ozone layer, skin cancer, amongst other diseases, would increase. In the troposphere however, ozone has a much more sinister effect. Produced through a variety of precursor chemical species, both anthropogenic and natural in origin, tropospheric ozone, in sufficiently high concentrations, can cause lung damage, coughing, nausea, pulmonary congestion and can act as an eye irritant (NRC, 1992). Tropospheric ozone can also be harmful to plant life and crops by destroying a plant's leaves, hindering photosynthesis and slowly "starving" the plant until it eventually dies (NRC, 1992).

Ozone in the troposphere has several sources, both natural and anthropogenic. The main precursor pollutants that eventually react in the presence of shortwave solar radiation and high temperatures to form tropospheric ozone are volatile organic chemicals (VOC) and oxides of nitrogen, especially NO and NO_2, denoted as NO_x. The largest sources of these precursor pollutants in large urban areas are anthropogenic and include industrial and commercial facilities, motor vehicles and power plants. Some lesser natural sources include lightning, biomass burning and soil.

Tropospheric ozone can also originate from the stratosphere. During intense low-pressure synoptic systems and thunderstorms, ozone from the stratosphere can pass through the tropopause into the troposphere (Johnson and Viezee, 1981). This ozone can then be transported horizontally and vertically to the surface, thereby adding to the anthropogenic ground-level ozone concentration.

Recently, studies have shown that sources of tropospheric ozone are larger than its sinks (NRC, 1992). Janach (1989) showed that the average annual ozone concentration over Europe has increased by 1-2% over the past 30 years. Most of this increase can be attributed to photochemically produced ozone. The various sinks for tropospheric ozone include irreversible transport into the stratosphere, dry deposition to vegetation, soils and oceans, scavenging by NO_x and wet transformation in clouds (NRC, 1992).

Elevated tropospheric ozone concentrations, especially downwind from highly populated urban areas were identified as a human health and crop degradation problem as early as the 1940's when vegetable crops showed signs of damage in the Los Angeles basin. In later studies published in the 1950's, photochemically produced ozone was identified as the main contributor to crop damage within the basin (Haagen-Smit *et al.*, 1951, 1953, Haagen-Smit 1952, Haagen-Smit and Fox, 1954, 1955, 1956). Over the next 30 years, many tropospheric ozone studies were conducted worldwide (Steyn *et al.*, 1997, Gusten *et al.,* 1988, Juarez *et al.,* 1994, Pont and Fontan, 2000, Rao *et al.,* 1991). Some of the major subjects included the reaction mechanisms of photochemical pollution (Mayer, 1999, Seinfeld, 1986, Stewart *et al.*, 1977) and air pollution modelling (Tulet *et al.,* 2000, Morison *et al.*, 2002, Zannetti, 1990).

Although most of the tropospheric ozone originated from anthropogenic precursor pollutants (Steyn *et al.,* 1997), there has been a recent interest in the component of ozone that was derived from natural sources, most importantly from the stratosphere (Danielsen, 1968, Davies and Schuepbach, 1994, Stohl *et al.,* 2000). Ozone can be injected into the troposphere via stratosphere-troposphere exchange (Johnson and Viezee, 1981, Cho *et al.,* 1999). The main mechanism of this exchange is tropopause

folding which involves an isentropic down folding of the tropopause which occurs behind upper or lower frontal surfaces (Danielsen, 1968). In order for irreversible exchange of ozone-rich stratospheric air within the fold to occur, turbulent mixing, usually in the form of Kelvin-Helmholtz waves, must occur on the lateral or bottom sides of the fold (Cho *et al.,* 1999). Once in the troposphere, stratospheric ozone can be vertically transported to the surface either through large-scale convection (i.e thunderstorms) (Tremblay and Servranckx, 1993) or subsidence (i.e. synoptic high pressure systems) (Kato *et al.,* 1990). Alternately, if the bottom side of the fold penetrates deep into the troposphere so that it impinges on the surface, ozone can be directly transferred to the ground. This particular process will increase the concentration of ground level ozone dramatically, but this direct transfer process usually occurs in high altitude locations only (i.e. mountainous regions) (Schuepbach *et al.,* 1999, Stohl *et al,* 2000, Bonasoni *et al,* 1999).

In order for researchers to determine the magnitude of the stratospheric ozone contribution to ground level ozone concentrations, some sort of stratospheric tracer, measurable at the surface, must be utilized. Over the years, many tracers have been used including relative humidity (Stohl *et al.* 2000), ^{90}Sr from American stratospheric nuclear tests (Danielsen 1968, Danielsen *et al.* 1970, 1977), and potential temperature (Haagenson, 1981). Ozone itself cannot be used as a tracer because it is not produced exclusively in the stratosphere. High surface ozone concentrations could be anthropogenic and/or natural in origin even in remote locations. It is the previously mentioned tracers that reveal the stratospheric source. In recent years, the cosmogenic radionuclide, ^{7}Be, has emerged as the primary stratospheric tracer in stratosphere-troposphere exchange (STE) studies (Murao *et al.,* 1990, Tremblay and Servranckx, 1993, Stohl *et al.,* 2000, Stohl and Trickl, 1999, Bonasoni *et al,* 1999).

Its usefulness as a tracer of STE stems from the fact that it is produced in the upper troposphere and lower stratosphere where tropopause folding occurs. Further characteristics of ^{7}Be will be covered more thoroughly in Section 2.1.1.

The bulk of studies involving STE have been conducted either in mountainous regions around the world, most importantly in the Swiss Alps, or in-situ via aircraft measurements because air of stratospheric origin has had little chance to dilute at these altitudes. The following two sections summarize several important papers, published over the past 30 years, which greatly aided the research community in this field.

1.1 In Situ Aircraft Studies

Danielson *et al.* (1970) were among the first researchers to study the distribution of radioactivity and ozone associated with tropopause folding. They were also the first researchers to show that there was a positive relationship between radioactivity and ozone originating from the stratosphere. Their measurements were carried out by fitting four RB-57 aircraft of the US Air Weather Service (now known as the National Weather Service) with radioactivity and ozone sensors and flying througha tropopaus foldbetween Albuquerque, NM and the southwest corner of Wyoming. It was reported that favourable meteorological conditions in which to observe a tropopause fold were an intensifying upper-level trough over western North America, a ridge over the Gulf of Alaska and a strong upper level jet that is advancing around the ridge. They also concluded that velocity shear produced by gravity waves plays an important, if not primary role in the mixing of stratospheric air into the troposphere.

Johnson and Viezee (1981) investigated the frequency and extent of stratospheric intrusions in the Central U.S.A. during the spring and fall of 1978 using in-situ aircraft measurements. At least during measurement flights, stratospheric ozone

intrusions were observed in nearly every trough regardless of its intensity. The maximum ozone concentrations in the intrusions and the trough intensity as characterized by the maximum wind speed at 300 mb were found to be highly correlated. During these intrusion events, peak ozone concentrations, between 240-400 ppb, were observed between 6-8 km a.s.l. The ozone concentrations then decreased to 100-200 ppb at lower levels as a result of turbulent mixing processes causing dilution. Measured ozone concentrations during spring were almost twice as high as those measured in the fall. These intrusions were generally 100-300 km wide in the crosswind direction, several hundred kilometres long and could penetrate as deep as the top of the boundary layer. They postulated that possible mechanisms for downward transport within the boundary layer include normal convective mixing, organized convection associated with cloud and precipitation processes and organized downward motion within frontal zones.

1.2 High Altitude Studies

Stohl *et al.* (2000) analyzed climatological data of ^{7}Be and ozone to characterize the frequency of stratospheric intrusions at three high altitude stations in the Alps and Apennines. These stations were Jungfraujoch, Zugspitze and Sonnblick. The data sets indicate that the absolute frequency of stratospheric intrusions depended on the threshold values that one sets for ^{7}Be, ozone and humidity. However, they noted that the relative shape of the annual cycle of stratospheric intrusions is fairly insensitive to the variations in the threshold values. Sonnblick and Zugspitze showed the highest stratospheric intrusion frequency in October with a secondary maximum in January and February and a deep minimum in summer. No clear seasonal stratospheric intrusion patten could be found in the Jungfraujoch data.

Zanis *et al.* (1999) investigated some of the factors affecting ^{7}Be at Jungfraujoch

in the Swiss Alps. They used a data set spanning 4 April 1996 – 1 January 1997. It was found that downward transport associated with an upper ridge and a high tropopause is a significant controlling mechanism for high ^{7}Be activity concentrations (Bqm^{-3}) at Jungfraujoch. However, they did state that this direct process is not the only way that stratospheric ^{7}Be and ozone were introduced to Jungfraujoch. An indirect multi-step mechanism might also be responsible. Zanis *et al* (1999) outline such a case that occurred from 16-23 July 1996 where it was concluded that stratospheric ozone that reached the station had originated from an STE event over northern Europe. The air that originated from this event was advected southward to Switzerland and eventually subsided to the surface.

These studies outlined not only the shape and frequency of stratospheric intrusions, but also the favourable meteorological conditions in which these intrusions occur. These studies also describe the vertical and horizontal transport mechanisms required for stratospherically intruded ozone to reach the surface.

1.3 Sea Level Studies

Although less prevalent in the literature, sea level case studies have also been conducted. Although the stratospheric signature of the intruded air is more dilute at altitudes close to sea level, it can be measured especially during the winter months when anthropogenically derived ozone production is at a minimum. ^{7}Be is a useful measurement tool in these studies, because the other stratospheric tracers have usually become too dilute to identify the air mass as partly stratospheric in origin.

Lamb (1977) investigated one case in Santa Rosa, CA, on 19 November 1977 in which that city's air quality monitoring station recorded five consecutive hours of ozone concentrations above the National Ambient Air Quality Standard of 120 ppb. During this time, the highest hourly average was 230 ppb. Lamb (1977) gives three

possible reasons for such high values. The first was instrument malfunction, but after some testing, this hypothesis was ruled out. The second was that these high oxidant concentrations originated from anthropogenic sources. The fact that this event occurred before sunrise rules out the possibility of photochemical processes unless the ozone was transported to the region. After model trajectory analysis, it was concluded that anthropogenic ozone was not responsible for this episode. The third possibility was that stratospheric ozone had made its way to the surface via STE. Through isentropic and isothermal analysis, Lamb (1977) was able to compute the vertical velocities and determined that there was descent along a frontal zone that passed over the area. Further evidence, including potential vorticity and mixing ratio profiles, suggested that this air, and thus the ozone, was indeed of stratospheric origin.

Chung and Dann (1985) document a rare high ozone concentration episode that occurred on 26-28 December 1980 at Regina, Canada in which one hour average oone concentrations ranged from 138-228 ppb. The meteorological conditions at this site were similar to other cases in which stratospheric intrusions occurred. They were :

- The presence of a quasi-stationary front with the formation of a lee cyclone east of the Rocky Mountains.
- The approach of an upper-level trough.
- The passing of a warm front over the area after a cold spell followed by a rapid temperature drop associated with the passing of a cold front.
- Wind shifts (presumably caused by the passing of the warm and cold fronts).
- The presence of a strong jet-stream maximum at all levels from 850 mb to 250 mb over southern Saskatchewan.

The occurrence of such an episode is rare for the region even though the meteorological conditions are frequently favourable for such stratospheric intrusion events.

The study conducted by Tremblay and Servranckx (1993) was one of the few studies, conducted near sea level, that measured ^{7}Be and ozone simultaneously. The

purpose of the study was to determine what fraction of the total ozone measured in the Montreal, Canada area originated from the stratosphere. On 27-28 June 1991, high ^{7}Be activity concentrations were recorded which suggested that some of the ozone at the surface was of stratospheric origin. During these two days, two thunderstorms with cloud tops reaching the lower stratosphere hit the southwestern portion of Quebec. Davies and Schuepbach (1994) suggested that downdrafts in thunderstorms could be a possible mechanism for the transport of ozone from the stratosphere to the surface. Tremblay and Servranckx (1993) reported that the average annual ^{7}Be activity in Montreal is about 3400 μBqm^{-3}. The values of ^{7}Be on 27-28 July 1991 were 5600 μBqm^{-3} and 6500 μBqm^{-3} respectively. This suggested that some of the ozone measured at the Montreal station, located at the top of the Atmospheric Environment Service building, originated from the stratosphere. They concluded that this stratospheric ozone could have acounted for 18% (or 9 ppb by volume) of the total ozone measured at the surface during the measurement period.

1.4 Research Goals

Although several studies have used ^{7}Be data to investigate single, high ozone cases (Murao *et al.,* 1990, Tremblay and Servranckx, 1993, Bonasoni *et al.,* 2000), very little attention has been paid to an examination of the climatology of both species (^{7}Be and O_3) simultaneously. This was mostly due to non-existent or at best sporadic ^{7}Be measurements. Since the implementation of the Comprehensive Nuclear Test Ban Treaty (CTBT) (see Section 2.1.1), ^{7}Be measurements are now readily available in many locations worldwide. The current research will make use of ^{7}Be data collected at a CTBT radionuclide monitoring station so that, in conjunction with a regional ozone monitoring network, cases in which stratospheric ozone is believed to

have had an influence on ground level ozone concentrations, may be identified and analysed.

The current research utilizes data collected in the Lower Fraser Valley (LFV) in southwestern British Columbia, Canada. It has long been known that this region suffers from a moderately acute ozone pollution problem (Steyn *et al.*, 1997). Although most of the ozone originates from anthropogenic precursor emissions, a lesser, but certainly not negligible contribution may b originating from the stratosphere. This stratospheric contribution will be the focus of the current research.

The goals of the current research are:

- To identify episodes, utilizing extensive ^{7}Be and ozone data sets, in which stratospheric ozone, via STE, contributes to the ground level ozone concentrations in the LFV.
- To identify source regions of stratospheric ozone which influences ground level ozone concentrations in the LFV. Two Lagrangian trajectory models, the Canadian Emergency Response Model (CANERM) and the NOAA Air Research Laboratories Hybrid Single Particle Lagrangian Integrated Trajectory model (HYSPLIT) will be utilized to determine not only source regions, but also the transport pathways of this stratospherically intruded ozone from the time of intrusion to the time of arrival in the LFV.
- To select four episodes from the identified stratospheric episodes and perform a detailed analysis to determine the various synoptic conditions necessary not only for STE, but also for the vertical and horizontal transport to the LFV.
- To qualitatively determine how precipitation affects ^{7}Be concentrations in the LFV.

The ^{7}Be, ozone and temperature data sets for the current research span the period 10 April 1996 to 12 March 2002. The CTBT radionuclide station at which ^{7}Be is measured is located at the University of British Columbia (Figure 11). Ozone concentrations are measured at several stations which are part of the Greater Vancouver Regional District air quality monitoring network (Figure 11). Other data such as 300 mb and 500 mb geopotential height charts, surface pressure charts, precipitation and infrared and water vapour satellite images will be utilized where possible during the case studies as they are not available continuously throughout the study period.

2. Data

2.1 ^{7}Be in the Atmosphere

Early stratosphere-troposphere exchange research utilized fissionogenic radionuclides as stratospheric tracers, most notably ^{90}Sr and ^{137}Cs (Danielsen, 1968). These radionuclides were products of nuclear tests that were conducted both in the atmosphere and on the ground. These radionuclides were injected into the stratosphere during a nuclear blast in the case of ground tests or were generated in situ in the case of stratospheric tests. In time, ^{90}Sr and ^{137}Cs concentrations in the atmosphere and in the stratosphere in particular began to decrease, either because of dry deposition to the earth's surface, scavenging due to precipitation, half life decay or ceased nuclear testing (Ishikawa *et al.*, 1995). Researchers eventually settled on the cosmogenic radionuclide ^{7}Be (half life of 53.3 days) due to its abundance in the lower stratosphere and its steep concentration gradients between the stratosphere and the troposphere (Lal and Peters, 1967).

^{7}Be is formed by spallation processes of light atmospheric nuclei such as ^{12}C, ^{14}N and ^{16}O with protons and neutrons (Zanis *et al.*, 1999). The galactic particles

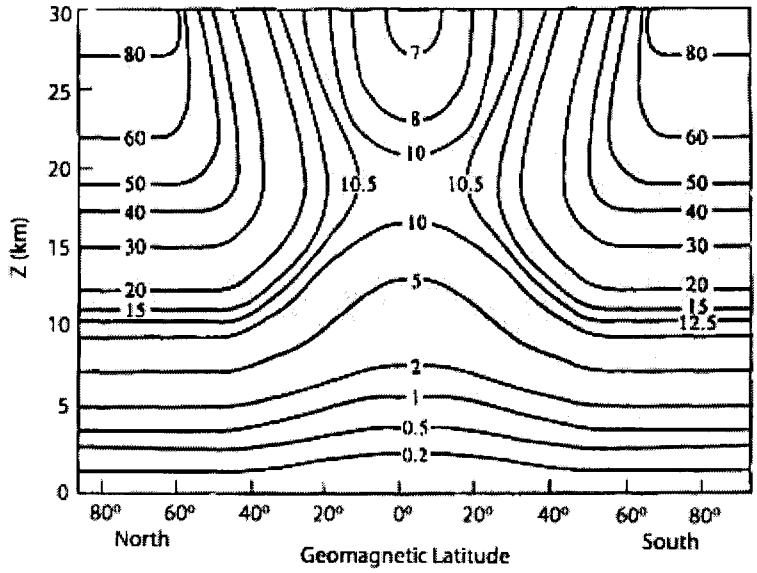

Figure 1 - A modeled north-south section through the atmosphere showing the surfaces of constant ^{7}Be production. Units are in nuclei min^{-1} m^{-3} at standard temperature and pressure. Taken from Lal and Peters (1967).

approach the solar system isotropically and tend to be deflected by the Earth's magnetic field and travel along field lines; hence, particles lose energy after successive collisions, and can (with low energy) enter the atmosphere predominantly over the magnetic poles, resulting in a pronounced pole-equator gradient in the flux of less energetic particles into the atmosphere which similarly leads to a pole-equator gradient of ^{7}Be production (Zanis *et al.*, 1999). About 75% of ^{7}Be is produced in the stratosphere and 25% in the troposphere (Johnson and Viezee, 1981) and there is a strong concentration gradient between the stratosphere and the troposphere (Feely *et al.*, 1989). Figure 1 shows the modelled ^{7}Be production rates in the atmosphere. It can clearly be seen from the figure that the production rates in the polar stratosphere are very large compared to the rest of the atmosphere and that steep horizontal and vertical gradients exist away from these locations. Talpos and Cuculeanu (1997) modeled vertical concentration profiles of ^{7}Be at 45°N. From the graph in Figure 2, it can be seen that ^{7}Be has a maximum concentration at approximately 15 km which

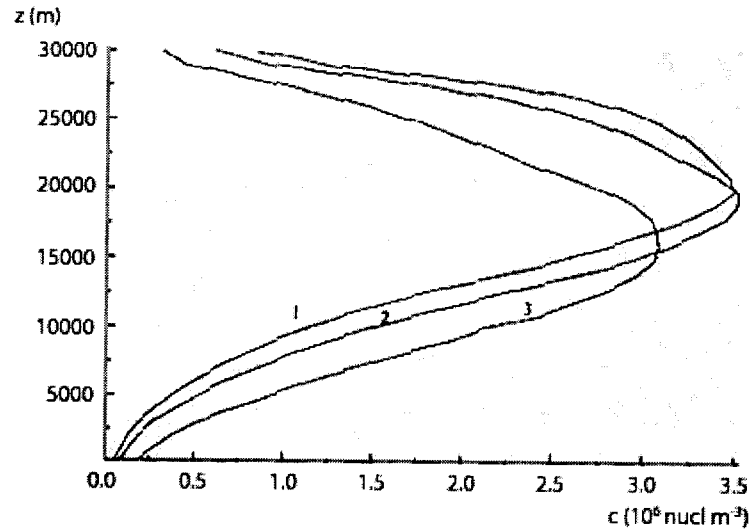

Figure 2 - The modeled vertical concentration profiles of ^{7}Be at 45°N for settling velocities (1) $\upsilon_s = 0$ ms^{-1}, (2) $\upsilon_s = 0.02$ ms^{-1} and (3) $\upsilon_s = 1$ ms^{-1}. Taken from Talpos and Cucleanu (1997).

then rapidly decreases to nearly zero at the surface.

Seasonal variation of surface ^{7}Be activity concentration varies greatly from place to place. Caillet *at al.* (2001) identified a summer maximum in Geneva, Switzerland. Bovis and Steyn (2001) and Megumi *et al.* (2000) determined a fall and spring maximum in Vancouver, Canada and Osaka, Japan respectively. Paatero and Hatakka (2000), Hotzl and Winkler (1987) and Dibb *et al.* (1994) identified spring maxima in Sodankyla, Finland; Neuherberg, Germany and Alert, Canada respectively. This difference in the seasonal variation of ^{7}Be is due to several factors. Since ^{7}Be concentrations at the surface greatly depend on air masses that have been transported from the upper troposphere/lower stratosphere, surface ^{7}Be concentrations are closely linked to the seasonality of STE (Feely *et al.*, 1989). Another major factor is that ^{7}Be attaches to sub-micron sized particles shortly after formation (Ishikawa *et al.*, 1995), which makes ^{7}Be susceptible to scavenging by precipitation. Feely *et al.* (1989) found strong correlations between average monthly precipitation and surface ^{7}Be concentrations for stations that had strong seasonal variations in precipitation.

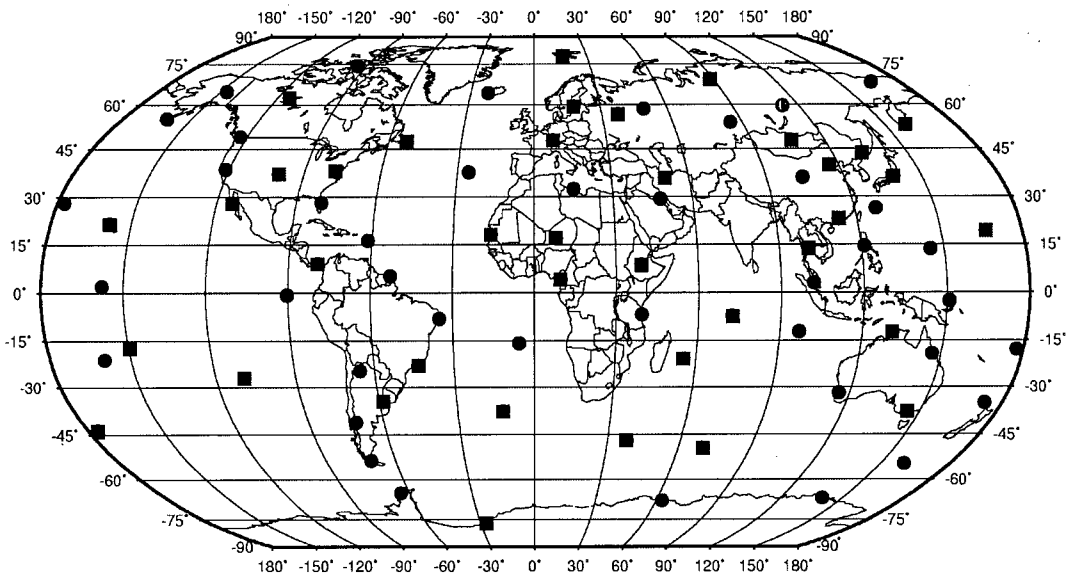

Figure 3 – Map of the Comprehensive Nuclear Test Ban Treaty Internaional Montoring System radionuclide network. Taken from Medici (2001).

Ishikawa *et al.* (1995) showed that only a small amount of precipitation was required to scavenge a sizeable amount of ^{7}Be out of the atmosphere. Thus, if only dry deposition measurements are being taken, a significant amount of information regarding ^{7}Be surface concentrations is being lost.

2.1.1 Radionuclide Measurements as part of the CTBT

The Comprehensive Nuclear Test Ban Treaty (CTBT) was a milestone agreement signed by 71 countries on 10 September 1996. The CTBT stated that no nuclear detonation of any kind or in any environment (air, land, underwater or underground) was to take place at any time. To ensure the treaty's compliance, the Comprehensive Nuclear Test Ban Treaty Organization (CTBTO) set up an International Monitoring System (IMS) network of 321 hydro acoustic, seismic, infrasonic and radionuclide monitoring stations and 16 radionuclide laboratories across the globe (Figure 3) to monitor and trace the origin of any nuclear detonations (Medici, 2001).

The radionuclide network is composed of 80 stations containing high volume air samplers, which collect aerosols and particulates of sub-micron size or larger on glass

fiber filters (Measday *et al.*, 2001). These filters are then analyzed for radionuclides, especially those of fissionogenic origin.

A side benefit of the radionuclide network is that many naturally occurring and anthropogenically produced radionuclides are monitored by the IMS as well. Bovis and Steyn (2001) and Measday *et al.* (2001) have already utilized these radionuclide data in the fields of stratosphere troposphere exchange and anthropogenic radionuclide monitoring respectively.

2.1.2 ^{7}Be Measurements in Vancouver, Canada

The IMS radionuclide station CA002 is located at The University of British Columbia west of Vancouver (49.25° N, 123.25° W). The station is located in a self-contained trailer next to fields used by the Faculty of Agricultural Sciences on a plateau about 50 m above sea level. The data are collected using a high volume air sampler capable of 1000 m^3hr^{-1}. Air is drawn through a high efficiency particulate filter with a square face area of 60 cm x 60 cm. Every 24 hours, the filter is removed and compacted into a disk with a diameter of 6.4 cm and a thickness of 1.4 cm (Measday *et al.*, 2001). The disk is then placed between two high-purity germanium detectors. The data collected by the germanium detector are then sent to the International Data Center in Vienna, Austria for further analysis (http://www.ctbto.org).

The ^{7}Be data utilized for this study range from 9 April 1996 – 12 March 2002 and have a temporal resolution of 24 hours. The entire ^{7}Be time series is shown in Figure 4. In agreement with Hotzl and Winkler (1987), the data are closely log- normally distributed (Figure 5). The geometric mean and standard deviation are 2032 μBqm^{-3} and 1773 μBqm^{-3} respectively. Figure 6 shows the monthly average ^{7}Be concentrations recorded at this station. The composite seasonal time series (Figure 6)

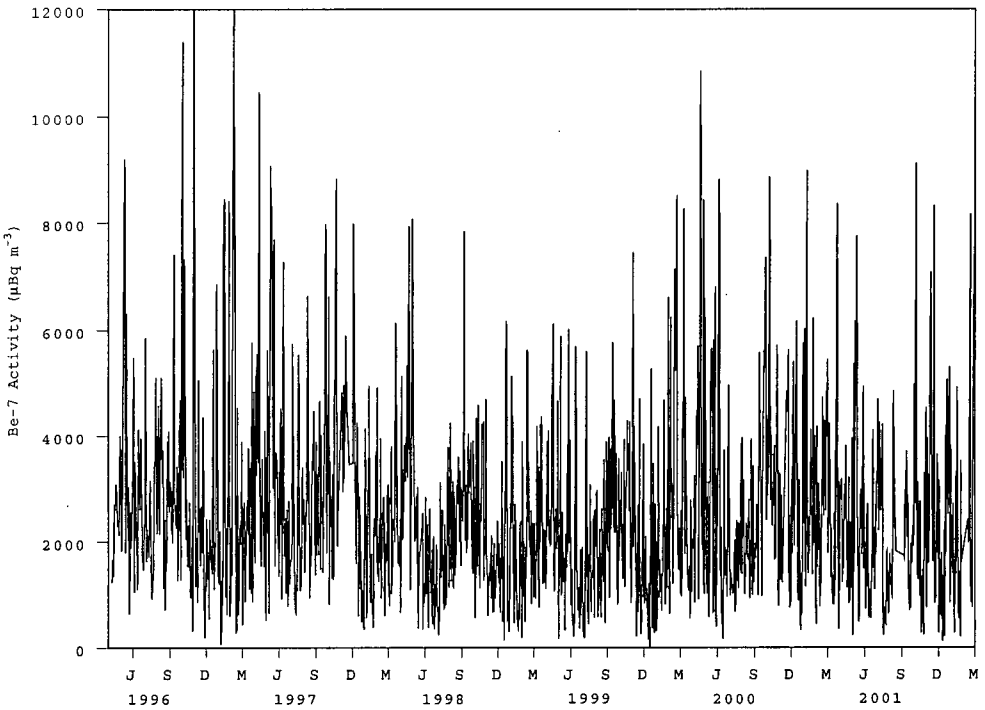

Figure 4 - Daily ^{7}Be activity concentrations measured at the CTBTO IMS station CA002 from 9 April 1996 - 12 March 2002.

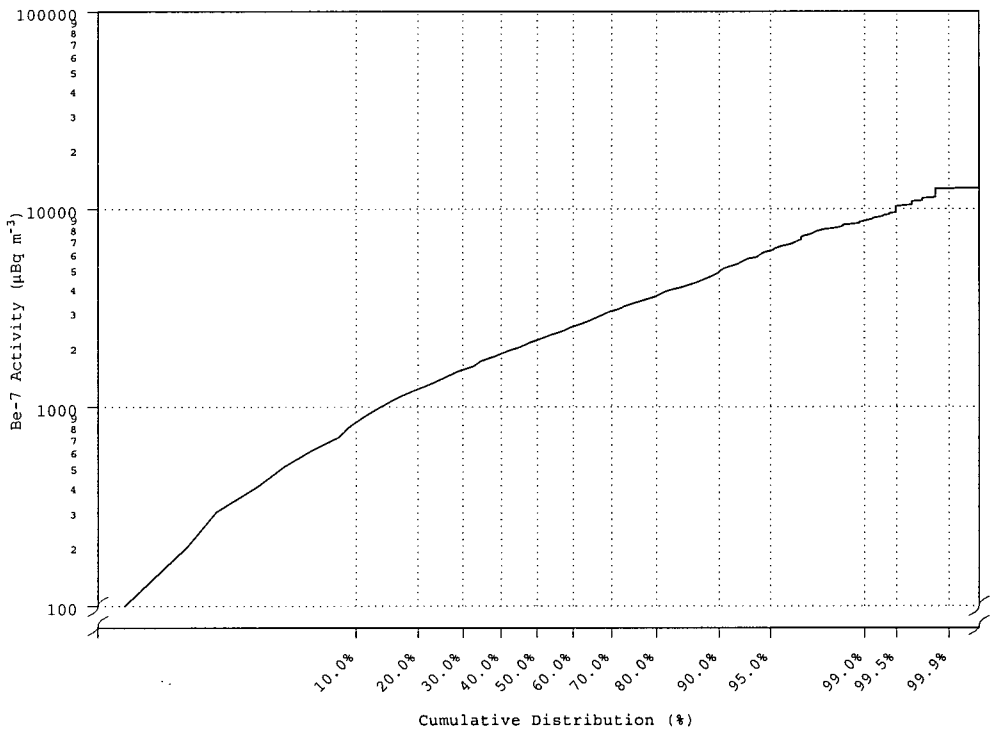

Figure 5 – Cumulative distribution of the ^{7}Be activity concentrations at the CTBTO IMS station CA002 during the period 9 April 1996 - 12 March 2002.

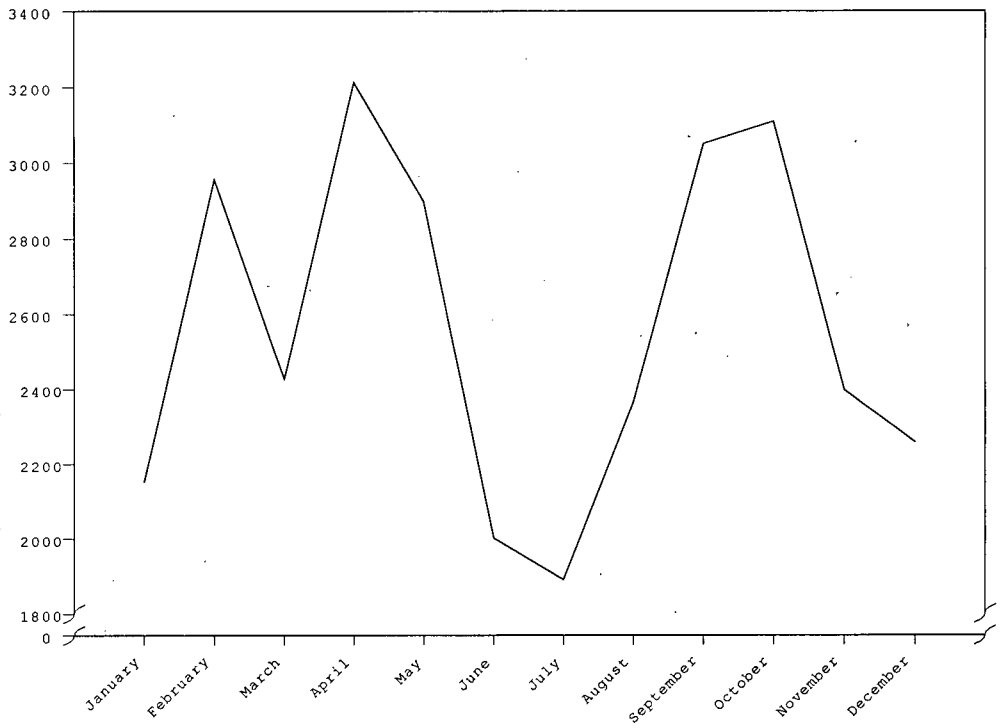

Figure 6 - Monthly average ^{7}Be concentration at the CTBTO IMS station CA002 during the period 9 April 1996 - 12 March 2002.

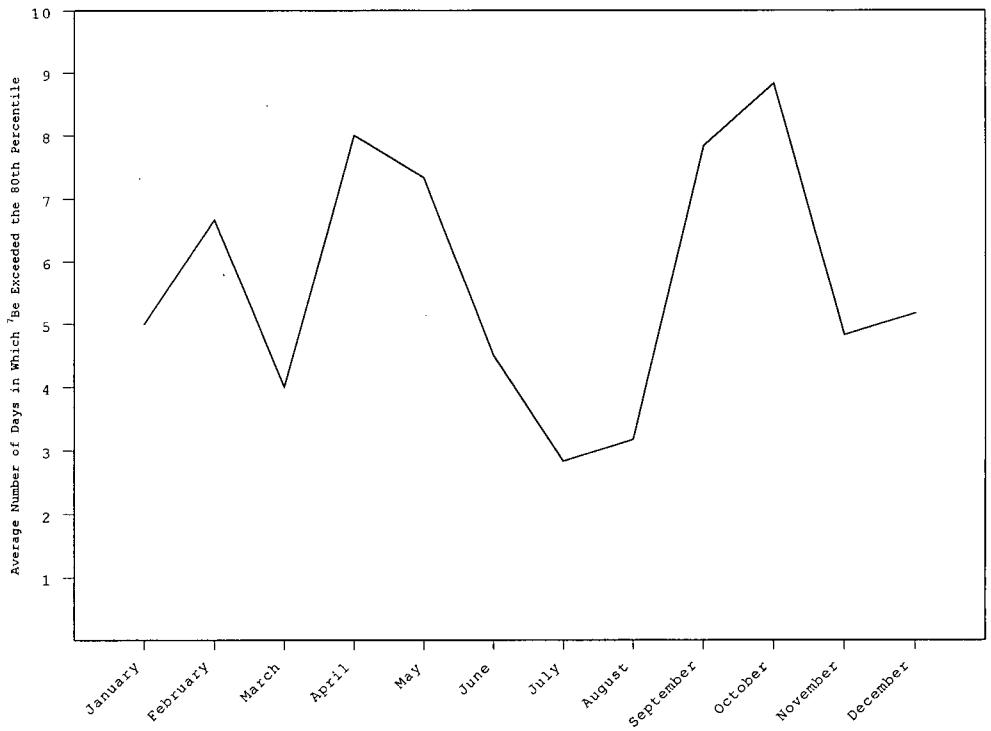

Figure 7 - Average number of days in a month in which ^{7}Be activity concentration exceeds the 80th percentile at the CTBTO IMS station CA002 during the period 9 April 1996 - 12 March 2002.

	Change in Odd Oxygen
$O_2 + h\upsilon \rightarrow O + O$	+2
$O + O_2 + M \rightarrow O_3 + M$	0
$O_3 + h\upsilon \rightarrow O + O_2$	0
$O + O_3 \rightarrow 2O_2$	-2
$O + O + M \rightarrow O_2 + M$	-2

Figure 8 - Chemical reactions of Chapman's mechanism, a static pure oxygen photochemical steady state model.

is bimodal with a spring and fall maximum and a summer and winter minimum. It must be kept in mind that these data are based on dry deposition measurements only so wet deposition caused by scavenging of ^{7}Be by precipitation is not taken into account. The winter season in Vancouver is associated with high precipitation, so if wet deposition measurements were being taken, the winter ^{7}Be concentration would be significantly higher. Figure 7 shows the average number of days in each month in which ^{7}Be exceeds the 80^{th} percentile. Again, spring and fall maxima are observed along with a secondary maximum in winter. These are periods in which air masses associated with stratosphere troposphere exchange could have an influence on ^{7}Be measurements taken at this station.

2.2 Ozone

2.2.1 Ozone Formation in the Stratosphere

Chapman (1930) was the first scientist to produce a theory of ozone formation in the stratosphere. Chapman's approach used oxygen as the only element involved in the reaction. Figure 8 shows the five reactions proposed by Chapman, along with the change in odd oxygen for each reaction, of the formation and destruction of ozone in the stratosphere. It was later found that this pure-oxygen reaction model produced ozone concentrations that were higher than observational values (Prinn *et al.*, 1978).

$$X + O_3 \rightarrow XO + O_2$$
$$XO + O \rightarrow X + O_2$$
$$\overline{O + O_3 \rightarrow O_2 + O_2}$$

Figure 9 - A generic sequence of reactions for the loss of odd oxygen by way of a catalytic cycle.

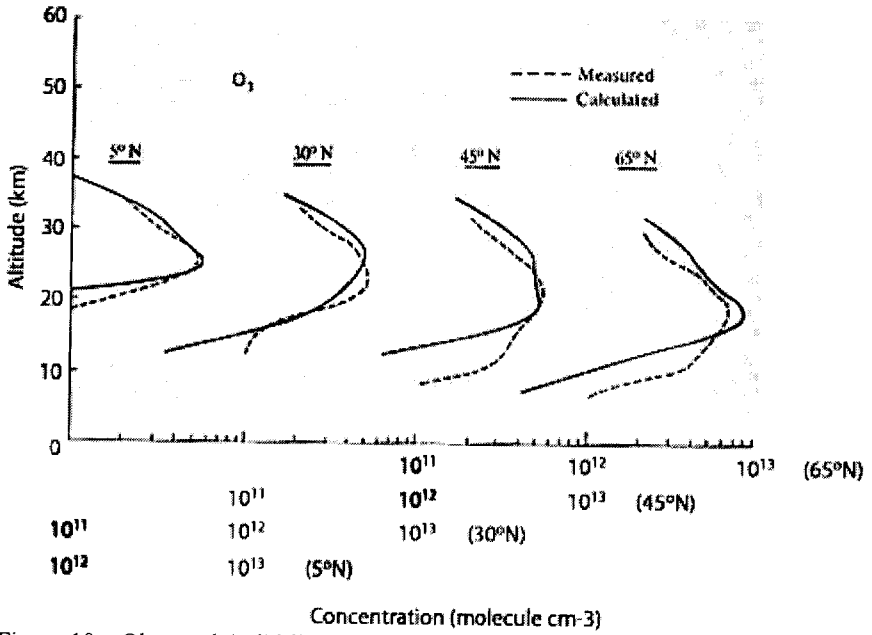

Figure 10 - Observed (solid line) and calculated (dashed line) vertical concentration profiles of ozone as a function of latitude in the Northern Hemisphere for mid-spring. Taken from Miller *et al.* (1981).

It was also found that the fourth reaction in Figure 8 only accounted for a quarter of the actual ozone loss (Wayne, 1999).

Bates and Nicolet (1950) proposed that trace atmospheric constituents could participate in catalytic process that removes ozone at a faster rate than the pure-oxygen model put forth by Chapman. The essence of catalytic schemes for the loss of odd oxygen is the provision of a more efficient route than the last two reactions in Figure 8 (Wayne, 1999). The chain mechanism depicted in Figure 9 achieves the same result as the fourth equation in Figure 8, but because of the catalyst, the reaction becomes faster, and ozone is destroyed more quickly than the Chapman mechanism (Wayne, 1999). Various chemical species have been identified as the catalyst, X, in

Figure 9 including H, OH, NO and Cl (Wayne, 1999). Miller *et al.* (1981), using a complex model based on catalytic cycles, found good agreement when compared with measured ozone profiles (Figure 10).

2.2.2 Ozone Formation in the Troposphere

In an urban region, ozone is formed in two major ways. The largest is the result of a series of reactions involving anthropogenically produced NO_x and volatile organic chemicals (VOCs) in the presence of ultraviolet radiation from the sun (Seinfeld and Pandis, 1998). Since temperature is a controlling factor on the reaction rate, the higher the temperature, the higher the measured ozone concentration. Anthropogenic ozone production is thus at a maximum during summer. A less important mechanism is a series of reactions involving naturally produced NO_x and VOCs in the presence of ultraviolet radiation (NRC, 1992). Wayne (1999) and NRC (1992) give a more detailed discussion on ozone formation in the troposphere with special attention paid to photochemical smog of which ozone is a major constituent.

2.2.3 The Greater Vancouver Regional District Air Quality Monitoring Network

Because of the geography of the Greater Vancouver Regional District, the region suffers from an acute ozone pollution problem, especially in the summer (Steyn *et al.*, 1997). To the west of the GVRD lies Georgia Straight which is a salt water body separating the British Columbia mainland and Vancouver Island. Mountain ranges lie to the north and south and the valley between these two ranges, in which the GVRD is located, becomes narrower further east. As pollutants travel down valley, they become trapped between the two mountain ranges as the valley narrows (Steyn *et al.*, 1997). Because of this, air pollutant concentrations, especially ozone, have a tendency to increase eastward in the GVRD.

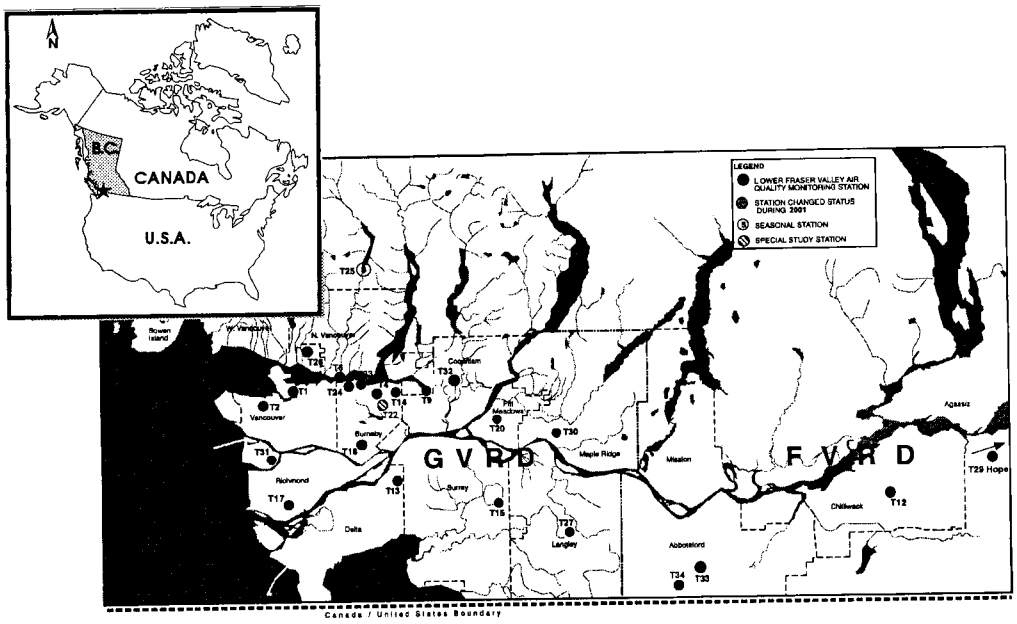

Figure 3 – Greater Vancouver Regional District Continuous Air Quality Monitoring Network. Air quality monitoring stations are indicated by the circles. Abbotsford International Airport is located at station T33, Vancouver International Airport is located at station T31 and the CTBTO IMS station CA002 is located just to the east of station T2. The stations used in this study are: Downtown Vancouver (T1), Kitsilano (T2), Chilliwack Airport (T12), Surrey East (T15), Richmond (T17), Langley Central (T27), Hope Airport (T29) and Port Coquitlam North (T32).

In order to observe the air quality in the GVRD, a monitoring network was set up starting in 1949. Today, there are over 30 monitoring stations operated by the GVRD Air Quality Department, most of which measure hourly concentrations of VOCs, NO_x, ozone, CO, SO_2 and suspended particulates. This monitoring network is displayed in Figure 11.

The GVRD ozone data set associated with this research spans between 1 January 1996 – 31 December 2001. All of the stations exhibit spring-summer maxima and a winter minimum. Figure 12 contains composite diurnal ozone concentration graphs for all stations used in this study. These stations are Downtown Vancouver (T001), Kitsilano (T002), Chilliwack Airport (T012), Surrey East (T015), Richmond (T017), Langley Central (T027), Hope Airport (T029) and Port Coquitlam North (T032). The error bars denote ± one standard deviation. These composites

a).

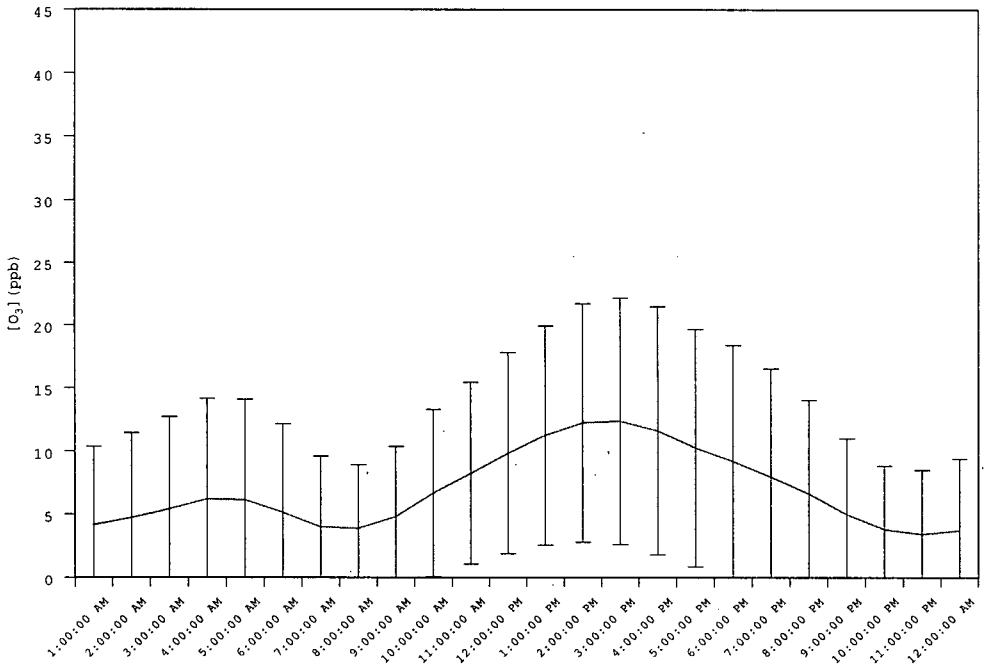
45
40
35
30
25
20
15
10
5
0
[O3] (ppb)
1:00:00 AM
2:00:00 AM
3:00:00 AM
4:00:00 AM
5:00:00 AM
6:00:00 AM
7:00:00 AM
8:00:00 AM
9:00:00 AM
10:00:00 AM
11:00:00 AM
12:00:00 PM
1:00:00 PM
2:00:00 PM
3:00:00 PM
4:00:00 PM
5:00:00 PM
6:00:00 PM
7:00:00 PM
8:00:00 PM
9:00:00 PM
10:00:00 PM
11:00:00 PM
12:00:00 AM

b).

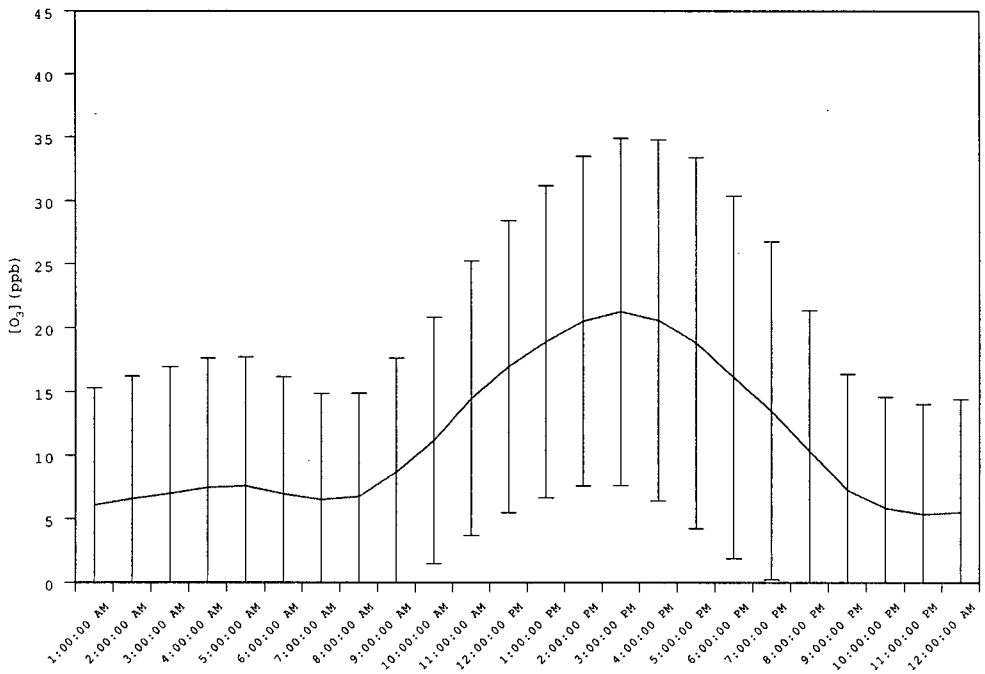
45
40
35
30
25
20
15
10
5
0
[O3] (ppb)
1:00:00 AM
2:00:00 AM
3:00:00 AM
4:00:00 AM
5:00:00 AM
6:00:00 AM
7:00:00 AM
8:00:00 AM
9:00:00 AM
10:00:00 AM
11:00:00 AM
12:00:00 PM
1:00:00 PM
2:00:00 PM
3:00:00 PM
4:00:00 PM
5:00:00 PM
6:00:00 PM
7:00:00 PM
8:00:00 PM
9:00:00 PM
10:00:00 PM
11:00:00 PM
12:00:00 AM

c).

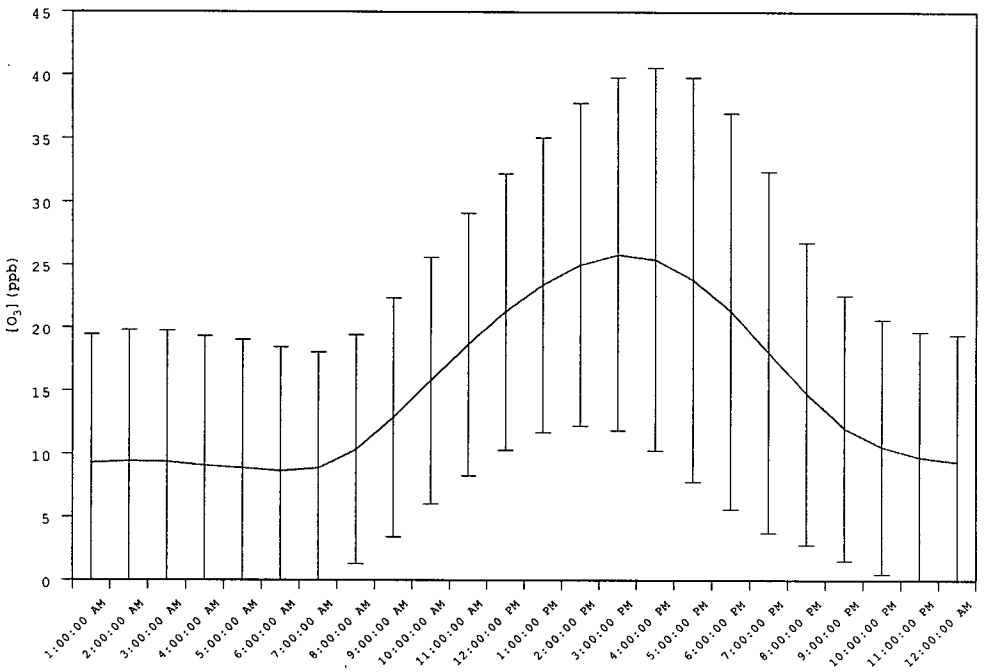
45
40
35
30
25
20
15
10
5
0
[O3] (ppb)
1:00:00 AM
2:00:00 AM
3:00:00 AM
4:00:00 AM
5:00:00 AM
6:00:00 AM
7:00:00 AM
8:00:00 AM
9:00:00 AM
10:00:00 AM
11:00:00 AM
12:00:00 PM
1:00:00 PM
2:00:00 PM
3:00:00 PM
4:00:00 PM
5:00:00 PM
6:00:00 PM
7:00:00 PM
8:00:00 PM
9:00:00 PM
10:00:00 PM
11:00:00 PM
12:00:00 AM

d).

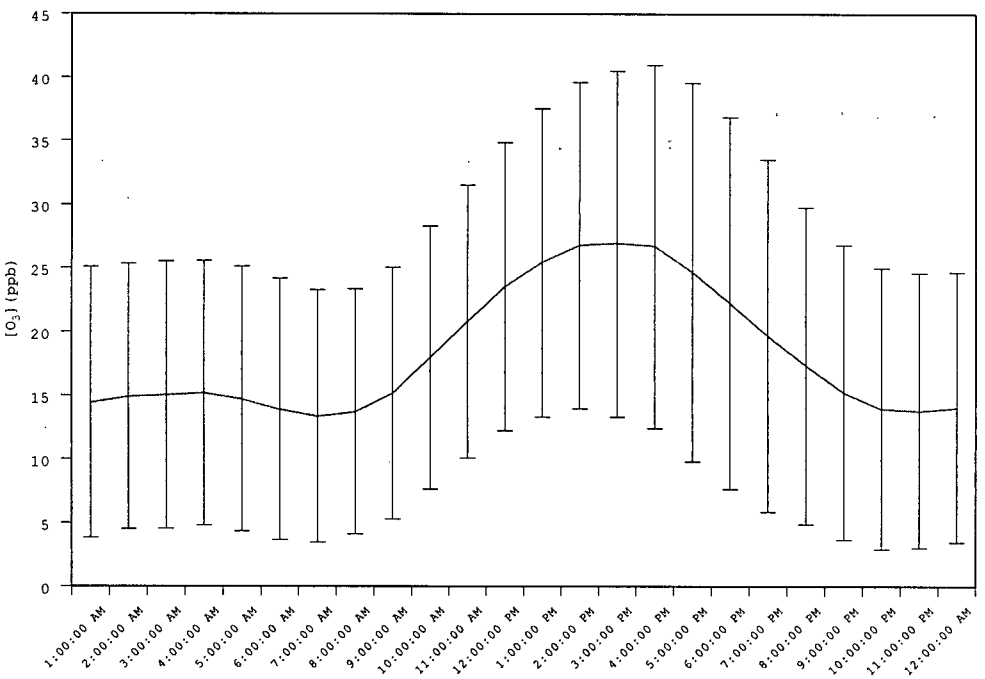
45
40
35
30
25
20
15
10
5
0
[O3] (ppb)
1:00:00 AM
2:00:00 AM
3:00:00 AM
4:00:00 AM
5:00:00 AM
6:00:00 AM
7:00:00 AM
8:00:00 AM
9:00:00 AM
10:00:00 AM
11:00:00 AM
12:00:00 PM
1:00:00 PM
2:00:00 PM
3:00:00 PM
4:00:00 PM
5:00:00 PM
6:00:00 PM
7:00:00 PM
8:00:00 PM
9:00:00 PM
10:00:00 PM
11:00:00 PM
12:00:00 AM

e).

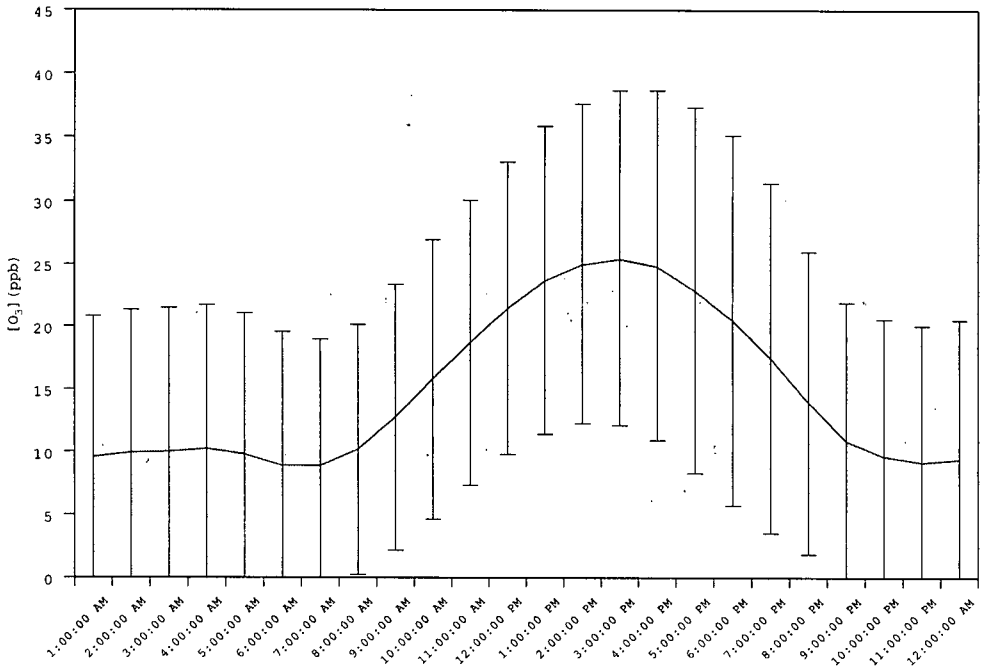
45
40
35
30
25
20
15
10
5
0
[O3] (ppb)
1:00:00 AM
2:00:00 AM
3:00:00 AM
4:00:00 AM
5:00:00 AM
6:00:00 AM
7:00:00 AM
8:00:00 AM
9:00:00 AM
10:00:00 AM
11:00:00 AM
12:00:00 PM
1:00:00 PM
2:00:00 PM
3:00:00 PM
4:00:00 PM
5:00:00 PM
6:00:00 PM
7:00:00 PM
8:00:00 PM
9:00:00 PM
10:00:00 PM
11:00:00 PM
12:00:00 AM

f).

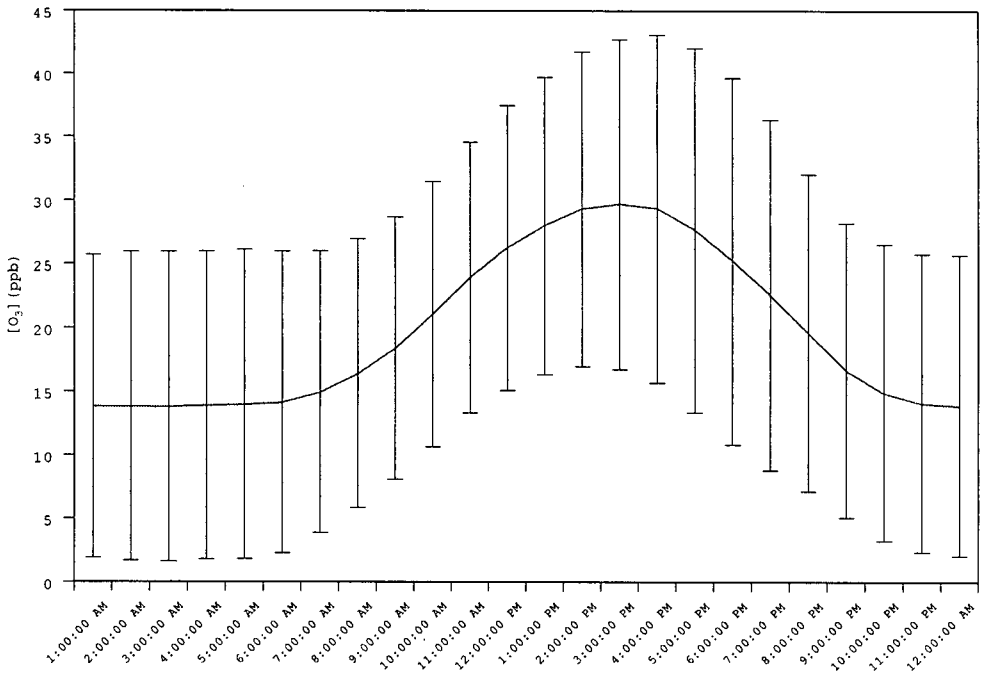
45
40
35
30
25
20
15
10
5
0
[O3] (ppb)
1:00:00 AM
2:00:00 AM
3:00:00 AM
4:00:00 AM
5:00:00 AM
6:00:00 AM
7:00:00 AM
8:00:00 AM
9:00:00 AM
10:00:00 AM
11:00:00 AM
12:00:00 PM
1:00:00 PM
2:00:00 PM
3:00:00 PM
4:00:00 PM
5:00:00 PM
6:00:00 PM
7:00:00 PM
8:00:00 PM
9:00:00 PM
10:00:00 PM
11:00:00 PM
12:00:00 AM

g.)

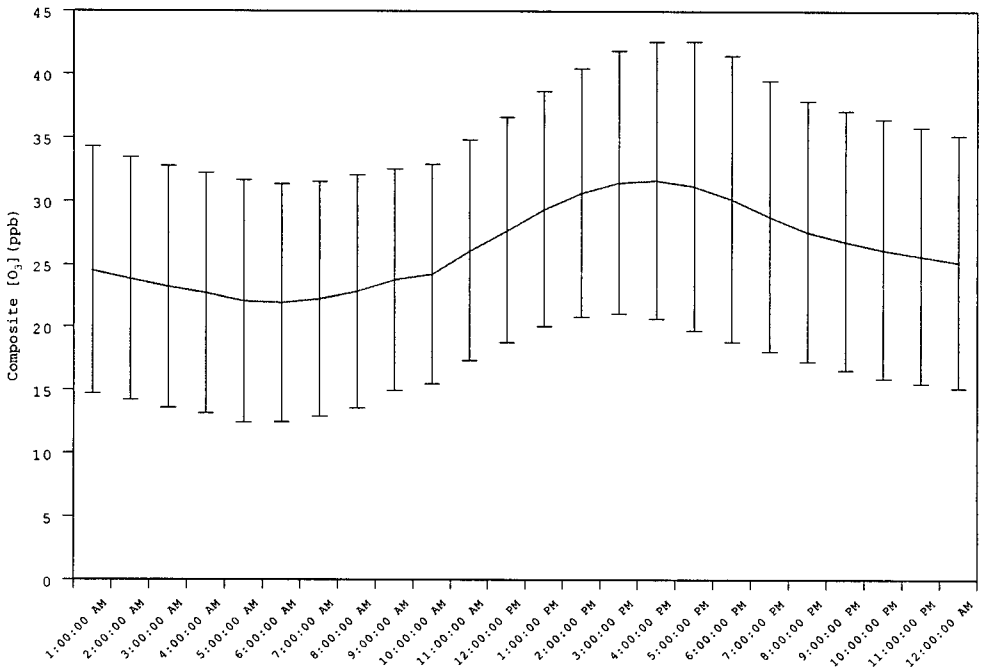
Composite [O3] (ppb)
45
40
35
30
25
20
15
10
5
0
1:00:00 AM
2:00:00 AM
3:00:00 AM
4:00:00 AM
5:00:00 AM
6:00:00 AM
7:00:00 AM
8:00:00 AM
9:00:00 AM
10:00:00 AM
11:00:00 AM
12:00:00 PM
1:00:00 PM
2:00:00 PM
3:00:00 PM
4:00:00 PM
5:00:00 PM
6:00:00 PM
7:00:00 PM
8:00:00 PM
9:00:00 PM
10:00:00 PM
11:00:00 PM
12:00:00 AM

h).

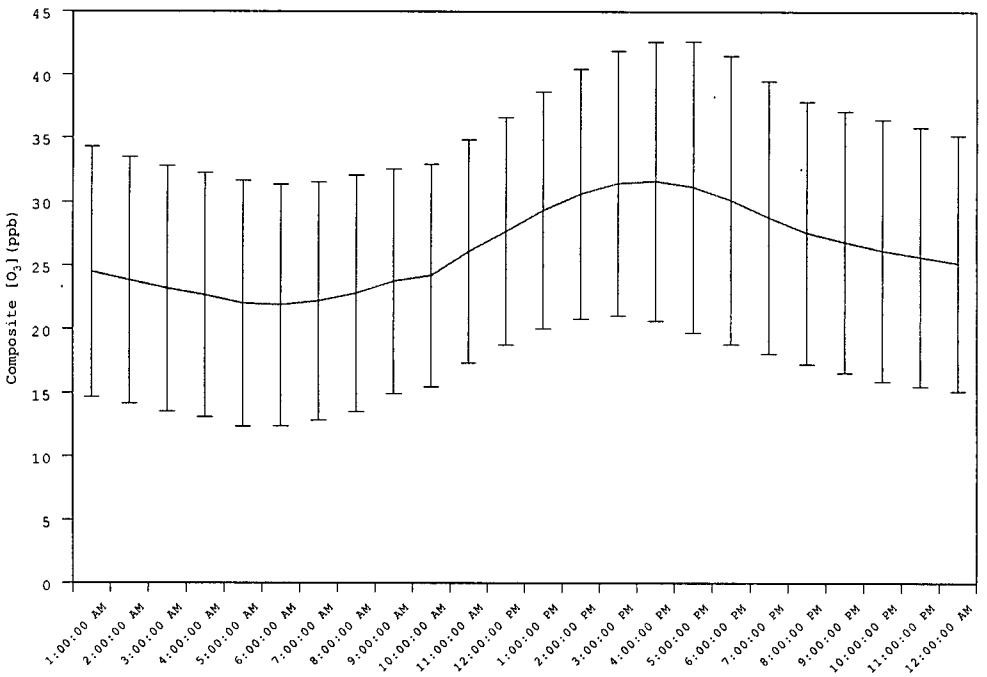
Composite [O3] (ppb)
45
40
35
30
25
20
15
10
5
0
1:00:00 AM
2:00:00 AM
3:00:00 AM
4:00:00 AM
5:00:00 AM
6:00:00 AM
7:00:00 AM
8:00:00 AM
9:00:00 AM
10:00:00 AM
11:00:00 AM
12:00:00 PM
1:00:00 PM
2:00:00 PM
3:00:00 PM
4:00:00 PM
5:00:00 PM
6:00:00 PM
7:00:00 PM
8:00:00 PM
9:00:00 PM
10:00:00 PM
11:00:00 PM
12:00:00 AM

Figure 12 (previous pages) - Composite diurnal ozone concentration graphs for a). Downtown Vancouver (T001), b). Kitsilano (T002), c). Chilliwack Airport (T012), d). Surrey East (T015), e). Richmond (T017), f). Langley Central (T027), g). Hope Airport (T029) and h). Port Coquitlam North (T032). The error bars denote +/- one standard deviation. The composites were constructed by averaging all of the measurements for a given hour at a given station.

---

were constructed by averaging all of the measurements for a given hour at a given station. The resulting graph is an average diurnal ozone time series for each station, each of which exhibits a daily maximum at 2:00pm PST and a daily minimum between 7:00am – 8:00am PST.

2.3 Temperature and Precipitation

This research makes use of hourly measurements of temperature and precipitation taken by the Meteorological Service of Canada spanning 1 January 1996 – 31 December 2001. The temperature data set includes data from Vancouver International Airport and Abbotsford International Airport while the precipitation data set includes data from Vancouver International Airport only. These two stations are labeled in Figure 11.

2.4 Satellite Data

Several satellite images were extracted from the Canadian Meteorological Center database for use with specific case studies covered in Section 3 of this thesis. The thermal infrared data and water vapor data were measured by the NASA Geostationary Earth Orbiting Satellite (GOES-10) with a pixel resolution of 4km. The thermal infrared data were measured at 10.7 microns and the water vapor data were measured at 6.7 microns. The temporal resolution of this data set is three hours.

3. Data Analysis

There are two main goals of the current research. The first is to identify episodes where ozone transported from the stratosphere is possibly influencing ground level ozone concentrations in the LFV. The second goal is to utilize meteorological back

trajectory analysis to identify the source regions of this stratospheric ozone. Once these episodes have been identified, several case studies will be investigated in greater detail and will include, in addition to ^{7}Be and ozone analysis, an examination of the synoptic meteorology as well as temperature and precipitation measurements.

This section will describe the two algorithms that were used to detect episodes in which air of stratospheric origin may be influencing the ground level ozone concentrations in the LFV. Section 4 introduces the concept of meteorological back trajectory analysis and the models that were used in the current research. Section 4 will also cover the four detailed case studies selected from the episodes identified in Sections 3.1 and 3.2.

3.1 80th Percentile Algorithm

This algorithm selected the 80^{th} percentile of all daily ^{7}Be activity concentrations and the 80^{th} percentile of all average daily maximum ground level ozone concentrations. The 80^{th} percentile cutoff was selected because at cutoff percentiles lower than this, some of the resulting cases may not contain ^{7}Be activity concentrations and ground level ozone concentrations that are being influenced by air of stratospheric origin. By picking cutoff percentiles higher than 80% some possible cases of stratospheric intrusions may be missed. On a given day, the average daily maximum ozone concentration is found by selecting and then averaging the highest hourly ozone concentration from each station across the network. The intersection of these two 80^{th} percentile data sets was then found so that the final resulting data set contained days in which both the daily ^{7}Be activity concentration and the average daily maximum ground level ozone concentration were in the 80^{th} percentile. This algorithm was then modified twice to exclude months in which anthropogenically derived ozone production is at a maximum. These modified algorithms selected

episodes in which stratospheric ozone may be influencing ground level ozone concentrations in the Lower Fraser Valley.

3.1.1 80th Percentile Algorithm Using All Data

All of the cases that were detected using this algorithm were distributed among 54 episodes, each episode possibly containing more than one case. A case is a period in which both the ^{7}Be activity concentrations and the average daily maximum ozone concentrations are in the 80^{th} percentile during a single day or on consecutive days. If more than one case occurred over the span of a few days,

Episode	Dates (yy/mm/dd)	Max ^{7}Be (μBqm^{-3})	Max [O_3] (ppb)
1	96/4/29, 96/5/1	3924.5	40.0
2	96/5/8-96/5/9, 96/5/11	5750.2	48.2
4	96/5/15-96/5/17	6614.8	49.4
5	96/6/2/-96/6/3	5613.9	41.6
6	96/6/15, 96/6/21	4234.5	40.8
7	96/7/2, 96/7/8, 96/7/14	5332.4	48.7
8	96/7/26, 96/7/28-96/7/29	6677.1	68.5
9	96/8/9-96/8/10	5259.4	69.2
10	97/3/30	4961.8	42.9
11	97/4/6-97/4/8, 97/4/11	5686.4	44.3
12	97/4/20, 97/4/26	4208.2	44.8
13	97/5/3, 97/5/9-97/5/16, 97/5/18-97/5/19	9290.6	67.3
14	97/6/6	4638.3	40.6
15	97/7/4	5887.8	45.2
16	97/7/18-97/7/20	5677.3	61.1
17	97/8/10-97/8/12	6835.3	49.8
18	98/4/9, 98/4/13, 98/4/17-98/4/18	5496.2	42.7
19	98/4/20-98/4/21, 98/4/28-98/4/30	6381.5	46.1
20	98/5/1-98/5/4	7582.0	51.1
21	98/7/29, 98/8/4	4376.0	69.5
22	98/9/5-98/9/7	8077.3	42.2
23	99/3/1	4316.1	37.3
24	99/4/2	4036.8	42.7
25	99/4/15-99/4/18	6309.8	50.9
26	99/4/30	4796.0	42.1
27	99/5/6	6070.8	39.1
28	99/5/24, 99/5/27	6211.0	54.9
29	99/6/12-99/6/14	5867.5	43.9
30	99/7/9-99/7/11	5771.7	58.2

31	99/8/23	3668.2	37.7
32	99/9/29	3680.1	48.9
33	00/4/9	3821.6	41.2
34	00/4/17-00/4/21	10845.5	47.2
35	00/4/27, 00/4/30-00/5/1, 00/5/3	8459.8	42.2
36	00/5/14-00/5/18	5661.2	46.5
37	00/5/24-00/5/25	5954.7	48.6
38	00/6/2-00/6/4	8827.7	53.6
39	00/6/17	3739.3	40.5
40	00/6/27-00/6/28	4960.3	56.2
41	00/7/30	3817.4	39.4
42	00/8/23	3952.5	39.5
43	01/2/16	4739.7	38.8
44	01/3/19	3716.4	39.5
45	01/3/25	4054.3	40.7
46	01/4/15	3832.1	47.7
47	01/4/30	3967.0	50.0
48	01/5/4	5374.7	40.2
49	01/5/7-01/5/12	7760.6	50.4
50	01/5/27-01/5/28	4938.8	50.4
51	01/6/21	4117.0	44.6
52	01/7/2-01/7/3, 01/7/7	4700.6	55.1
53	01/8/10-01/8/11	4853.4	58.0
54	02/2/24	5418.9	38

Table 1 - Episodes based on the 80th percentile detection algorithm (all data). The highest daily ^{7}Be activity concentration and the highest average daily maximum ozone concentration are indicated for each episode.

these cases were grouped to form one episode, thus making analysis easier. Therefore, an episode is a time period in which one or more cases occurred. Table 1 lists all of the episodes and the dates of the cases that they contain. Table 1 also lists the highest ^{7}Be activity concentration and the highest average daily maximum ozone concentration that occurred during each episode. Figure 13 shows the daily ^{7}Be activity concentration, the average daily maximum temperature, the average daily maximum ground level ozone concentration and the coefficient of variation of ozone of four of these episodes. Graphs of all the episodes can be found in Bovis and Steyn (2001).

a).

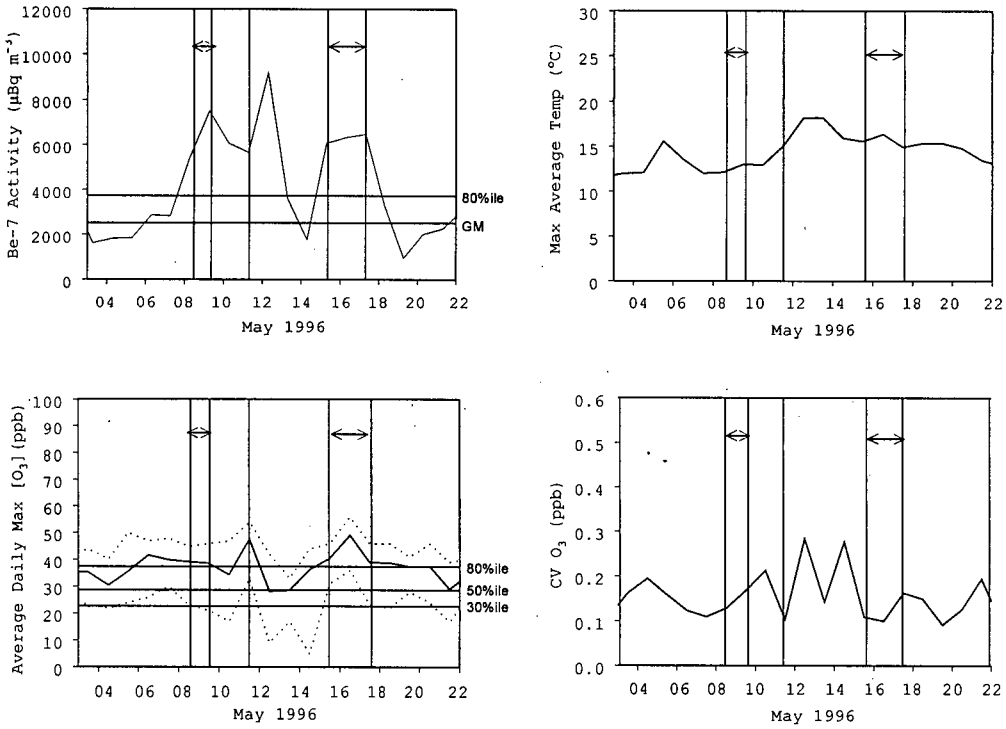
Be-7 Activity (μBq m⁻³)
80%ile
GM
May 1996
Max Average Temp (°C)
May 1996
Average Daily Max [O3] (ppb)
80%ile
50%ile
30%ile
May 1996
CV O3 (ppb)
May 1996

b).

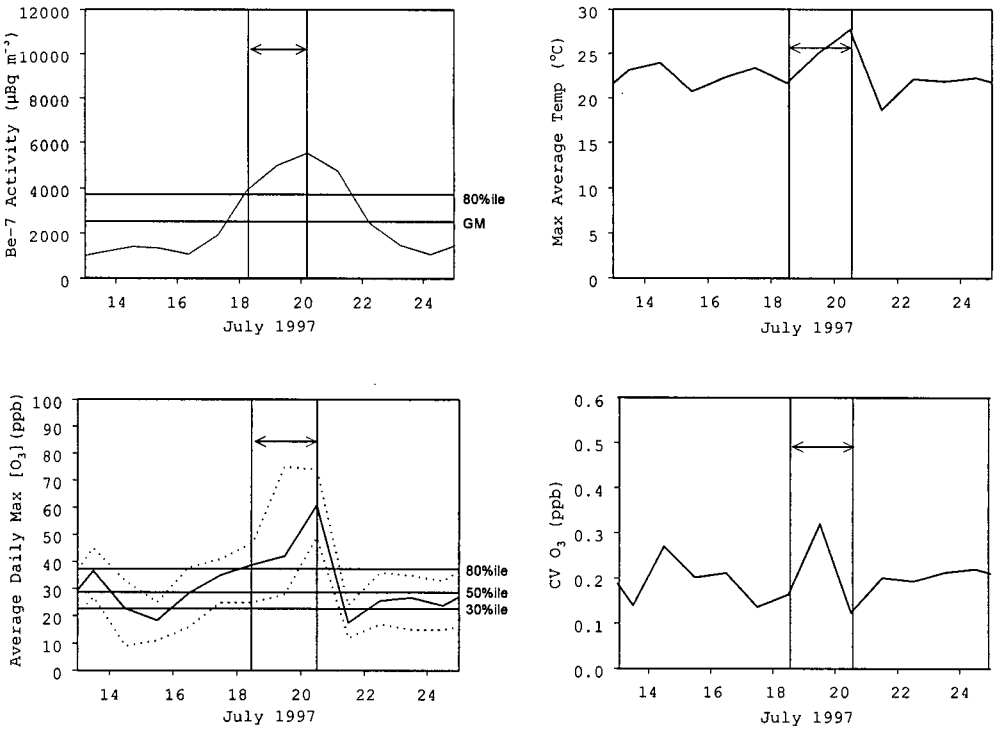
Be-7 Activity (μBq m⁻³)
80%ile
GM
July 1997
Max Average Temp (°C)
July 1997
Average Daily Max [O3] (ppb)
80%ile
50%ile
30%ile
July 1997
CV O3 (ppb)
July 1997

c).

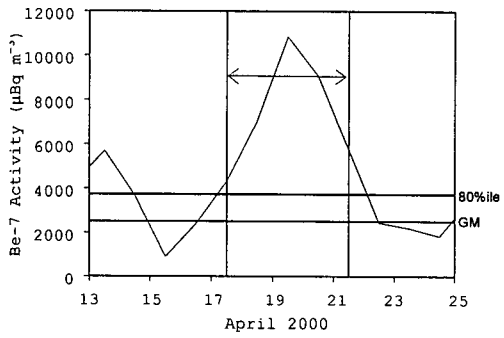
Be-7 Activity (μBq m⁻³)
12000
10000
8000
6000
4000
2000
0
80%ile
GM
13 15 17 19 21 23 25
April 2000

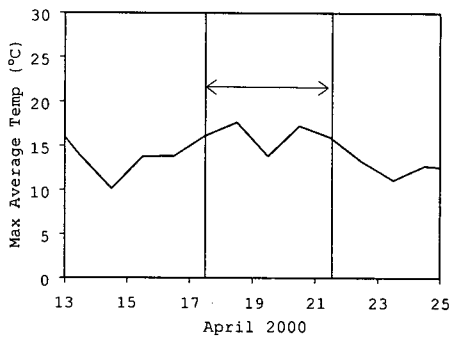
Max Average Temp (°C)
30
25
20
15
10
5
0
13 15 17 19 21 23 25
April 2000

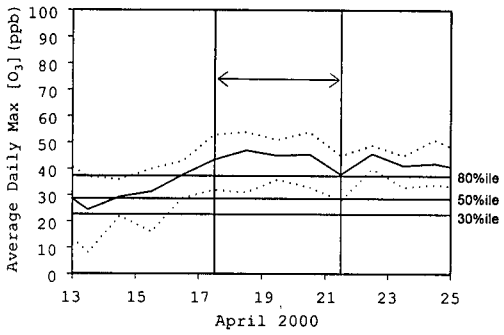
Average Daily Max [O3] (ppb)
100
90
80
70
60
50
40
30
20
10
0
80%ile
50%ile
30%ile
13 15 17 19 21 23 25
April 2000

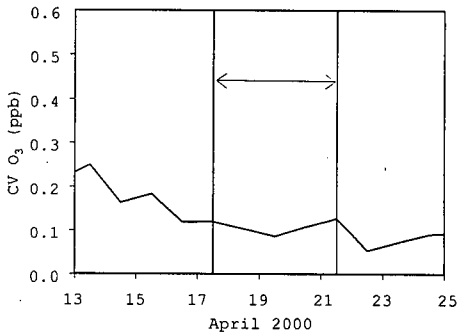
CV O3 (ppb)
0.6
0.5
0.4
0.3
0.2
0.1
0.0
13 15 17 19 21 23 25
April 2000

d).

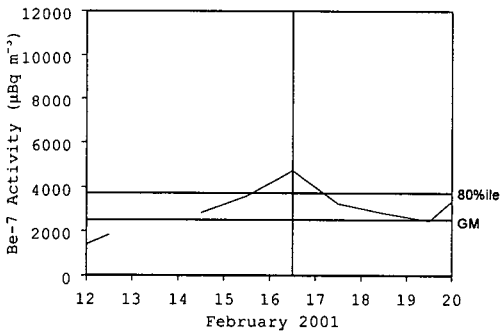
Be-7 Activity (μBq m⁻³)
12000
10000
8000
6000
4000
2000
0
80%ile
GM
12 13 14 15 16 17 18 19 20
February 2001

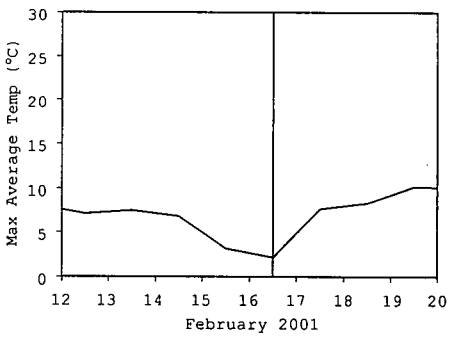
Max Average Temp (°C)
30
25
20
15
10
5
0
12 13 14 15 16 17 18 19 20
February 2001

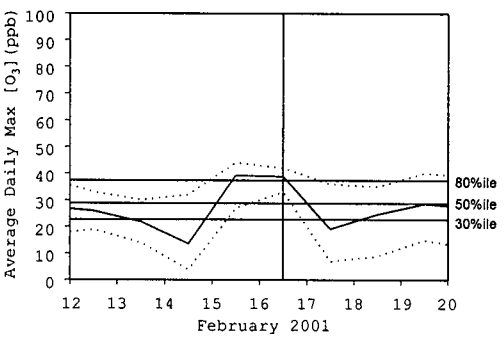
Average Daily Max [O3] (ppb)
100
90
80
70
60
50
40
30
20
10
0
80%ile
50%ile
30%ile
12 13 14 15 16 17 18 19 20
February 2001

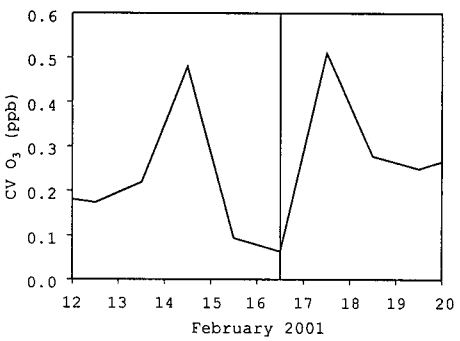
CV O3 (ppb)
0.6
0.5
0.4
0.3
0.2
0.1
0.0
12 13 14 15 16 17 18 19 20
February 2001

Figure 13 (previous pages) - ^{7}Be activity concentration, average daily maximum temperature, average daily maximum ozone concentration and coefficient of variance of ozone for a) 3 May 1996 – 22 May 1996, b) 13 July 1997 – 25 July 1997, c) 13 April 2000 – 25 April 2000 and d) 11 February 2001 – 20 February 2001 from the 80th percentile detection algorithm (all data). A single vertical line represents an episode in which both ^{7}Be and ozone were above the 80th percentile for one day only. Two vertical lines with an arrow between them indicate a multi-day episode. The graph on the upper left shows the daily ^{7}Be activity concentration. The top horizontal line indicates the 80th percentile value. Values above this line constitute the top 20% of all daily ^{7}Be activity concentrations in the data set. The lower line (marked GM) is the geometric mean daily ^{7}Be activity concentration for the entire data set. The graph on the upper right shows the average daily maximum temperature, which is found by selecting and then averaging the daily maximum temperatures measured at both Abbotsford International Airport and Vancouver International Airport (Figure 11). For the graph on the lower left, the solid line is the average daily maximum ground level ozone concentration. The upper dotted line is the highest hourly ozone concentration recorded over the entire network on a given day. The lower dotted line is the lowest daily maximum value recorded over the entire network on a given day. The upper horizontal line indicates the 80th percentile value, the middle line represents the median value and the lower line represents the 30th percentile value. The graph on the lower right shows the coefficient of variation (CV) of ozone which is the standard deviation of the daily maximum ground level ozone concentrations recorded across the network divided by the average daily maximum ground level ozone concentration.

In Figure 13, if the CV is small, the daily maximum ground level ozone concentrations recorded across the network will be similar. Because air masses influenced by stratosphere troposphere exchange are 100's of km long and 10's of km wide (Johnson and Viezee, 1981), one would expect a network wide rise in ozone once this air mass reached the surface. This would lower the CV value, because all monitoring stations would be recording approximately the same ozone concentration at any given time during the episode.

During most of the episodes three things occur. First, a local maximum occurs in the average daily maximum ground level ozone concentration. Second, the maximum daily ^{7}Be activity concentration measured during an episode corresponds to a local spatial maximum in average daily maximum temperature. This may be due to ^{7}Be being vertically transported to the lower troposphere by subsiding air in a high pressure system followed by entrainment into the boundary layer. This subsiding air is adiabatically warmed as it descends, thus the increase in surface temperature. Finally, the entire episode is characterized by a relative minimum in the CV of ozone. This characteristic is only evident in about 50% of the identified cases. One reason

for this is that the stratospheric signature of the subsiding air in some episodes may be weak. This weak signature could be due to either dilution of stratospheric air over a long transport path or a weak stratosphere troposphere exchange episode initially (or both). This weak stratospheric signature would mean that stratospheric ozone from this subsiding air could be partially or completely scavenged by NO_x at some stations, especially during the night-time hours when NO_x concentrations are high (NRC 1992). This would increase the CV of ozone because the spatial structure of the daily maximum ground level ozone concentrations would increase.

The disadvantage of the 80^{th} percentile algorithm using all of the data is that it selects many episodes in which ground level ozone concentrations are heavily influenced by ozone that is derived from anthropogenic precursors. An episode in which anthropogenically derived ozone is a factor occurs when the average daily maximum temperature exceeds approximately 20°C. Wunderli and Gehrig (1991) showed that at temperatures higher than this, the daily maximum ozone concentration at two air quality sites surrounding Zurich, Switzerland approached or exceeded 80 ppb. This is close to the Canadian Air Quality Objective maximum allowable one-hour ozone concentration of 82 ppb. It was concluded that the majority of this ozone was produced from anthropogenic precursor pollutants because of the high concentrations of peroxyacetyl nitrate (PAN) that existed during this time. During a summer STE episode in Montreal, Tremblay and Servranckx (1993) estimated that the stratospheric contribution to the ground level ozone concentration was only about 10 ppb. This constituted about 18% of the total ground level ozone concentration. Therefore selecting episodes during days in which the average daily maximum temperature is lower than 20°C would ensure that stratospheric ozone would be

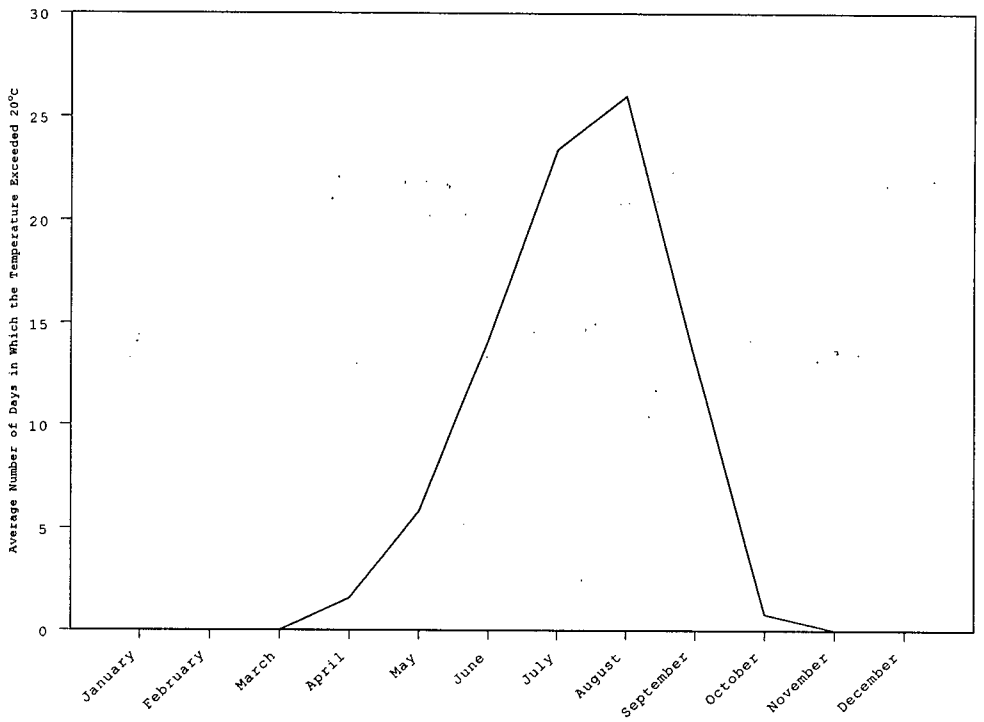

Figure 14 - Average number of days in a month in which the average daily maximum temperature exceeded 20°C in the Lower Fraser Valley during the period 10 April 1996 – 31 December 2001.

making a larger contribution to the total ground level ozone concentration, when compared to ozone produced from anthropogenic precursor pollutants.

3.1.2 80th Percentile Algorithm Excluding June to August

In order to eliminate the majority of the high temperature cases, the 80th percentile algorithm detection algorithm was refined slightly. Before the algorithm selected the two 80th percentile data sets of ^{7}Be and ozone, all months between June and August inclusive were excluded from the data set. These months were excluded because they contained the highest frequency of days in which the average daily maximum temperature exceeded 20°C (Figure 14). The algorithm then selected the ^{7}Be and ozone 80th percentile data sets. The intersection of these two data sets was then found. The episodes that were selected using this algorithm are listed in Table 2.

Episode	Dates (yy/mm/dd)	Max ^{7}Be (μBqm^{-3})	Max [O_3] (ppb)
1	96/4/30	4129.0	36.2
2	96/5/8-96/5/10	7626.4	48.2
4	96/5/15-96/5/17	6614.8	49.4
5	97/3/30	4961.8	42.9
6	97/4/6-97/4/8, 97/4/11-97/4/13	10718.8	47.2
7	97/4/26	4208.2	37.4
8	97/5/3	5764.5	45.5
9	97/5/9-97/5/16, 97/5/18-97/5/19	9290.6	67.3
10	98/4/15, 98/4/17-98/4/18, 98/4/20-98/4/21	6381.5	45.5
11	98/4/30	8320.9	40.2
12	98/5/1-98/5/4	7582.0	51.1
13	98/9/6-98/9/7	8077.3	62.8
14	99/2/13	5732.6	36.2
15	99/3/8	4316.1	37.3
16	99/3/17	4348.3	36.8
17	99/4/2	4036.8	42.7
18	99/4/15, 99/4/17-99/4/18	6309.8	50.9
19	99/4/30	4796.0	42.1
20	99/5/6	6070.8	39.1
21	99/5/27	6211.0	49.8
22	99/9/14	4089.5	37.1
23	00/4/10	4375.9	36.9
24	00/4/17-00/4/19, 00/4/20-00/4/21	10845.5	47.2
25	00/4/27, 00/4/30	8439.8	41.3
26	00/5/1, 00/5/3	4799.6	42.2
27	00/5/14-00/5/18	5661.2	48.2
28	00/5/24-00/5/25	5954.7	48.6
29	01/2/26	4739.7	38.8
30	01/3/25	4054.3	40.7
31	01/4/30	3967.0	50.0
32	01/5/4, 01/5/7-01/5/12	7760.6	50.4
33	01/5/27-01/5/28	4938.8	50.4
34	01/10/6	6346.9	37.2
35	02/2/24	5418.9	38.0

Table 2 - Episodes based on the 80th percentile detection algorithm (excluding June - August). The highest daily ^{7}Be activity concentration and the highest average daily maximum ozone concentration are indicated for each episode.

Although a few high temperature cases remain, most of the episodes are low temperature.

3.1.3 80th Percentile Algorithm Excluding May to September

The algorithm can be further refined by removing all months between May and September inclusive before starting the algorithm. Excluding these months will further eliminate days in which the average daily maximum temperature exceeds 20°C (Figure 14). The resulting episodes from this algorithm are shown in Table 3. Although the final 80th percentile algorithm produces only half as many cases as the first algorithm, the number of high temperature episodes (>20°C) has been reduced from 58% to 17%. The ground level ozone concentrations associated with these low temperature episodes in the final 80th percentile algorithm are possibly strongly influenced by air of stratospheric origin.

3.1.4 Disadvantages of the 80th Percentile Algorithm

There is still a major problem with the third 80th percentile algorithm in that all of the episodes, with one exception, occur only during March and April. This is due to the fact that both ground level ozone concentrations and daily ^{7}Be activity concentrations are quite high during these months. By using the average daily maximum ozone data instead of the hourly data recorded at the stations, one cannot obtain a detailed sense of what is happening spatially and temporally over the entire network. The CV of ozone gives some insight on spatial variability, but does not indicate how the concentration varies over a small temporal scale (i.e. on the order of hours). Also, none of the 80th percentile algorithms describe which stations have similar values at any one time and where the stations are located (i.e. urban or rural areas). The algorithm described next attempts to correct these three problems.

Episode	Dates (yy/mm/dd)	Max ^{7}Be (μBqm^{-3})	Max [O_3] (ppb)
1	96/4/29	3924.5	37.5
2	97/3/30, 97/4/3-97/4/4, 97/4/6-97/4/7	5686.4	44.3
3	97/4/11-97/4/13	10718.8	47.2
4	97/4/26	4208.2	37.4
5	98/4/9	3954.7	43.7
6	98/4/13, 98/4/15, 98/4/17-98/4/18	5496.2	43.3
7	98/4/20-98/4/22	8176.9	45.5
8	98/4/28-98/4/30	8320.9	46.1
9	99/2/13	5732.6	36.2
10	99/3/8	4316.1	37.3
11	99/3/17	4348.3	36.8
12	99/4/2	4036.8	42.7
13	99/4/15-99/4/18	6309.8	50.9
14	99/4/30	4796.0	42.1
15	00/3/8	6040.6	36.0
16	00/4/10	4375.9	36.9
17	00/4/17-00/4/21	10845.5	47.2
18	00/4/27, 00/4/30	8439.8	41.3
19	01/2/16	4739.7	38.8
20	01/3/25	4054.3	40.7
21	01/4/15	3832.1	47.7
22	01/4/30	3967.0	50.0
23	01/10/6	6346.9	37.2
24	02/2/24	5418.9	38.0

Table 3 –Episodes based on the 80th percentile detection algorithm (excluding May-September). The highest daily ^{7}Be activity concentration and the highest average daily maximum ozone concentration are indicated for each episode.

3.2 ^{7}Be Only Algorithm

In order to alleviate the problems inherent in all three of the 80th percentile algorithms, it is necessary to select the days in which the ^{7}Be activity concentration is high and then analyze the ozone data. For this algorithm a threshold ^{7}Be activity concentration of 6000 μBqm^{-3} was selected. This threshold activity concentration is based on previous studies by Dutkiewicz and Husain (1979). The 6000 μBqm^{-3} threshold activity concentration algorithm identified 51 episodes, which are listed in Table 4. Figure 15 shows the daily ^{7}Be activity concentration, the average daily maximum temperature, the average daily maximum ground level ozone concentration

Episode	Dates (yy/mm/dd)	Max ^{7}Be (μBqm^{-3})	Max [O_3] (ppb)
1	96/5/9-96/5/10, 96/5/12, 96/5/15-96/5/17	9456.5	49.4
2	96/7/3	6007.4	22.3
4	96/7/28	6677.1	68.5
5	96/9/11-96/9/12	7586.3	33.1
6	96/10/1-96/10/3, 96/10/7-96/10/8	11673.0	21.6
7	96/10/30-96/10/31	12978.6	22.2
8	96/11/4	9601.0	19.2
9	96/12/26-96/12/27	7022.6	23.4
10	97/1/13-97/1/16	8658.5	17.9
11	97/1/27	8623.4	16.9
12	97/2/5-97/2/11	12937.3	19.8
13	97/4/12-97/4/13	10718.8	47.2
14	97/5/10-97/5/15, 97/5/19-97/5/20	9290.6	67.3
15	97/6/12	7451.0	23.7
16	97/8/10-97/8/11	6835.3	49.8
17	97/9/23-97/9/25	8197.8	32.1
18	97/10/2	6824.6	28.4
19	97/10/19-97/10/22	9078.2	15.8
20	97/11/14	6067.5	8.7
21	97/12/3-97/12/5	8213.1	9.6
22	98/3/20	6332.2	32.2
23	98/4/21-98/4/23	8176.9	45.5
24	98/4/29-98/5/2	8320.9	51.1
25	98/9/7	8077.3	40.4
26	98/12/21	6370.3	28.7
27	99/4/18	6309.8	43.6
28	99/5/6	6070.8	39.1
29	99/5/27	6211.0	49.6
30	99/11/3	7449.4	27.8
31	00/1/30	6617.7	23.7
32	00/2/5	6254.9	13.6
33	00/2/14-00/2/15, 00/2/17-00/2/20	8519.7	30.3
34	00/3/8-00/3/9	8267.3	36.0
35	00/4/18-00/4/20	10845.5	47.2
36	00/4/27, 00/4/30	8439.8	41.3
37	00/5/26	6814.2	33.2
38	00/6/3-00/6/5	8408.7	53.6
39	00/9/27-00/9/28	7355.9	33.1
40	00/10/7-00/10/8	8865.9	27.2
41	00/12/14	6181.9	18.5
42	01/1/3	6037.8	11.2
43	01/1/8	8980.1	20.9
44	01/1/24	6233.0	11.2
45	01/3/23-01/3/24	8366.5	32.9

46	01/5/8, 01/5/11-01/5/12	7760.6	49.9
47	01/10/5-01/10/6	9118.6	37.2
48	01/11/10-01/11/12	7080.7	17.6
49	01/11/19	8334.9	29.7
50	02/2/16-02/2/17	8168.5	20.4
51	02/2/26-02/2/27	7553.7	31.3

Table 4 - Episodes based on the ^{7}Be detection algorithm. The highest daily ^{7}Be activity concentration and the highest average daily maximum ozone concentration are indicated for each episode.

and the coefficient of variation of ozone of four of these episodes. Graphs of all the episodes can be found in Bovis and Steyn (2001).

Upon inspection of the graphs in Figure 15, two characteristics are common to most of the cases. Firstly, most of the 6000 μBqm^{-3} ^{7}Be episodes exhibit an activity concentration distribution starting at levels below 2000 μBqm^{-3} before rising to values exceeding 6000 μBqm^{-3}. The ^{7}Be activity concentration then remains at levels exceeding 6000 μBqm^{-3} for a period of one to seven days before returning to sub 2000 μBqm^{-3} levels. This indicates that stratospherically derived may have a substantial influence over ground level ozone concentrations over a period of several days. Secondly, the CV of ozone is probably not a reliable measure of the spatial variability of ozone.

In order to investigate the spatial and temporal variability of ozone, four urban stations and four rural stations were selected and their hourly ozone concentrations were plotted over the course of each episode. The stations used are listed in Table 5. Hourly ozone concentrations of four episodes corresponding to the episodes in Figure 15 are depicted in Figure 16. In Figure 16, each episode has two graphs. The first shows the hourly ground level ozone concentrations at the four urban stations and the second shows the hourly ground level ozone concentrations at the four rural stations.

a).

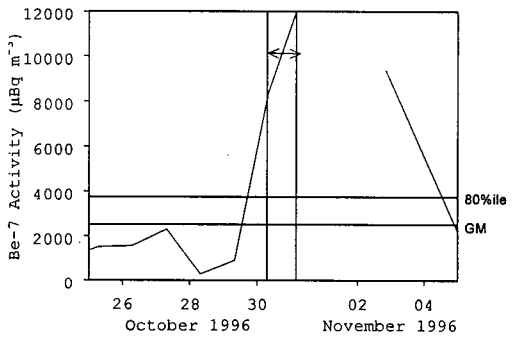
Be-7 Activity (μBq m⁻³)
12000
10000
8000
6000
4000
2000
0
80%ile
GM
26
28
30
02
04
October 1996
November 1996

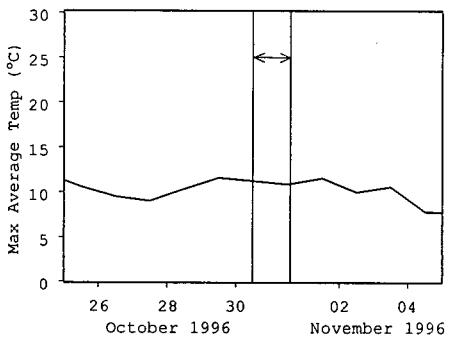
Max Average Temp (°C)
30
25
20
15
10
5
0
26
28
30
02
04
October 1996
November 1996

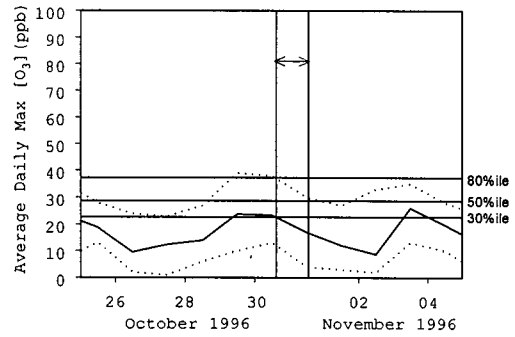
Average Daily Max [O3] (ppb)
100
90
80
70
60
50
40
30
20
10
0
80%ile
50%ile
30%ile
26
28
30
02
04
October 1996
November 1996

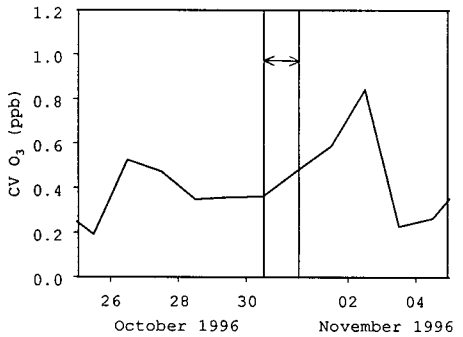
CV O3 (ppb)
1.2
1.0
0.8
0.6
0.4
0.2
0.0
26
28
30
02
04
October 1996
November 1996

b).

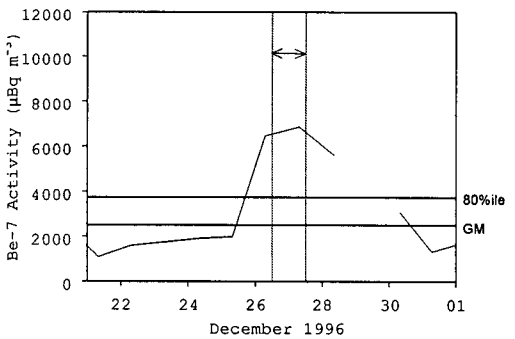
Be-7 Activity (μBq m⁻³)
12000
10000
8000
6000
4000
2000
0
80%ile
GM
22
24
26
28
30
01
December 1996

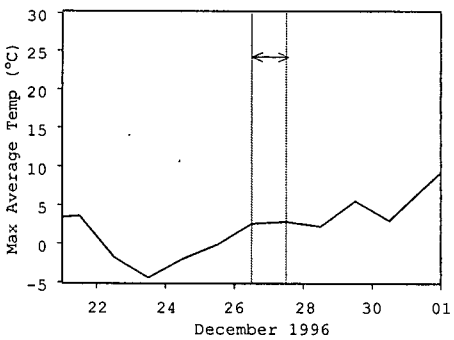
Max Average Temp (°C)
30
25
20
15
10
5
0
-5
22
24
26
28
30
01
December 1996

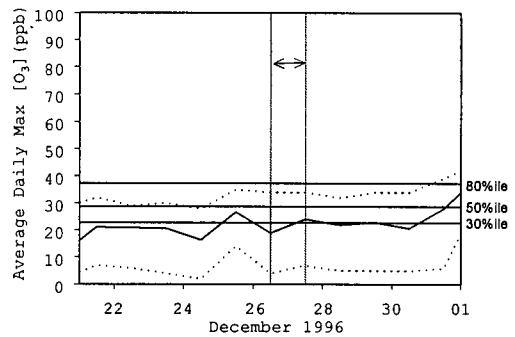
Average Daily Max [O3] (ppb)
100
90
80
70
60
50
40
30
20
10
0
80%ile
50%ile
30%ile
22
24
26
28
30
01
December 1996

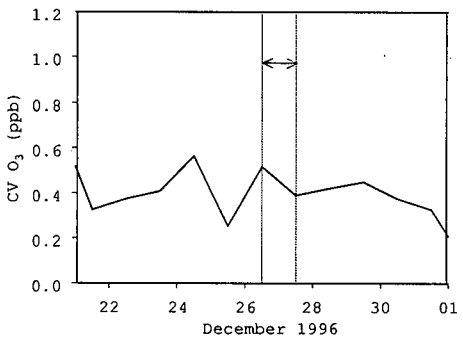
CV O3 (ppb)
1.2
1.0
0.8
0.6
0.4
0.2
0.0
22
24
26
28
30
01
December 1996

c).

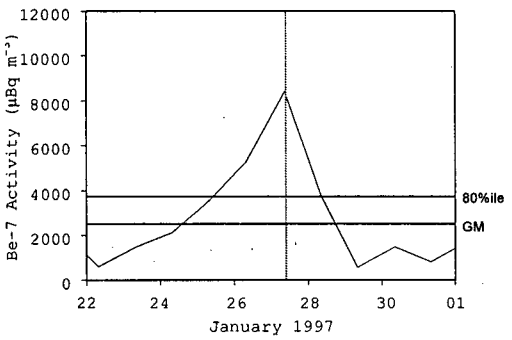
Be-7 Activity (μBq m⁻³)
12000
10000
8000
6000
4000
2000
0
80%ile
GM
22
24
26
28
30
01
January 1997

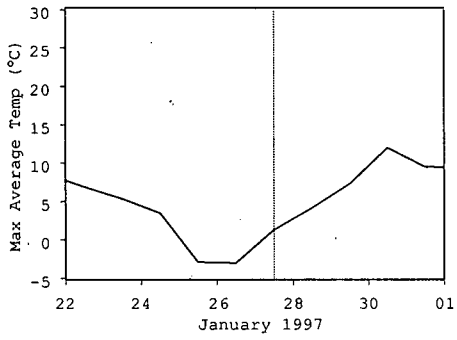
Max Average Temp (°C)
30
25
20
15
10
5
0
-5
22
24
26
28
30
01
January 1997

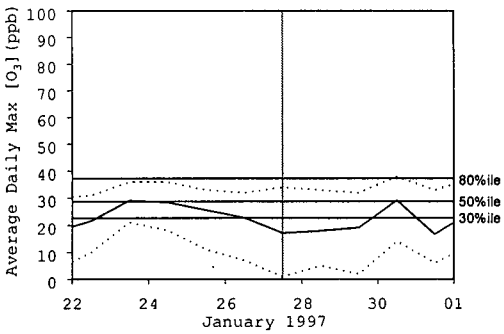
Average Daily Max [O3] (ppb)
100
90
80
70
60
50
40
30
20
10
0
80%ile
50%ile
30%ile
22
24
26
28
30
01
January 1997

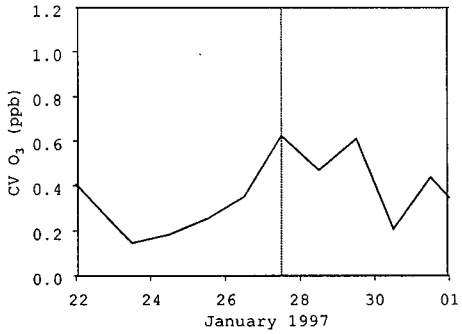
CV O3 (ppb)
1.2
1.0
0.8
0.6
0.4
0.2
0.0
22
24
26
28
30
01
January 1997

d).

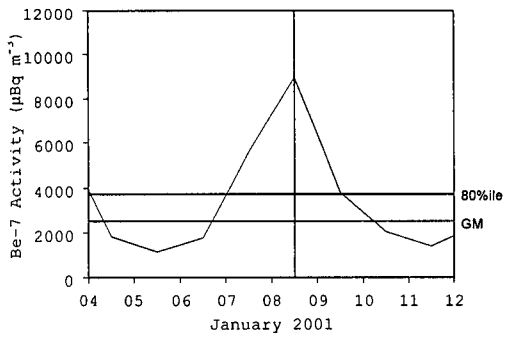
Be-7 Activity (μBq m⁻³)
12000
10000
8000
6000
4000
2000
0
80%ile
GM
04
05
06
07
08
09
10
11
12
January 2001

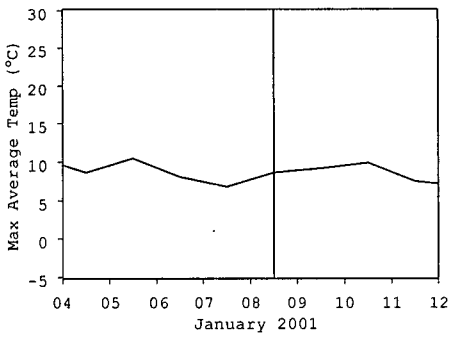
Max Average Temp (°C)
30
25
20
15
10
5
0
-5
04
05
06
07
08
09
10
11
12
January 2001

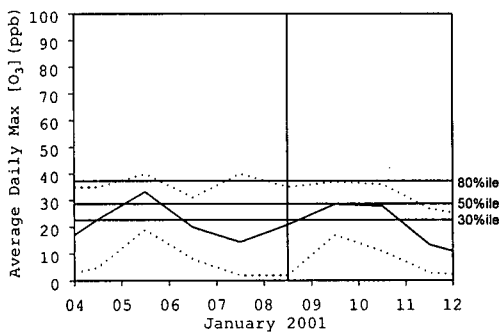
Average Daily Max [O3] (ppb)
100
90
80
70
60
50
40
30
20
10
0
80%ile
50%ile
30%ile
04
05
06
07
08
09
10
11
12
January 2001

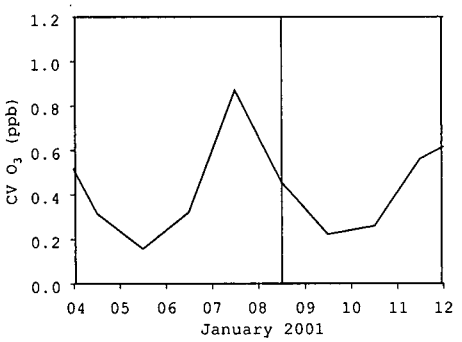
CV O3 (ppb)
1.2
1.0
0.8
0.6
0.4
0.2
0.0
04
05
06
07
08
09
10
11
12
January 2001

Figure 15 – ^{7}Be activity concentration, average daily maximum temperature, average daily maximum ozone concentration and coefficient of variance of ozone for a) 25 October 1996 – 5 November 1996, b) 21 December 1996– 1 January 1997, c) 22 January 1997 – 1 February 1997 and d) 4 January 2001 – 12 January 2001 from the ^{7}Be only detection algorithm. A single vertical line represents an episode in which both ^{7}Be and ozone were above the 80th percentile for one day only. Two vertical lines with an arrow between them indicate a multi-day episode. The graph on the upper left shows the daily ^{7}Be activity concentration. The top horizontal line indicates the 80th percentile value. Values above this line constitute the top 20% of all daily ^{7}Be activity concentrations in the data set. The lower line (marked GM) is the geometric mean daily ^{7}Be activity concentration for the entire data set. The graph on the upper right shows the average daily maximum temperature, which is found by selecting and then averaging the daily maximum temperatures measured at both Abbotsford International Airport and Vancouver International Airport (Figure 11). For the graph on the lower left, the solid line is the average daily maximum ground level ozone concentration. The upper dotted line is the highest hourly ozone concentration recorded over the entire network on a given day. The lower dotted line is the lowest daily maximum value recorded over the entire network on a given day. The upper horizontal line indicates the 80th percentile value, the middle line represents the median value and the lower line represents the 30th percentile value. The graph on the lower right shows the coefficient of variation (CV) of ozone which is the standard deviation of the daily maximum ground level ozone concentrations recorded across the network divided by the average daily maximum ground level ozone concentration.

Urban		Rural	
Station #	**Station Name**	**Station #**	**Station Name**
T001	Downtown Vancouver	T012	Chilliwack Airport
T002	Kitsilano	T015	Surrey East
T017	Richmond South	T027	Langley Central
T021	Port Coquitlam North	T029	Hope Airport

Table 5 - GVRD Air Quality Monitoring stations used in the hourly ozone concentration graphs in Figure 16. The locations of these stations can be found in Figure 11.

Before analyzing the urban and rural graphs of episodes in which ^{7}Be activity concentrations exceeded 6000 μBqm^{-3} (Figure 16), it is instructive to compare them to graphs of episodes in which the ^{7}Be activity concentrations are low. Figure 17 shows a high temperature low ^{7}Be episode. The general pattern in such episodes is a pronounced diurnal variability in the ground level ozone concentration. The maximum concentration usually occurs in the early afternoon hours with concentrations usually falling to below 10 ppb of ozone during the nocturnal hours, which is due to scavenging of ozone by NO_x (NRC 1992, Wayne, 1999). Figure 18 shows a low temperature episode, in which the ^{7}Be activity concentrations are also low. The general diurnal pattern is not as pronounced as the diurnal pattern in Figure

a).

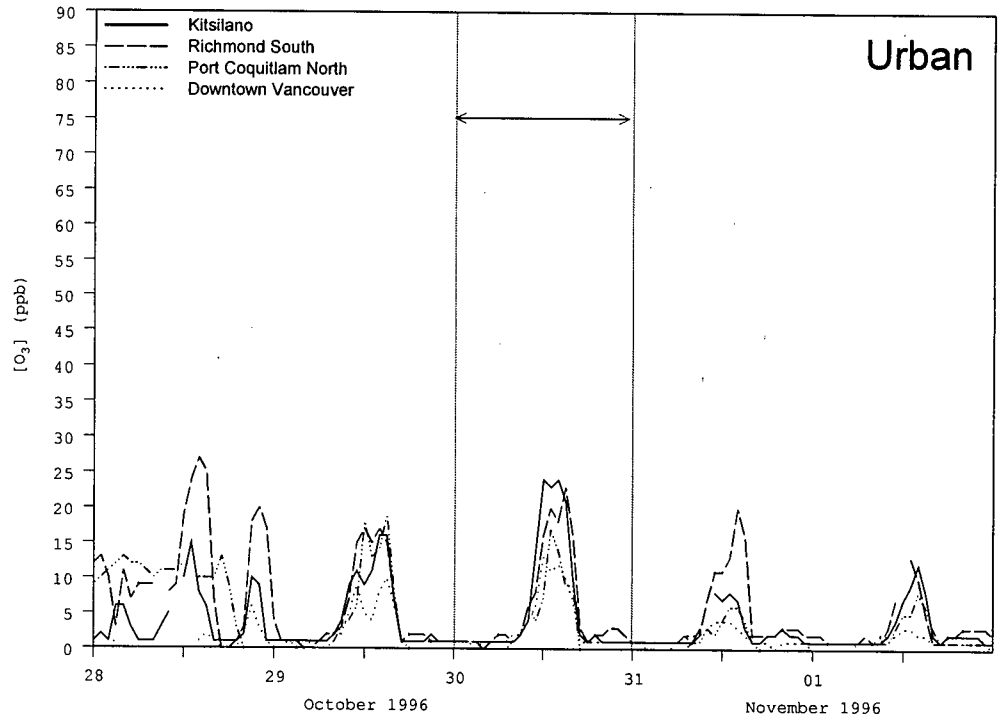
Kitsilano
Richmond South
Port Coquitlam North
Downtown Vancouver
Urban
[O3] (ppb)
90
85
80
75
70
65
60
55
50
45
40
35
30
25
20
15
10
5
0
28
29
30
31
01
October 1996
November 1996

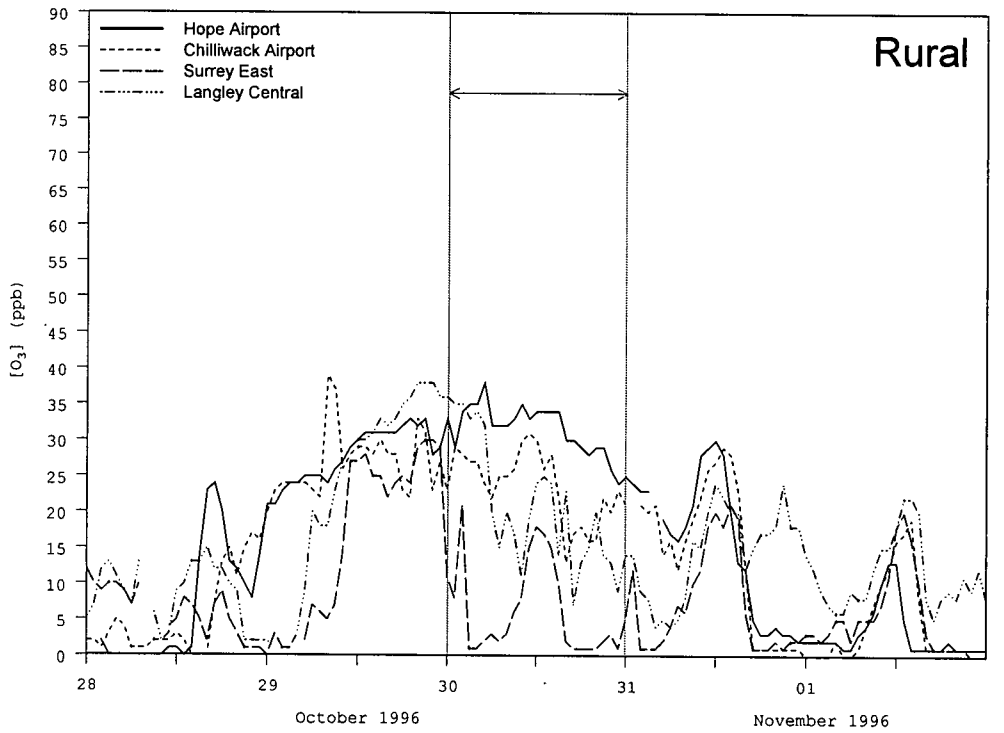
Hope Airport
Chilliwack Airport
Surrey East
Langley Central
Rural
[O3] (ppb)
90
85
80
75
70
65
60
55
50
45
40
35
30
25
20
15
10
5
0
28
29
30
31
01
October 1996
November 1996

b).

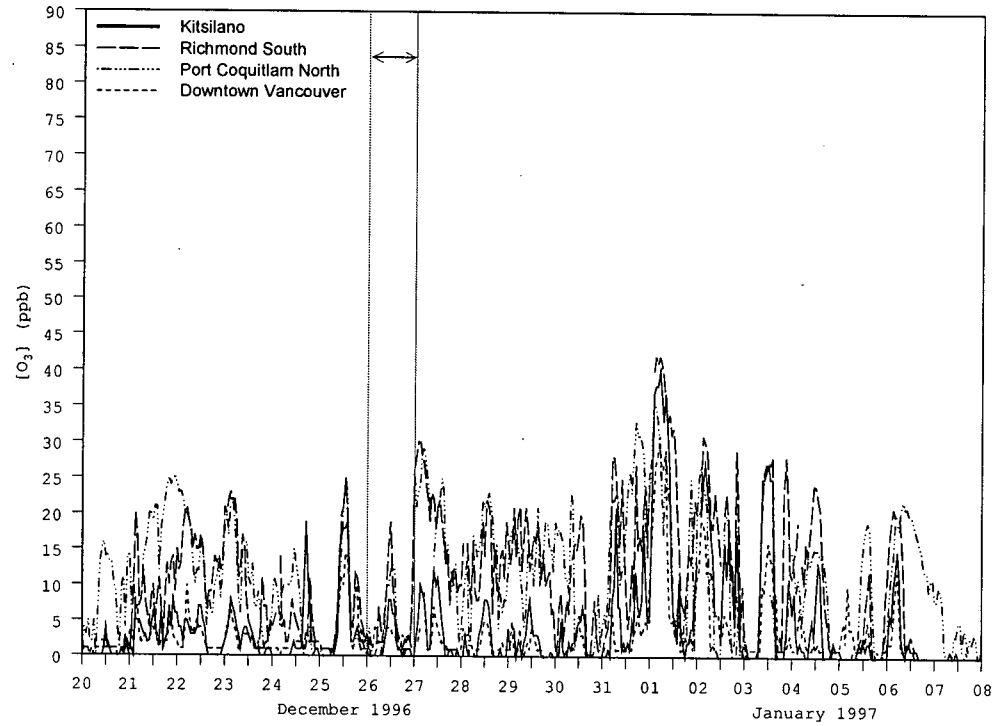
Kitsilano
Richmond South
Port Coquitlam North
Downtown Vancouver
[O3] (ppb)
December 1996
January 1997

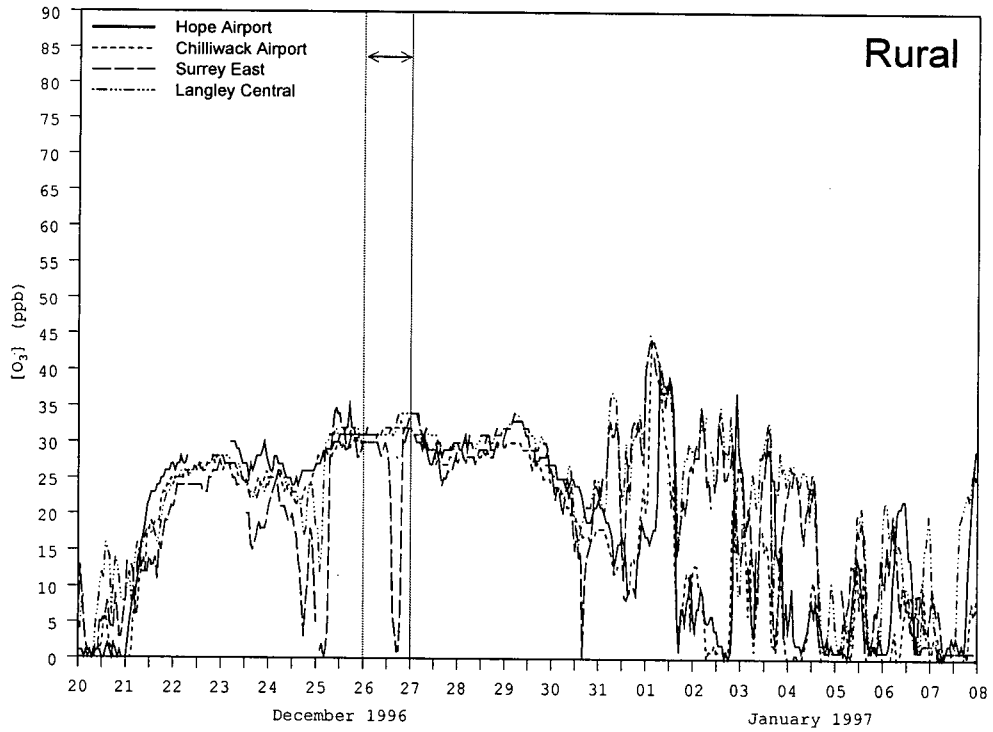
Hope Airport
Chilliwack Airport
Surrey East
Langley Central
Rural
[O3] (ppb)
December 1996
January 1997

c).

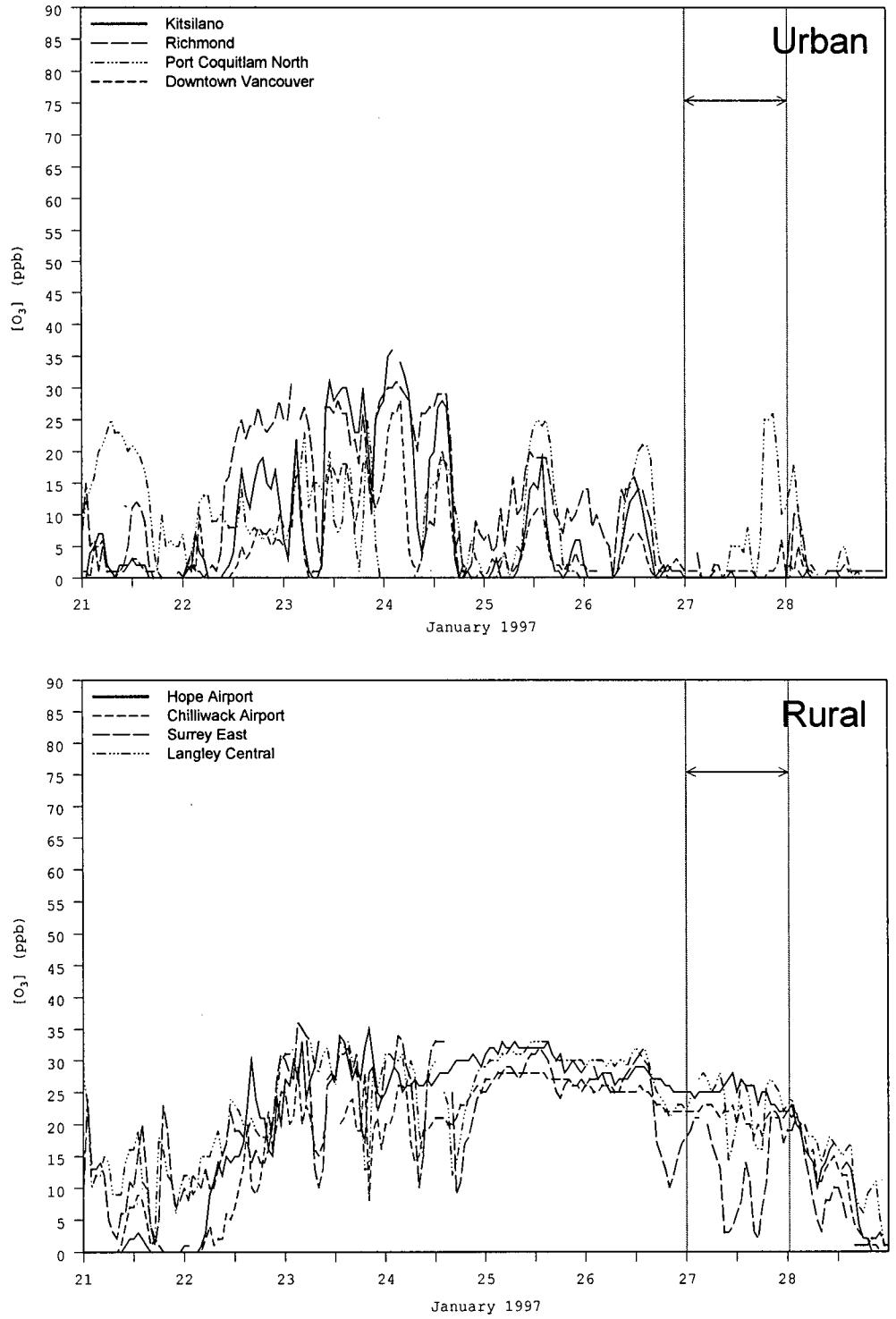
Kitsilano
Richmond
Port Coquitlam North
Downtown Vancouver
Urban
[O3] (ppb)
January 1997
Hope Airport
Chilliwack Airport
Surrey East
Langley Central
Rural
[O3] (ppb)
January 1997

d).

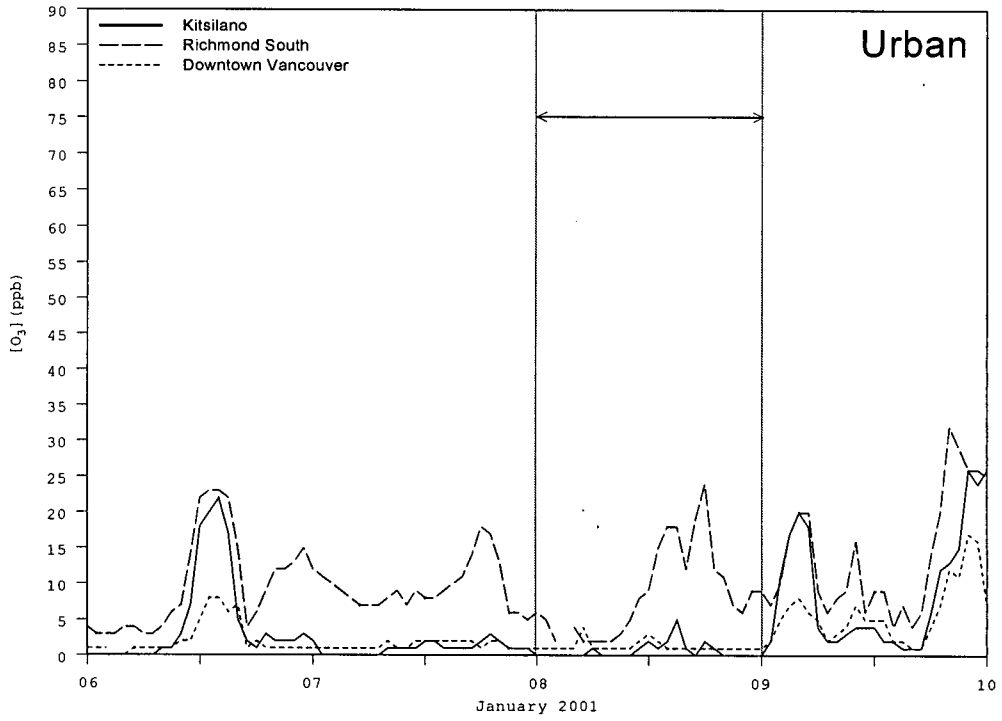
Kitsilano
Richmond South
Downtown Vancouver
Urban
[O3] (ppb)
January 2001

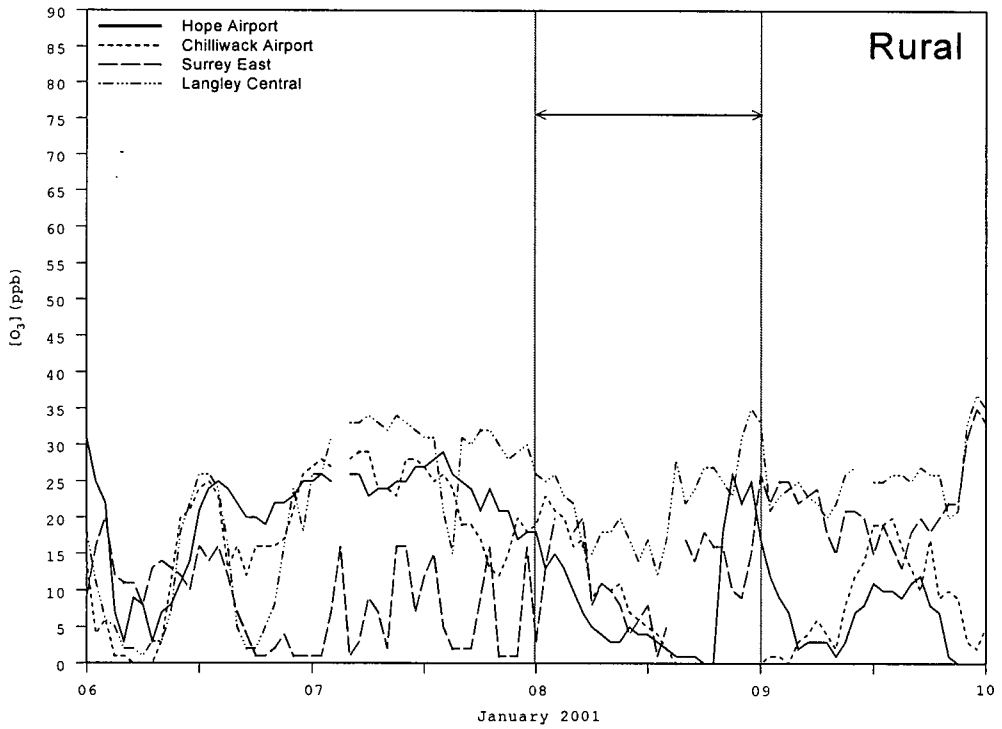
Hope Airport
Chilliwack Airport
Surrey East
Langley Central
Rural
[O3] (ppb)
January 2001

Figure 16 (previous pages) - Hourly ozone concentrations measured at Kitsilano, Richmond South, Port Coquitlam North and Downtown Vancouver urban air quality monitoring stations (top graph) and Hope Airport, Chilliwack Airport, Surrey East and Langley Central rural air quality monitoring stations in the Greater Vancouver Regional District for a) 28 October 1996 – 1 November 1996, b) 20 December 1996 – 7 January 1997, c) 21 January 197 – 28 January 1997 and d) 6 January 2001 – 9 January 2001. Two vertical lines separated by an arrow indicate the duration during which the daily ^{7}Be activity concentration remained above 6000 μBqm^{-3}.

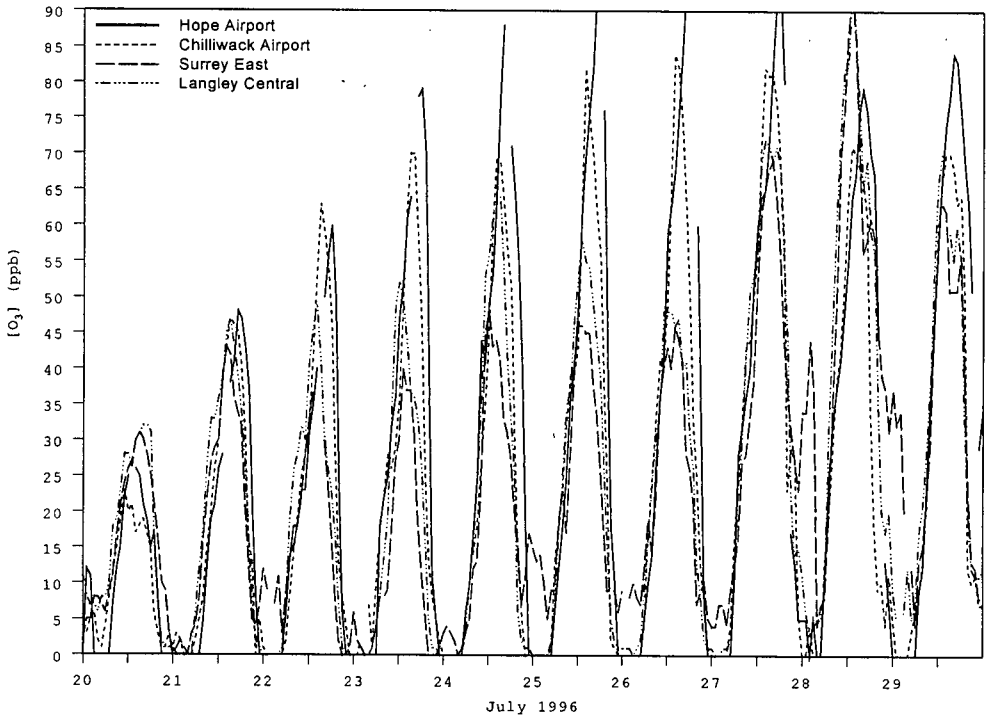

Figure 17 - Hourly ozone concentrations measured Hope Airport, Chilliwack Airport, Surrey East and Langley Central rural air quality monitoring stations in the Greater Vancouver Regional District for 20 July 1996 – 29 July 1996.

17. This may be because very little ozone is produced from anthropogenic precursor pollutants as the ground level ozone concentration rarely rises above 20-25 ppb.

All of the examples in Figure 16 have two distinct characteristics. Firstly, all of the urban ozone stations show very low ozone concentrations during the entire episode. This could be due to NO_x scavenging ozone in the urban areas. Secondly, all of the rural areas exhibit peak ozone concentrations that do not rise above 40 ppb during any of the episodes, but, during most of the episodes, the concentration remains fairly constant and there seems to be very little nocturnal NO_x scavenging.

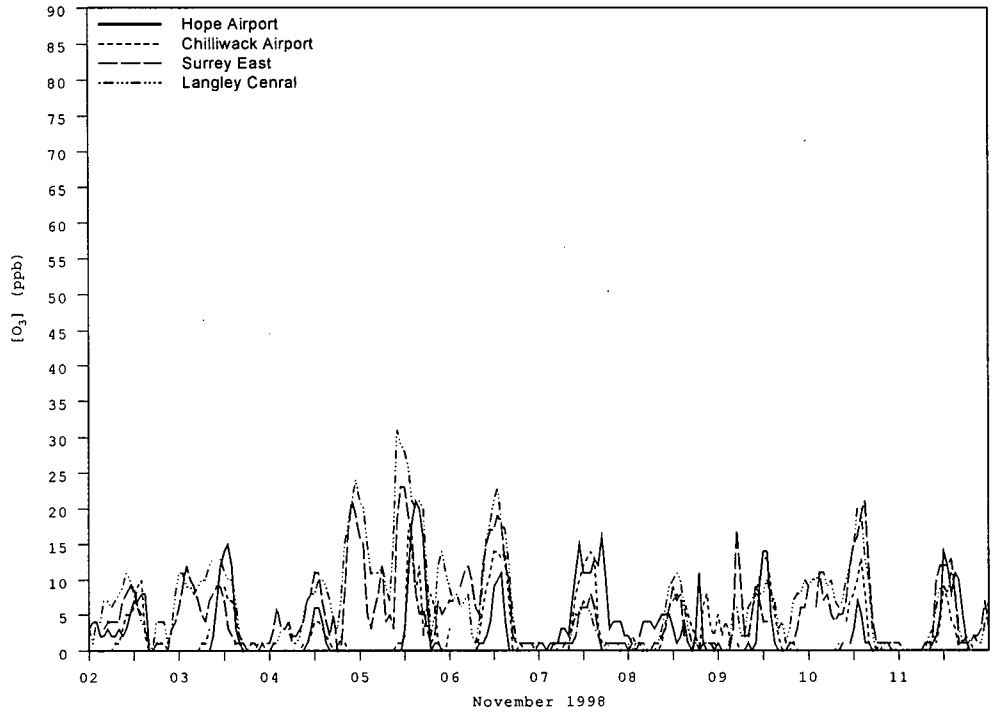

Figure 18 - Hourly ozone concentrations measured Hope Airport, Chilliwack Airport, Surrey East and Langley Central rural air quality monitoring stations in the Greater Vancouver Regional District for 2 November 1998 – 11 November 1998.

This characteristic is especially evident at Hope (T29 in Figure 11) and Chilliwack (T12) Airports and less so in Langley Central (T27) and Surrey East (T15).

3.3 Summary

Figures 19-22 show the total number of days in each month during which both ozone and ^{7}Be exceeded the 80th percentile (all data, exluding June - August and excluding May – September) and during which the daily ^{7}Be activity concentration was greater than 6000 μBqm^{-3} respectively. Upon inspection of the 80th percentile graphs (Figures 19-21), April and May contain the greatest number of days during which both ozone and ^{7}Be are in the 80th percentile. It may be tempting to perform stratospheric ozone case studies during these particular months in Section 4. Unfortunately, these months do contain several days during which the average daily maximum temperature exceeds 20°C. Because of this, the influence of locally

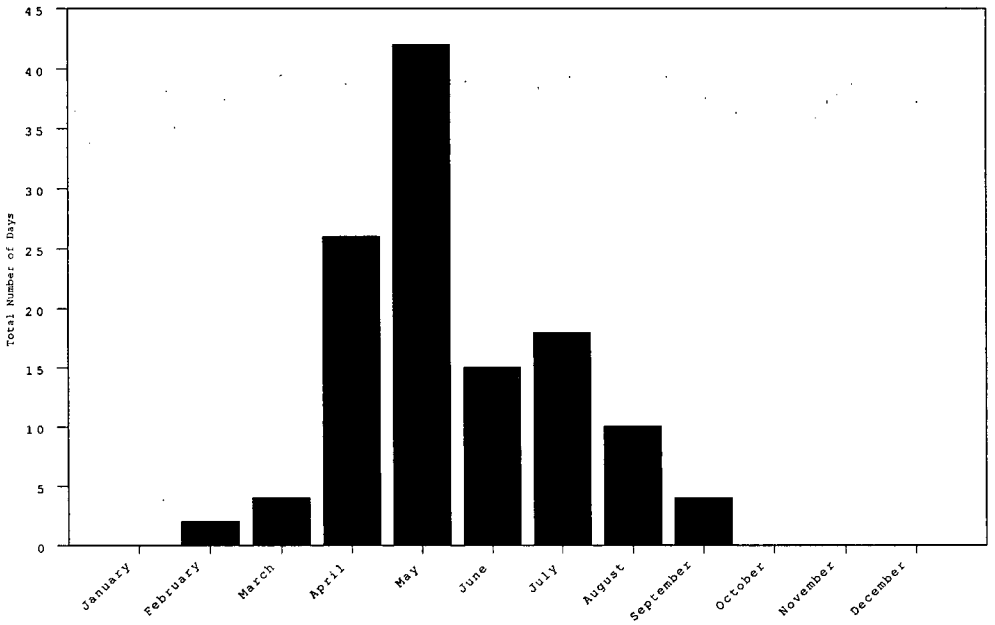

Figure 19 - Total number of days in a month in which both the daily ^{7}Be activity concentration and the average daily maximum ozone concentration exceeded the 80th percentile (all data) at the CTBTO IMS station CA002 during the period 9 April 1996 - 12 March 2002.

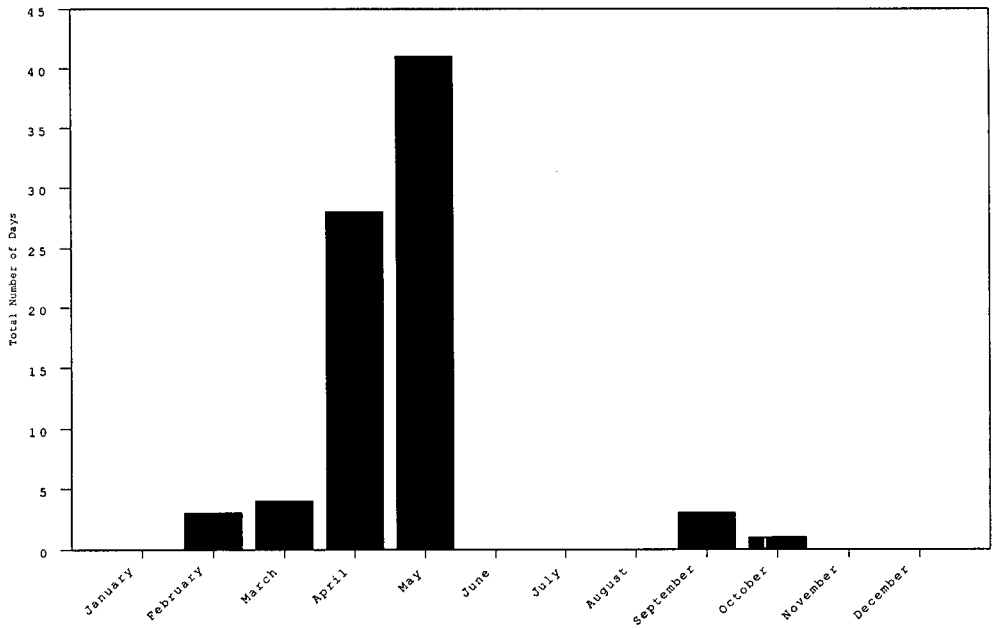

Figure 20 - Total number of days in a month in which both the daily ^{7}Be activity concentration and the average daily maximum ozone concentration exceeded the 80th percentile (excluding June - August) at the CTBTO IMS station CA002 during the period 9 April 1996 - 12 March 2002.

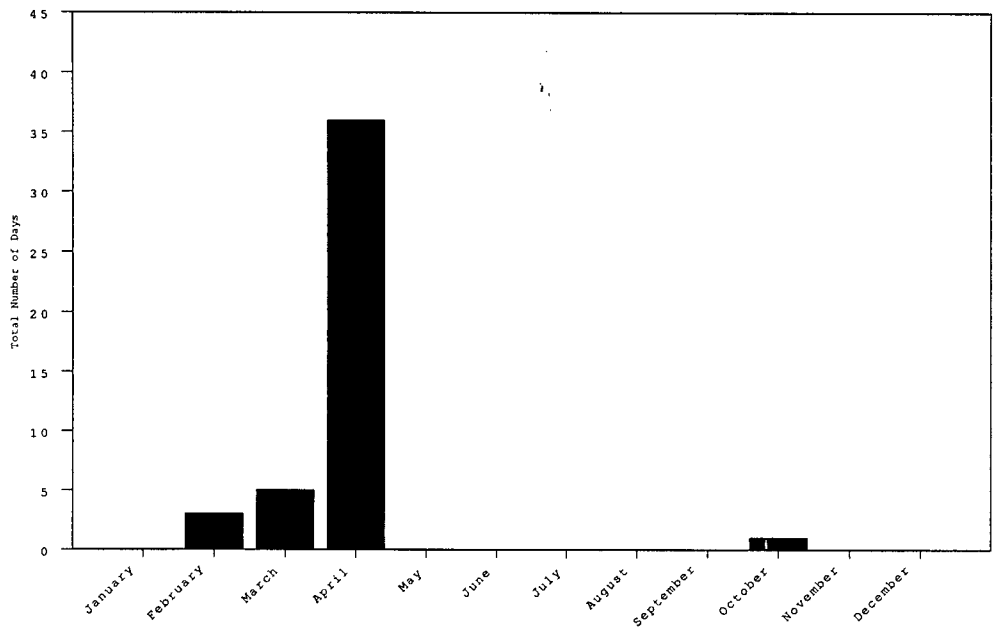

Figure 21 - Total number of days in a month in which both the daily ^{7}Be activity concentration and the average daily maximum ozone concentration exceeded the 80th percentile (excluding May - September) at the CTBTO IMS station CA002 during the period 9 April 1996 - 12 March 2002.

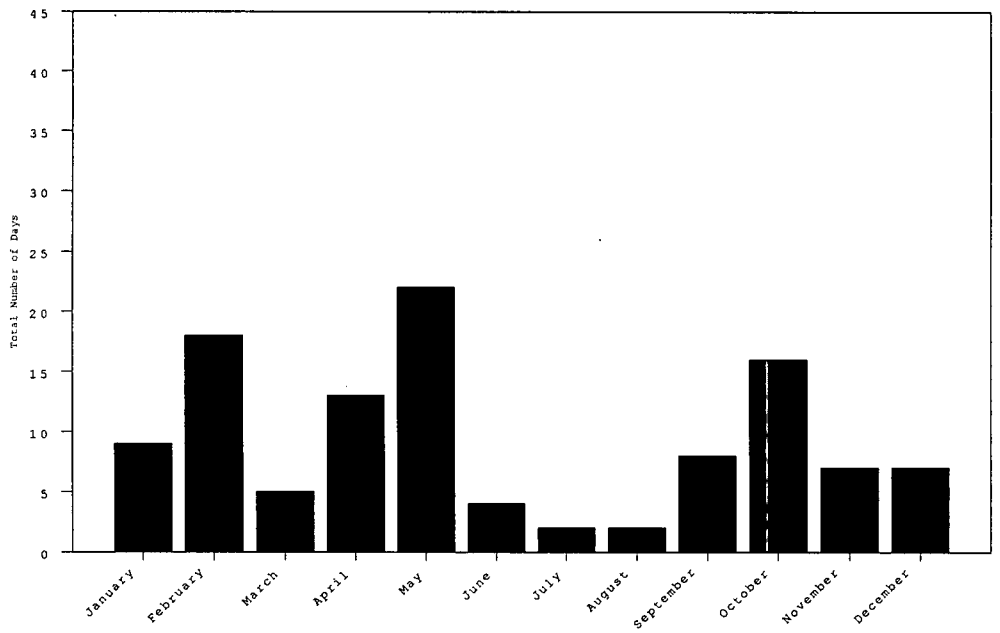

Figure 22 - Total number of days in a month in which the daily ^{7}Be activity concentration exceeded 6000 μBqm^{-3} at the CTBTO IMS station CA002 during the period 9 April 1996 - 12 March 2002.

produced anthropogenically derived ozone can not be ruled out. Case studies in Section 4 should therefore be carried out during months during which both the average daily maximum temperature is low (Figure 14) and the ^{7}Be concentration is high (Figure 22). Although the average daily maximum ozone concentration will be low during these periods, the low temperatures will ensure that a greater portion of the ground level ozone concentration in the LFV will have originated from natural, possibly stratospheric, sources.

4. Back Trajectories and Case Studies

Meteorological trajectories are an important tool in stratosphere-troposphere exchange research (Stohl *et al.*, 2000, 2002, Stohl and Trickl, 1999, Ancellet *et al.*, 1991, Bonasoni *et al.*, 2000, Danielsen, 1968). A trajectory is the time integration of the position of a parcel of air as it is transported by the wind (Stohl *et al.*, 2002). The parcel's passive transport by the wind is computed from the average of the three-dimensional velocity vectors at the particle's initial-position P(t) and its first-guess position P'(t+dt) (READY website). The velocity vectors are interpolated in both space and time. The first guess position is:

$$P'(t+dt) = P(t) + V(P,t)dt$$

where V(P,t) is the velocity at the particle's initial position. The final position is:

$$P(t+dt) = P(t) + \frac{[V(P,t) + V(P',t+dt)]}{2} dt$$

Trajectories may be integrated both forward and backward in time (READY website).

Meteorological back trajectories are an important part of the current research because of their ability to determine the source altitude and location of near surface air in the LFV during episodes in which air of stratospheric origin is believed to be influencing ground level ozone concentrations. Once back trajectories have been

calculated for a particular episode, meteorological analysis will be used to relate the trajectory paths to the overall synoptic situation.

Early research utilizing meteorological trajectories required either an immense amount of computing power or the trajectories had to be computed by hand (Danielsen, 1968). Trajectory calculations were thus considered costly and impractical for general use save for the largest research projects (Danielsen, 1968, Danielsen *et al.*, 1970, 1977). With the increase in the availability of fast desktop PC's and workstations, trajectory analysis has become an important tool for many fields of atmospheric research such as stratosphere-troposphere exchange (Stohl *et al.*, 2000, 2002, Stohl and Trickl, 1999, Ancellet *et al.*, 1991, Bonasoni *et al.*, 2000), volcanic ash (Heffter and Stunder, 1993) and air pollution dispersion (Fast and Berkowitz, 1997, Gislason and Prahm, 1983).

Several trajectory models are widely used in many fields of research. Some examples are the FLEXTRA (FLEXible TRAjectory) model developed at the Technical University of Munich in Germany (Stohl et al. 1995, Baumann and Stohl, 1997, Stohl and Seibert, 1998), the HYSPLIT (Hybrid Single Particle Lagrangian Integrated Trajectory) model developed by the NOAA Air Resources Laboratory in the USA (Draxler and Hess, 1997) and the CANERM (CANadian Emergency Response Model) developed at the Canadian Meteorological Center in Dorval, Canada (Pudykiewicz, 1988, Pudykiewicz, 1989).

4.1 Previous Research

The bulk of previous research involving trajectory analysis of STE has been conducted in mountainous regions around the world, most importantly in the Swiss Alps because air of stratospheric origin has had little chance to dilute at these

altitudes. The following three papers, published over the last 12 years, outline some of the previous work.

The study conducted by Ancellet *et al.* (1991) used a ground-based lidar at the Observatoire de Haute Provence (OHP) in France to determine a coarse value of the total outflow of ozone from the stratosphere to the troposphere due to frontal activity. Trajectory analyses were used for several cases to determine whether the elevated ozone concentrations measured at the observatory were the result of STE. For each model run, trajectories were calculated at end points both directly overhead and 1° north, south, east and west of the observatory. The model input consisted of European Center for Medium Range Weather Forecasting (ECMWF) three dimensional mean wind fields at a resolution of 2° x 2°. Using these trajectory calculations for an elevated ozone case that occurred on 28-29 March 1988, it was found that surface air at OHP originated from a tropopause fold northeast of England two days earlier. Using the ozone lidar at OHP, Ancellet *et al.* (1991) estimated that a total of 2×10^{33} ozone molecules were transferred via the tropopause fold. This number was multiplied by the average annual number of tropopause folds to give an approximate value for the total ozone outflow from the stratosphere in the Northern Hemisphere (1.5×10^{36} molecules yr^{-1}). This number is lower than values obtained from previous studies ($3.5\text{-}6.1\times10^{36}$ molecule yr^{-1}) because this study did not include the ozone outflow generated by cutoff lows (Danielsen and Mohnen, 1977).

Bonasoni *et al.* (2000) used a variety of meteorological data including trajectory analysis, water vapor satellite imagery, ozone soundings, ground based air quality monitoring and synoptic charts to describe a stratospheric intrusion event at Mt. Cimone (2165 m a.s.l.) in the Northern Apennines in Northern Italy. The case study took place on 11-12 March 1996 during the Vertical Ozone Transport in the Alps

(VOTALP) field study. Around midday on 12 March an ozone concentration of approximately 110ppb was measured at Mt. Cimone. An ensemble of trajectory end points situated around the Mt. Cimone area was set up using the FLEXTRA trajectory model to determine the source region of this ozone rich air. The bulk of the resulting trajectory pathways showed that the air around the Mt. Cimone area originated near Greenland seven days earlier. This air then became incorporated into a cut off low over Central Europe prior to its arrival over Mt. Cimone. Thirty six hours earlier the trajectory paths originated at low levels over Northwestern Italy, suggesting an anthropogenic source. During this case study, trajectory analysis was essential as it was able to rule out ozone of anthropogenic origin during the elevated ozone event.

Another case study that occurred during the VOTALP project was investigated by Stohl and Trickl (1999). Between midday on 28 March and early evening on 29 March 1997 ozone concentrations between 60-80ppb were observed at the Jungfraujoch observatory in the Swiss Alps. During this time, the relative humidity (RH) fell to nearly 10% at Jungfraujoch starting at midday on 28 March and persisted until midday on 29 March. These low RH values suggested that air of stratospheric origin was heavily influencing the ground level ozone concentrations. After midday on 29 March, the RH rose to about 90%, yet the ozone concentrations remained elevated thus suggesting a possible anthropogenic influence on ground level ozone concentrations. In order to investigate the source regions of these two air masses, the FLEXTRA trajectory model was utilized, using ECMWF 1° x 1° mean wind fields. After analyzing the trajectory results, Stohl and Trickl (1999) concluded that ozone concentrations measured at Jungfraujoch during the period of low relative humidity originated from a STE event over Northern Europe. Ozone concentrations measured

during the high relative humidity period were the result of long range transport of air that originated in the boundary layer over Eastern North America.

4.2 Trajectory Models and Procedures Used in the Current Research

4.2.1 HYSPLIT

The NOAA Air Resource Laboratory's (ARL) Hybrid Single Particle Lagrangian Integrated Trajectory (HYSPLIT) model is designed to support a wide range of simulations including long range transport (trajectories), particle dispersion and deposition. The model input into HYSPLIT is based on the NOAA Global Data Assimilation System (GDAS) three dimensional gridded wind fields. The GDAS model is run every six hours with start times at 00, 06, 12 and 18 UTC at one degree latitude-longitude resolution. ARL then interpolates the GDAS wind fields to a conformal map projection which reduces the resolution to 100km. The resulting modified GDAS model output is called ARL-packed FNL output. FNL output files are available for both the Northern and Southern Hemispheres. Each FNL file contains two weeks worth of compacted GDAS model output. The resulting FNL files are used as the model input for HYSPLIT.

4.2.2 CANERM

The capabilities of the Canadian Meteorological Center's (CMC) CANadian Emergency Response (CANERM) model are similar to HYSPLIT. The model runs performed on CANERM used three dimensional mean wind fields from the NCEP (National Center for Environmental Prediction) Reanalysis model output with a latitude-longitude grid resolution of 1° degree. The NCEP reanalysis is available every six hours at 00, 06, 12 and 18 UTC. The NCEP reanalysis output is based on a project to recover archived data such as land surface, ship, rawinsonde, pibal, aircraft, satellite and other data. These data are then quality controlled and assimilated with a

data assimilation system, which is kept unchanged over the reanalysis period. This eliminates perceived climate jumps associated with changes in the data assimilation system. Further information on the NCEP reanalysis project can be found in Kalnay *et al.* (1996).

4.2.3 Trajectory Model Procedure

Twenty seven trajectories were calculated around the LFV area for each model run during an episode. Of these 27 trajectories, nine were calculated starting at 100m a.g.l. (above ground level), nine were calculated starting at 500m a.g.l. and nine were calculated starting at 1000m a.g.l. The nine end point receptors at each of the three levels are identical. Eight of these endpoints are evenly distributed around the edge of a 1°x1° square centered around 49.25°N latitude 123.25°W longitude. The ninth endpoint receptor is located at the center of the 1°x1° square. The total duration of each back trajectory is 144 hours and the position of each trajectory is recalculated every hour.

4.3 Case Studies

In order to better understand the meteorological phenomena that occur both prior to, and during an elevated ground level ozone concentration episode in the LFV that is believed to have been the result of STE, a set of four episodes were selected for more detailed study. During each case study, synoptic analysis, satellite imagery (where available), temperature and precipitation, back trajectory analysis, ozone concentration and ^{7}Be activity concentration data were utilized. These case studies were not selected randomly from the identified episodes. Instead, they were selected based on a detailed set of criteria listed below.

1. ^{7}Be exceeds a threshold activity concentration during the episode. The selection of the threshold activity concentration was based on previous studies.

Dutkiewicz and Husain (1979) suggested that a 24 hour ground level ^{7}Be activity of 6000 μBqm^{-3}, roughly one third of upper tropospheric values, indicates a recent upper atmospheric contribution of ^{7}Be.

2. Ozone concentrations remain elevated during most of the episode, especially during the night time hours.
3. The average daily maximum temperature must be below 20°C (see section 3.1.1).
4. A majority of the back trajectories from any one model run show a total descent of at least 4000 m - 5000 m over a six day period immediately prior to the trajectory's arrival in the LFV (Stohl *et al.*, 2000). This last criterion is implemented to ensure that lower tropospheric sources of ozone are kept to a minimum. It is entirely possible that ozone originating from 5000 m a.s.l. (above sea level) is of anthropogenic origin (i.e. long range transport). If the air mass at that altitude exhibits a high ^{7}Be activity concentration however, the possibility that the air mass is of stratospheric origin increases. Even if the ^{7}Be activity concentration at 5000 m a.s.l. is high, there is still a small chance that the air mass could still have an upper tropospheric origin because this region constitutes 25% of the ^{7}Be production. During the case study selection process, preference was given to episodes in which the bulk of the trajectory descent took place three to four days immediately prior to the trajectory's arrival in the LFV thus minimizing the influence of anthropogenically derived ozone along the trajectory path.

4.3.1 Case Study #1 - 28 October 1996 – 31 October 1996

4.3.1.1 Synoptic Overview

On 23 October 1996 at 0000 UTC, a large scale trough was present over most of the Northern Pacific Ocean. The trough axis was oriented northwest - southeast with its most intense portion (i.e. area of strongest gradient of geopotential height contours) located between 30°N-40°N latitude and 170°E longitude. In addition, a cut off low was located in the Arctic Ocean north of Alaska, USA with its center located at approximately 75°N latitude and 140°W longitude. Both features were present at least up to the 250 mb isobaric surface.

Over the next 36 hours, the wavelength of the Pacific trough began to decrease. At the same time, the amplitude of the trough began to increase and its axis changed to a more north - south orientation. At the same time, the cutoff low in the Arctic Ocean began to slowly track southwestward so that its center of rotation was located just to the north of Alaska.

On 25 October at 1200 UTC, the flow around the Pacific trough began to separate from the main flow allowing a cutoff low to develop at 500 mb. The cutoff low was not apparent at 250 mb. Immediately east of the cutoff low, a steep ridge began to develop over the northeastern Pacific Ocean and a trough over western North America began to dig southwards. The cutoff low centered over Northern Alaska did not move relative to its position 18 hours previously. These synoptic patterns on the 250 mb and 500 mb isobaric surfaces are shown in Figure 23 and Figure 24 respectively.

Over the next 72 hours, the Pacific cutoff low rejoined the main flow and the associated trough began to weaken. At the same time, the Northern Alaska cutoff low began to track eastwards so that its center was located just north of the Northwest Territories in Canada.

At the surface, several main synoptic processes took place. On 23 October at 0000 UTC a low was present over the central Alutian Islands located west of Alaska in the USA with a central pressure of about 984 mb. Over the next 72 hours, the low began to fill and track eastwards towards the Alaskan Panhandle.

Associated with the Pacific trough present at 0000 UTC on 23 October, a new low began to develop on the east side of the trough with a central pressure of 1011 mb. Over the next 48 hours, the low moved towards the east and deepened to 969 mb so that its center was now situated just south of the central Aleutian Islands. At the same time, the previous low that began to dissipate over the Alaskan Panhandle was incorporated into this low. After 25 October at 1800 UTC, this low began to track further east and fill as it came onshore over northern British Columbia. During the lifetime of this low, a large area of high pressure extending from the southeastern Pacific to Western North America began to develop. Besides a short lived low that developed over Southwestern British Columbia on 28 October at 1800 UTC, this high pressure pattern persisted for the duration of the elevated ozone episode in the LFV.

The final low pressure system to track over the Northern Pacific was the most intense with central pressures reaching 956 mb. The low developed over eastern Siberia on 24 October at 1800 UTC and over the next 72 hours it moved northeastward to northeast Russia where it reached its lowest central pressure (Figure 25). On 28 March at 0000 UTC, the low began to track further to the northeast where it began to steadily dissipate over the northern entrance to the Bering Straight.

4.3.1.2 Surface O_3 and ^7Be Concentrations and Temperature in the LFV

On 28 October at 0600 UTC (27 October at 2200 Pacific Standard Time), elevated ozone concentrations began to be measured in the LFV starting at Hope Airport (Figure 16a). Over the next 12 hours elevated ozone concentrations were

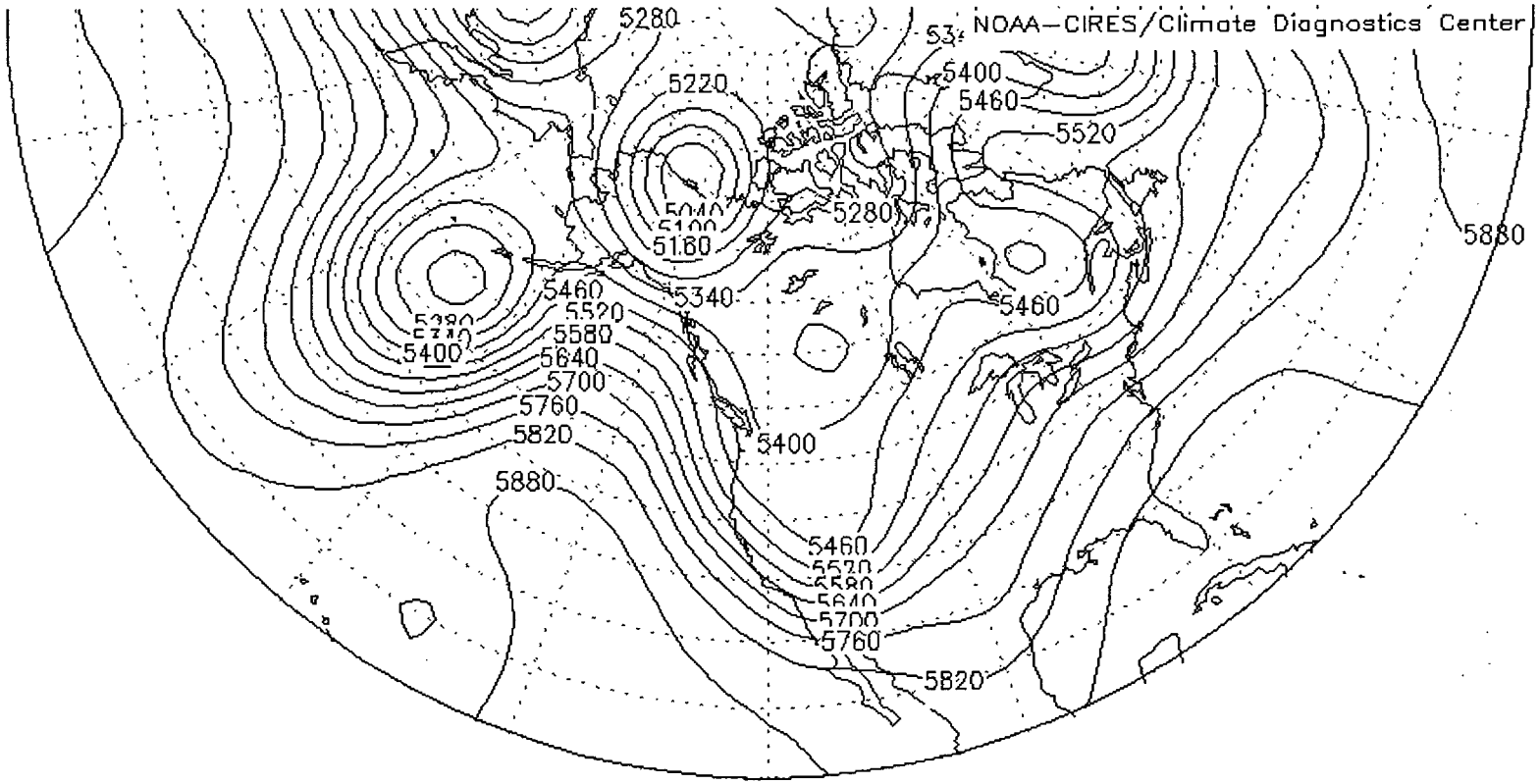

Figure 23 - 500 mb geopotential chart for 25 October 1996 at 1800 UTC. Image courtesy of the NOAA Climate Diagnostics Center.

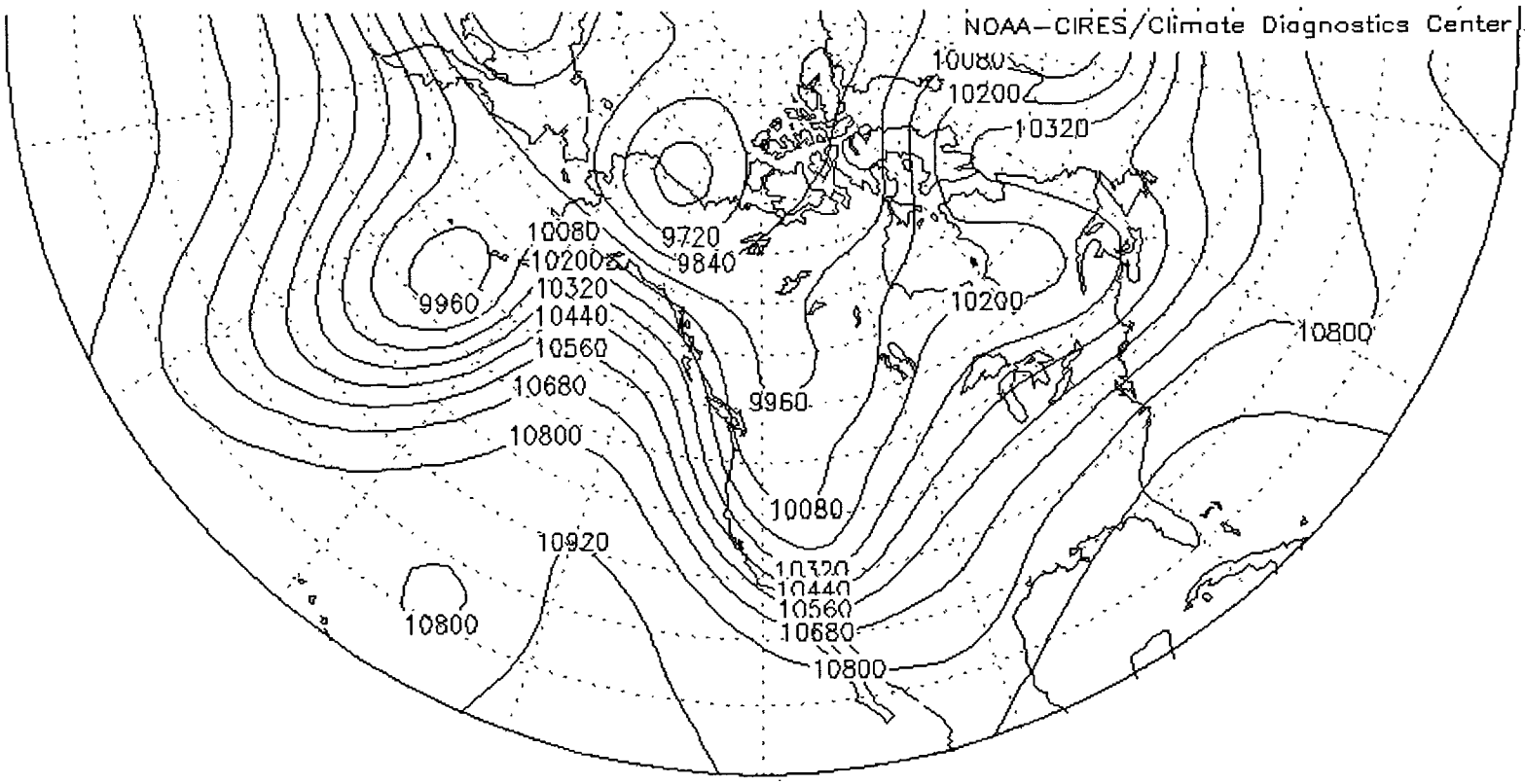

Figure 24 - 250 mb geopotential chart for 25 October 1996 at 1800 UTC. Image courtesy of the NOAA Climate Diagnostics Center.

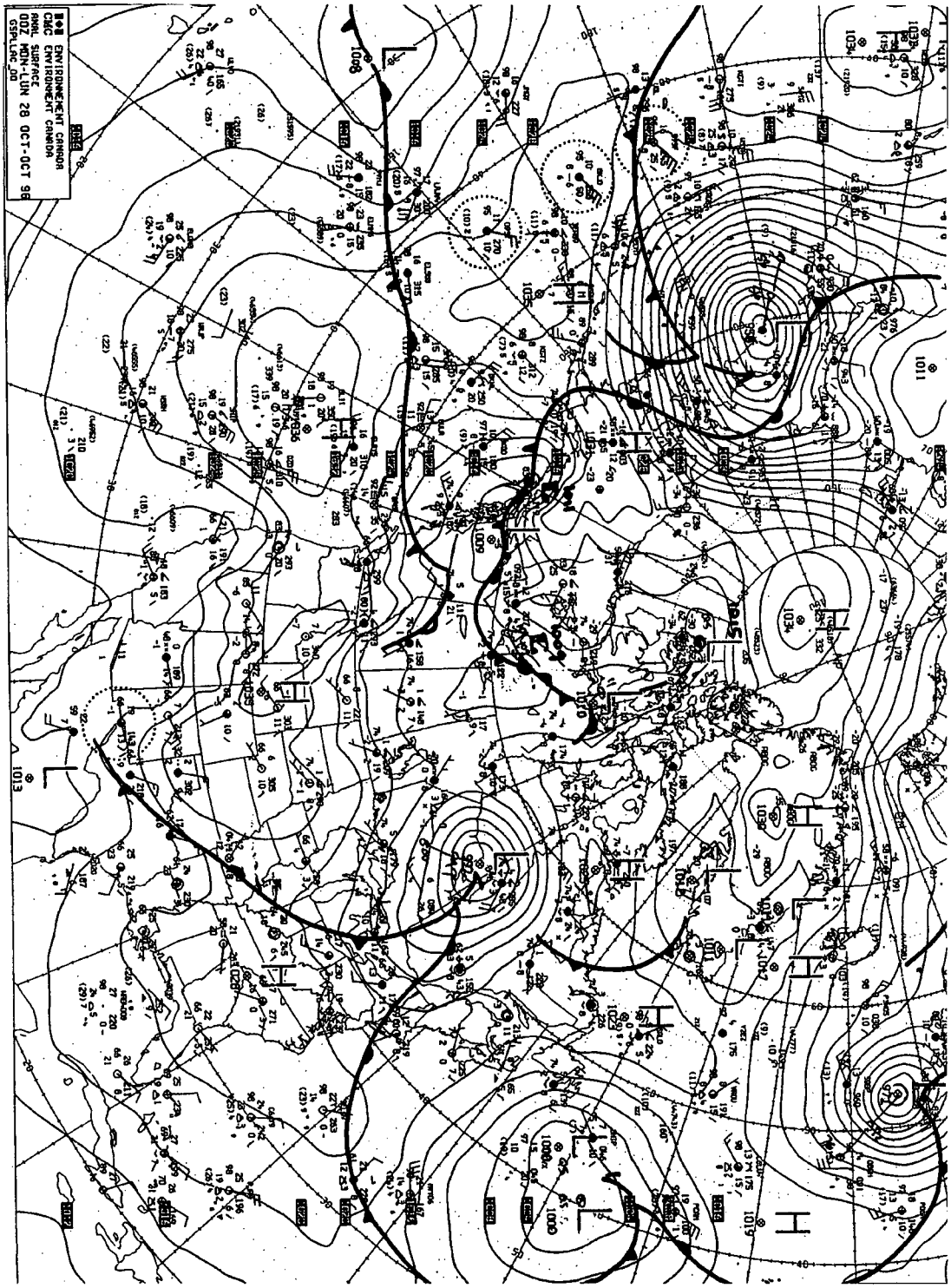
ENVIRONMENT CANADA
CMC ENVIRONMENT CANADA
ANAL SURFACE
00Z MON-LUN 28 OCT-OCT 98
GSPLAC_00

Figure 25 (previous page) – Surface isobaric chart for 28 October 1996 at 0000 UTC. Image courtesy of Environment Canada's Canadian Meteorological Center.

---

measured at Chilliwack Airport, Surrey East and Langley Central air quality stations. With the exception of Surrey East, these ozone concentrations remained at a roughly constant level during the entire five day episode with very little NO_x scavenging during the night time hours. The maximum 1 hour ground level ozone concentration measured at each rural station in Figure 16a during the episode ranged between 25-40 ppb.

At the urban stations, very little evidence of elevated ozone concentrations could be found (Figure 16a). The only exception occurred on 29 October at 0600 UTC (28 October at 2200 PST) when a small spike between 10-20 ppb was measured at the Kitsilano and Richmond South air quality stations.

During the episode, the average daily maximum (ADM) ozone concentration rose by 10 ppb from a pre-episode concentration of 14 ppb on 27 October to 24 ppb on 29-30 October (Figure 15a). The ADM ozone concentration deceased to 17 ppb by the end of the episode on 31 October. The coefficient of variance (CV) of ozone experienced a relative minimum during the entire episode with values ranging from 0.4 ppb between 28-30 October to 0.5 ppb on 31 October (Figure 15a). This relative minimum in CV of ozone signifies that the maximum daily ozone concentrations across the network were approaching a more common value compared to the maximum daily ozone concentrations immediately prior to and following the episode.

Although ozone concentrations remained elevated for four days, the ^{7}Be activity concentrations remained above 6000 μBqm^{-3} for two days only (30-31 October) (Figure 15a). A possible explanation for this would be that a heavy precipitation event occurred on 28 October. Vancouver International Airport (Figure 11) measured

50 mm of total precipitation on this day. Since ^{7}Be can be scavenged out of the atmosphere by precipitation (Feely *et al.*, 1989), it is likely that a large amount of ^{7}Be was scavenged out of the atmosphere above the LFV.

Over the course of the entire episode, the average daily maximum temperature remained fairly constant, ranging from 10°C-11°C.

4.3.1.3 Back Trajectory Analysis

Back trajectory analysis, performed between 30-31 October, when the daily ^{7}Be activity concentration measured at UBC exceeded 6000 μBqm^{-3}, revealed two major trajectory paths that air particles followed prior to their arrival over the LFV. Figure 26 shows six day back trajectories taken by particles of air that arrived over the LFV on 31 October at 0600 UTC. The first trajectory path followed the flow around the Pacific trough and originated as far away as North Central Siberia six days prior (Figure 26). All of the trajectories that arrived over the LFV at an altitude of 1000 m a.g.l. that traveled in the flow around this trough originated at a height of at least 5000 m a.g.l. Prior to their arrival in the LFV, these trajectory paths descended at a rate of 1.5-2.0 cms^{-1} between 27 October at 0600 UTC and 30 October at 0600 UTC. This rapid descent was probably due to the large surface high pressure region present over Alaska and the northern two thirds of British Columbia.

With the exception of four trajectory paths which originated at low levels over the northeastern Pacific, the remaining trajectories originated around the region of the North Alaskan cutoff low six days earlier. After exiting the cutoff low, these trajectories descended at a rate of approximately 2.0 cms^{-1} over three days before arriving over the LFV (Figure 26). Again, this rapid descent was probably caused by the two surface high pressure systems present over Alaska and British Columbia. These two major trajectory paths persisted for the entire period during which ozone

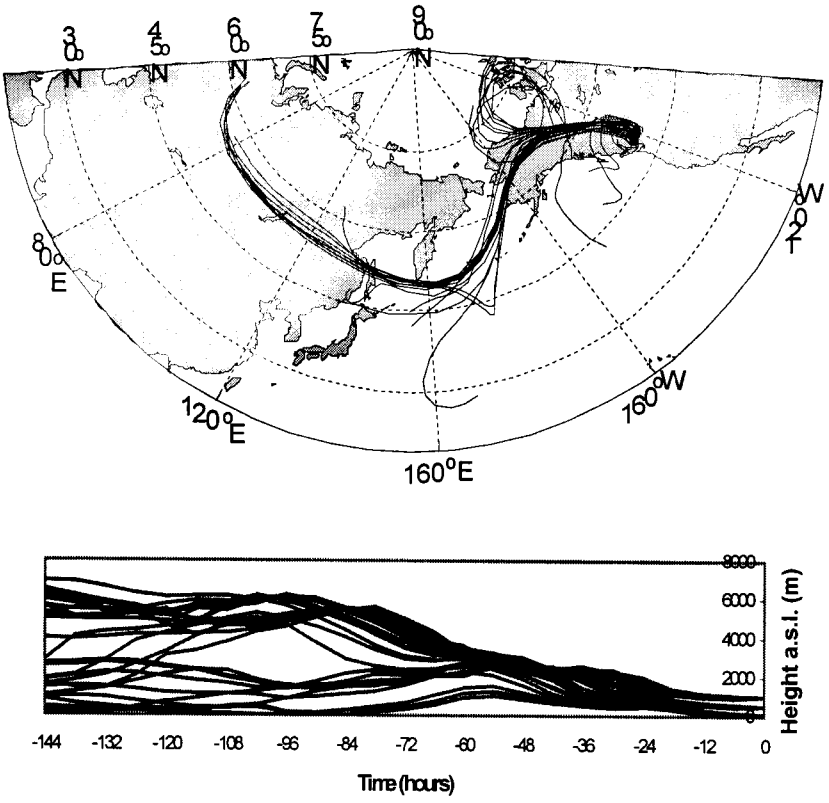

Figure 26 – Three dimensional back trajectories arriving over the LFV area on 31 October 1996 at 0600 UTC using the CANERM model. The three day back trajectory ensemble consists of 27 trajectories starting at 100m a.s.l., 500m a.s.l. and 1000m a.s.l. over the LFV. The lower plot shows the time height profile of the trajectories. Back trajectory data courtesy of Environment Canada's Canadian Meteorological Center.

concentrations remained elevated and daily ^{7}Be activity concentrations exceeded 6000 μBqm^{-3}.

Even though neither of the two major trajectory paths originated in the stratosphere, it is still probable that these trajectories passed through high ozone concentration regions prior to their arrival in the LFV. It has long been known that cutoff low pressure systems and troughs are responsible for the descent of ozone rich stratospheric air into the mid to upper troposphere via tropopause folding (Ancellet et al., 1993, Johnson and Viezee, 1981, Haagenson, 1981, Danielson et al., 1970, Schuepbach et al., 1998, Davies and Schuepbach, 1993). Therefore, air need only pass through these regions at mid to upper tropospheric levels to intercept ozone rich,

stratospheric air. This possible scenario is supported by the elevated ground level ozone and ^{7}Be concentrations at the surface in the LFV.

4.3.2 Case Study #2 – 20 December 1996 – 01 January 1997

4.3.2.1 Synoptic Overview

On 21 December 1996 at 0000 UTC, three main upper level features were present over the northeastern Pacific and North America. Over the north central Pacific, a high amplitude trough was present. The trough axis was oriented in a northwest - southeast direction. Immediately to the east of the trough, a narrow, high amplitude ridge extended as far north as the Arctic Ocean with its axis tilted in a north - south direction. The final feature was a broad trough encompassing the entire North American continent. These features were present at least up to the 250 mb isobaric surface.

Over the next 24 hours, the Pacific ridge and trough detached from the main flow creating a cutoff high and cutoff low respectively. Between 23 December at 0000 UTC and 24 December at 0000 UTC, the cutoff low moved eastward while the cutoff high, centered over northwestern Alaska remained stationary. This caused the cutoff high to become completely separated from the main flow (Figures 27 and 28). During this 24 hour period, the geopotential gradient of the large scale trough over North America increased and its axis shifted from the west coast of North America to the central United States.

Over the next 5 days, both the Pacific cutoff low and cutoff high joined and then re-detached from the main flow. The major consequence of this ridge/cutoff high system was that it acted as a barrier to the further eastward propagation of many surface low pressure systems that formed in the western and central Pacific Ocean. During this same time span, the northern portion of the North American trough

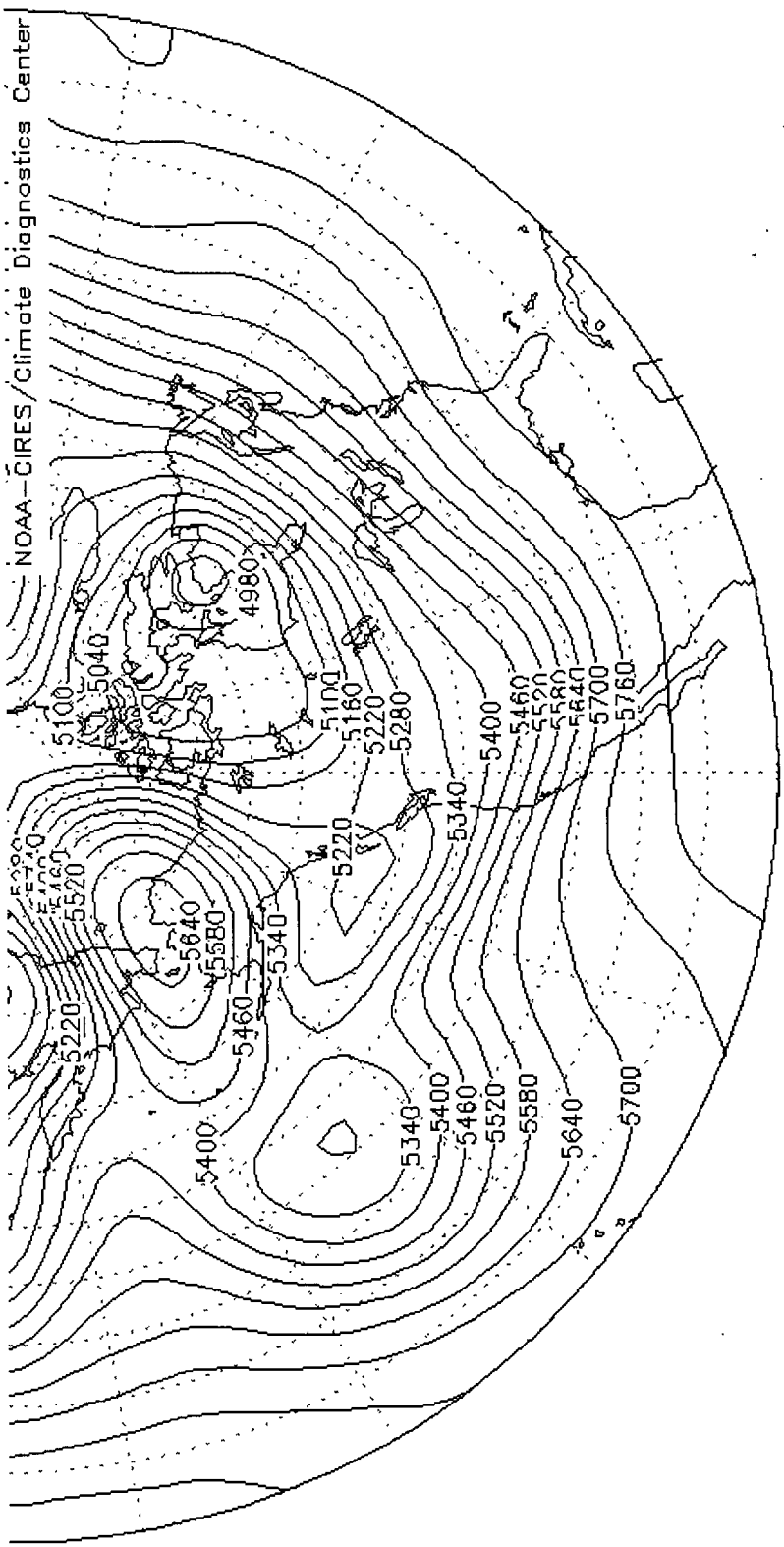

Figure 27 - 500 mb geopotential chart for 23 December 1996 at 0600 UTC. Image courtesy of the NOAA Climate Diagnostics Center.

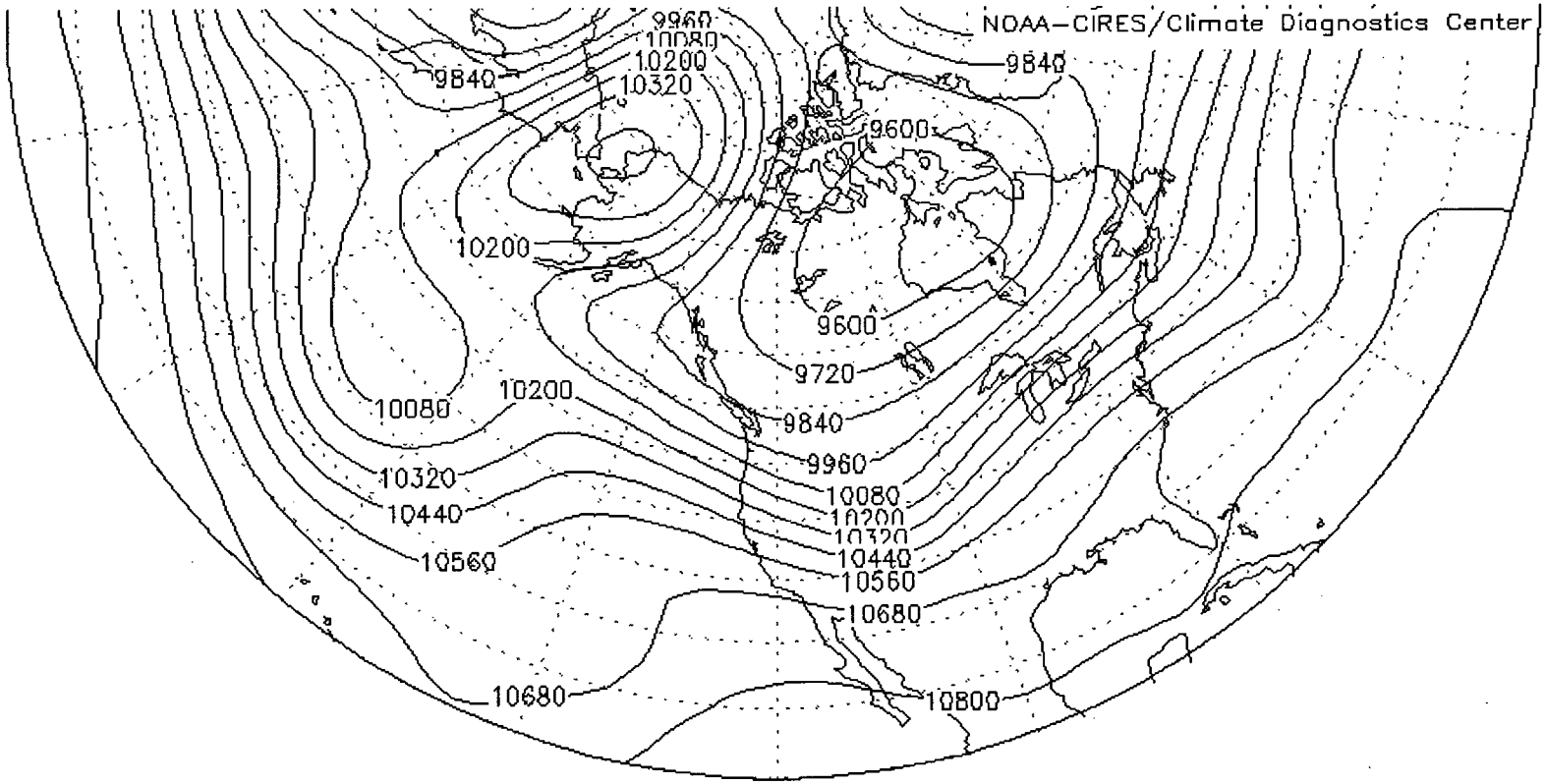

Figure 28 - 250 mb geopotential chart for 23 December 1996 at 0600 UTC. Image courtesy of the NOAA Climate Diagnostics Center.

separated from the main flow to create a cutoff low that covered most of Central Canada and the Northwest Territories.

At the surface, four major synoptic patterns were evident. These synoptic systems corresponded well with the upper level flow described above. Associated with the Pacific upper level trough on 21 December at 0000 UTC were three surface low pressure systems with the northern most system being the most intense with a central pressure 972 mb. Separating these low pressure systems from the west coast of North America was a strong high pressure system with a central pressure of 1048 mb over the northern Yukon Territory, Canada. Over North America, this high pressure system covered most of central Canada and separated two weak surface lows over the northern United States from an intense low over Labrador, Canada with a central pressure of 954 mb.

As the upper level ridge and trough began to separate from the main flow on 22 December at 0000 UTC, the North American high pressure system began to intensify and extend further south. Because of the strong pressure gradient on the western side of this high, the eastward progression of several surface low pressure systems over the northern Pacific was hindered. Over the next six days, these blocked low pressure systems combined to form one large surface low with several frontal systems (Figure 29).

Associated with the large upper level cutoff low that began to form over northern Canada on 24 December at 0000 UTC were several surface low pressure systems centered over an area just to the west of Baffin Island in the Northwest Territories. This area of low pressure was unable to progress further southwards due to the large area of high pressure over central Canada (Figure 29).

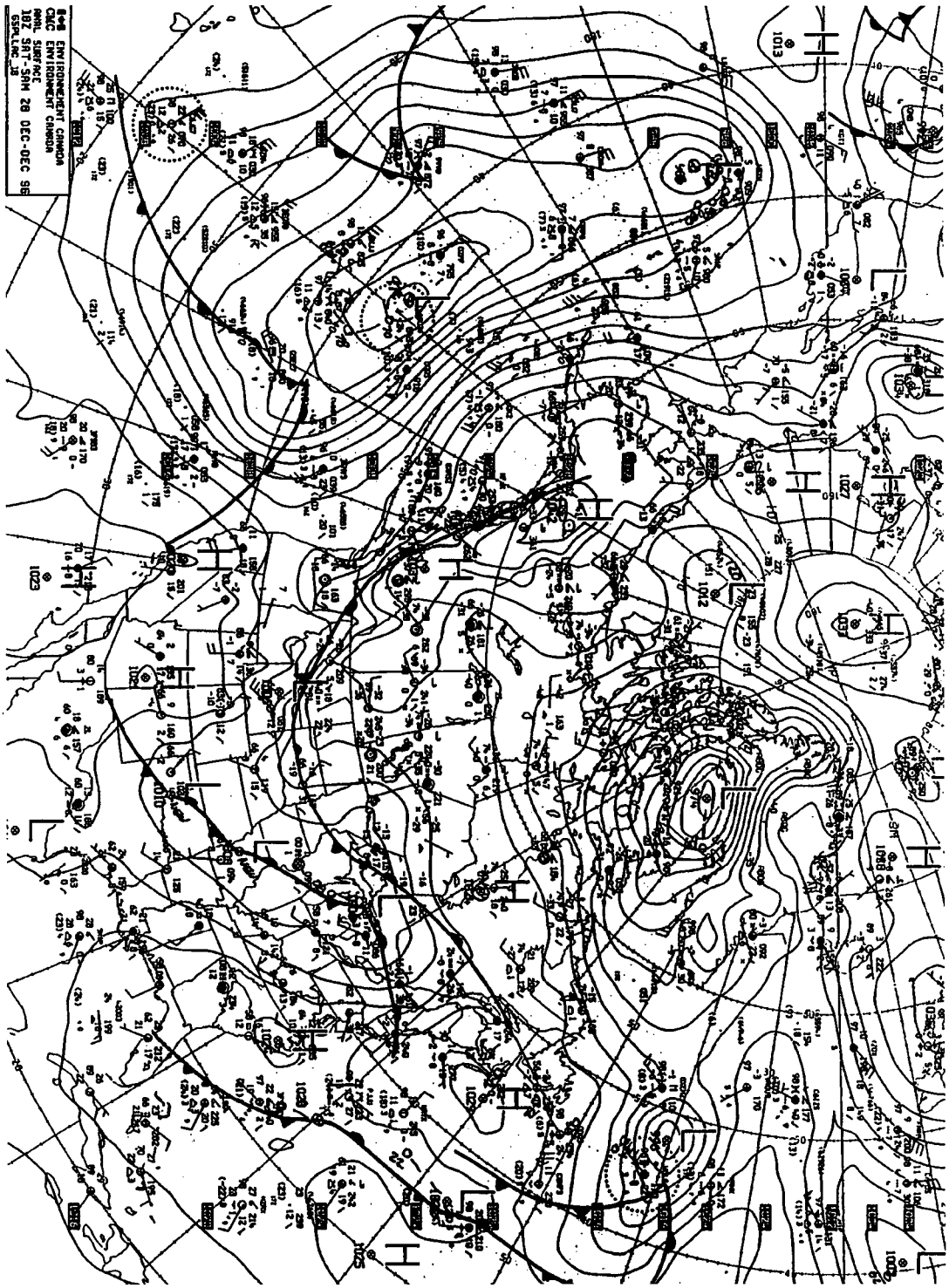
ENVIRONMENT CANADA
CMC ENVIRONMENT CANADA
ANAL SURFACE
18Z SAT-9AM 28 DEC-DEC 98
GSPALOC_18

Figure 29 – Surface isobaric chart for 28 December 1996 at 1800 UTC. Image courtesy of Environment Canada's Canadian Meteorological Center.

4.3.2.2 Surface O_3 and ^7Be Concentrations and Temperature in the LFV

On 21 December at 0600 UTC (20 December at 2200 PST), elevated ground level ozone concentrations began to be measured in the LFV. Unlike Case #1 described above (Section 4.3.1.2), these elevated concentrations occurred simultaneously at all four rural air quality monitoring stations (Figure 16b). By 21 December at 1200 UTC (0400 PST), the ozone concentrations at the rural stations rose to 25-30 ppb. These ozone concentrations rose to 30-35 ppb over the next seven days with very little scavenging by NO_x during the night time hours. After 29 October at 2200 UTC (1600 PST), the ground level ozone concentrations began to decrease until 31 December at 0600 UTC (30 December at 2200 PST) when concentrations began to sharply increase again with concentrations rising to 40-45 ppb. These concentrations did not remain as constant as the concentrations measured over the prior 10 days.

The urban air quality monitoring stations experienced ground level ozone concentrations with more variability at a diurnal scale especially at Kitsilano and Downtown Vancouver (Figure 16b). During the night time hours however, elevated ozone concentrations were measured at both the Richmond South and Port Coquitlam North air quality stations with concentrations reaching 30 ppb.

During the episode, the ADM ozone concentration remained fairly constant at about 20 ppb (Figure 15b). The only exceptions occurred when the ADM ozone concentration dipped to 16 ppb on 24 December and then rose to 27 ppb on 25 December. The CV of ozone also remained fairly constant during the episode (0.4 ppb) except between 24 December – 26 December (Figure 15b). During this time, the

CV rose to 0.6 ppb on 24 December and then fell to 0.2 ppb on the 25 December which corresponded with the relative maximum in ADM ozone.

As in Case #1, the daily ^{7}Be activity concentrations remained above 6000 μBqm^{-3} for two days only even though the ground level ozone concentrations remained elevated for several days (Figure 15b). Precipitation may have been responsible for the low activity concentrations measured at the beginning of the episode. On 20-21 December, the daily total precipitation at Vancouver International Airport was 7.9 mm and 8.5 mm respectively. Ishikawa *et al.* (1995) showed that even light precipitation events could washout a large amount of ^{7}Be.

The ADM temperature fluctuated between a low of -5°C on 23 December to a high of 6°C on 29 December. The relative minimum in ADM temperature that occurred between 21 December – 26 December could have been due to a cold/stationary front present over the area at this time.

4.3.2.3 Back Trajectory Analysis

When the daily ^{7}Be activity concentration exceeded 6000 μBqm^{-3} on 26-27 December, back trajectory analysis revealed three major trajectory paths that air particles followed prior to their arrival over the Lower Fraser Valley (Figure 30). The first trajectory path originated in the Pacific trough at levels just below the tropopause. Insufficient data was available to conclude whether this air originated in a tropopause fold associated with the upper level trough or if the air had just passed through an upper tropospheric region in which stratospherically intruded air was present. These trajectories originated from a maximum altitude of 7200 m before descending into the mid troposphere as the air traveled around the ridge and then to the lower troposphere as the air traveled through the broad region of surface high pressure that was located over British Columbia (Figure 29).

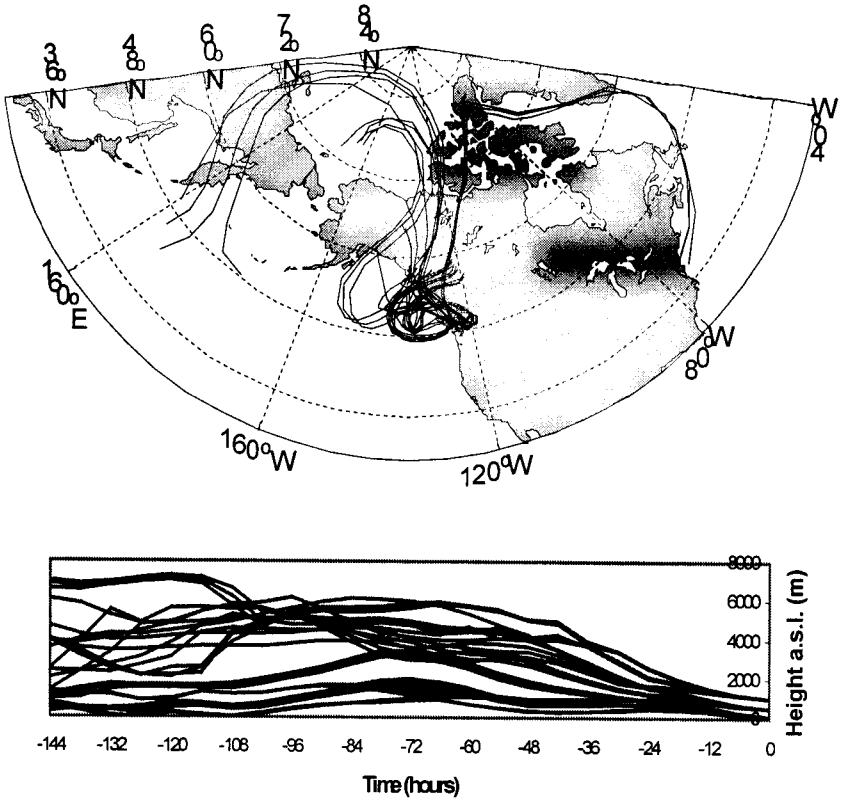

Figure 30 – Three dimensional back trajectories arriving over the LFV area on 26 December 1996 at 1200 UTC using the CANERM model. The three day back trajectory ensemble consists of 27 trajectories starting at 100m a.s.l., 500m a.s.l. and 1000m a.s.l. over the LFV. The lower plot shows the time height profile of the trajectories. Back trajectory data courtesy of Environment Canada's Canadian Meteorological Center.

The next trajectory path originated in the lower troposphere over the eastern United States. This air then traveled up the eastern seaboard of Canada where it ascended into the cutoff low situated over northern Canada on 21 October at 1800 UTC. The air then rapidly descended into the lower troposphere at an average rate of 2.3 cms^{-1} as it exited the cutoff low on 24 December at 0000 UTC and encountered the area of strong surface high pressure over northern Canada.

The final trajectory path originated in the lower troposphere and circulated around a surface low pressure system off the coast of southern British Columbia. The bulk of the trajectories, whose end points originated between 100 m a.s.l. and 500 m a.s.l. over the LFV region, followed this trajectory (Figure 30).

It is entirely possible that the trajectories that originated over eastern North America could have contained ozone from two completely different sources: the stratosphere and the boundary layer. The end of the back trajectory paths originated in the free troposphere at heights between 1500-2500 m. This air could have contained photochemically derived ozone produced over the highly urbanized American east coast. As this air ascended into the northern Canadian cutoff low, it may have encountered ozone rich air that descended from the stratosphere. Stohl and Trickl (1999), using detailed back trajectory analysis, studied a similar situation that occurred in the Swiss Alps when air arriving at the Jungfraujoch observatory contained ozone that originated within the boundary layer over the eastern United States and a tropopause fold that occurred over Greenland.

4.3.3 Case Study #3 – 22 January 1997 – 29 January 1997

4.3.3.1 Synoptic Overview

On 18 January at 0000 UTC, three large troughs were present over the northern Pacific Ocean and North America. The first trough, centered over the Russian Kamchatka Peninsula, covered the entire western half of the Pacific. Its trough axis was orientated in an approximately north - south direction. Over the next 24 hours, the northern section of the trough axis shifted to a northwest - southeast orientation. At the same time, this section of the trough also began to separate from the main flow forming a cutoff low (Figure 31). Between 19 January at 0000 UTC and 22 January at 1200 UTC, the southern portion of this trough began to dig southeastwards and formed another cutoff low centered about 3000 km north of Hawaii. These two cutoff lows intensified before rejoining the main flow 72 hours later. Separating this western Pacific trough/cutoff low system was a ridge that began to extend northwards

over the Bering Straight on 18 January at 0000 UTC before forming a cutoff high on 25 January at 0600 UTC.

The second trough present over the eastern portion of the north Pacific, on 18 January at 0000 UTC with an approximately north - south oriented trough axis, was short lived (Figure 31). Over the next 48 hours, the wavelength of this trough began to decrease as it propagated eastward so that its axis was now situated near the west coast of North America. Between 20 January at 0000 UTC and 23 January at 0000 UTC, the trough began to weaken and finally dissipate as it crossed the western North American coast.

The third very broad trough existed over the eastern half of North American continent for the duration of this episode (Figure 31). In the northern part of the trough, a cutoff low, with a large geopotential gradient, was present over central Quebec, Canada. Over the next five days, this cutoff low began to propagate northwestwards and weaken with its new position centered over Baffin Island in northern Canada. Between 21 January at 0600 UTC and 24 January at 1800 UTC, the southern part of the trough began to move westwards with its axis now centered over central North America. At the same time, the trough began to dig so that it extended as far south as the central portion of the Gulf of Mexico. All three of these troughs were present at least up to the 250 mb isobaric surface.

At the surface, there were up to five low pressure systems occurring simultaneously associated with the upper level trough present over the Western Pacific (Figure 32). Because of the surface high pressure system, associated with the central Pacific upper level ridge (Figure 31), centered over the northeastern Pacific Ocean, these lows were not able to propagate further east. As this high pinched off from a much larger region of high pressure over the tropics on 21 January at 0000

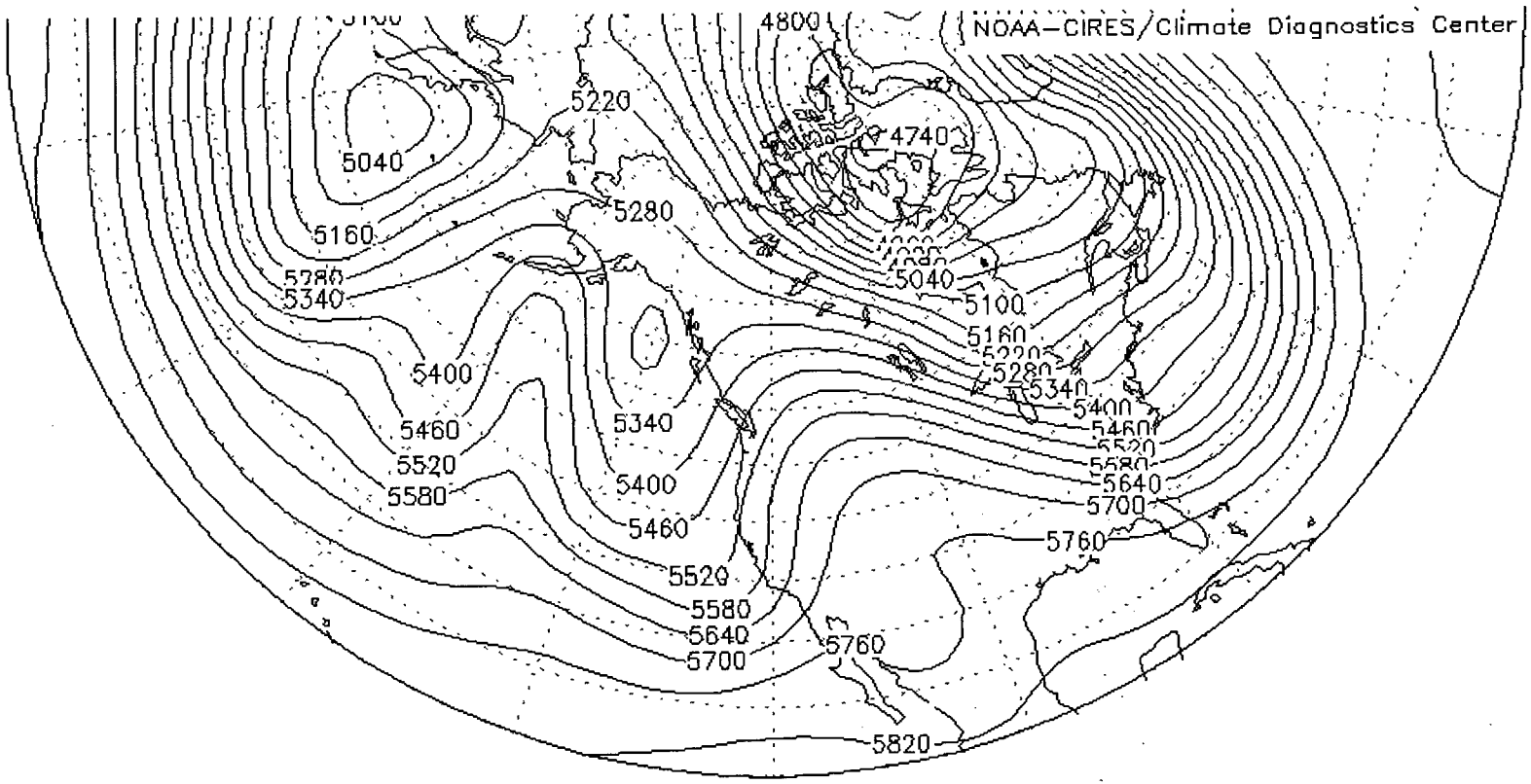

Figure 31 - 500 mb geopotential chart for 20 January 1997 at 0600 UTC. Image courtesy of the NOAA Climate Diagnostics Center.

UTC, the west Pacific low pressure systems were able to move eastwards around the southern portion of this "pinched off" high. These lows then encountered another region of high pressure centered over central Canada, blocking their further eastward progression. This was due to the strong pressure gradient associated with the outer region of this high (Figure 33). These lows eventually dissipated on 24 January. As these lows tracked around the southern end of the "pinched off" high pressure system and began to propagate and dissipate over the southeast portion of the northern Pacific and the southwestern United States, a new, more intense set of surface lows began to form in the north central Pacific. The movement of these lows was also restricted due to the strong surface high pressure system present over northwestern Canada.

The low pressure systems associated with the short lived trough present over the northeastern Pacific began to weaken between 18 January at 0000 UTC and 19 January at 0000 UTC. These lows eventually dissipated completely on 25 January at 0000 UTC.

The final set of low pressure systems were associated with the cutoff low present over northeastern Canada. Starting on 21 January at 0000 UTC, two new low pressure systems began to form over south central Canada. Over the next three days, these lows tracked eastwards over the Great Lakes, before turning north and joining the set of low pressure systems associated with the cutoff low over northeastern Canada.

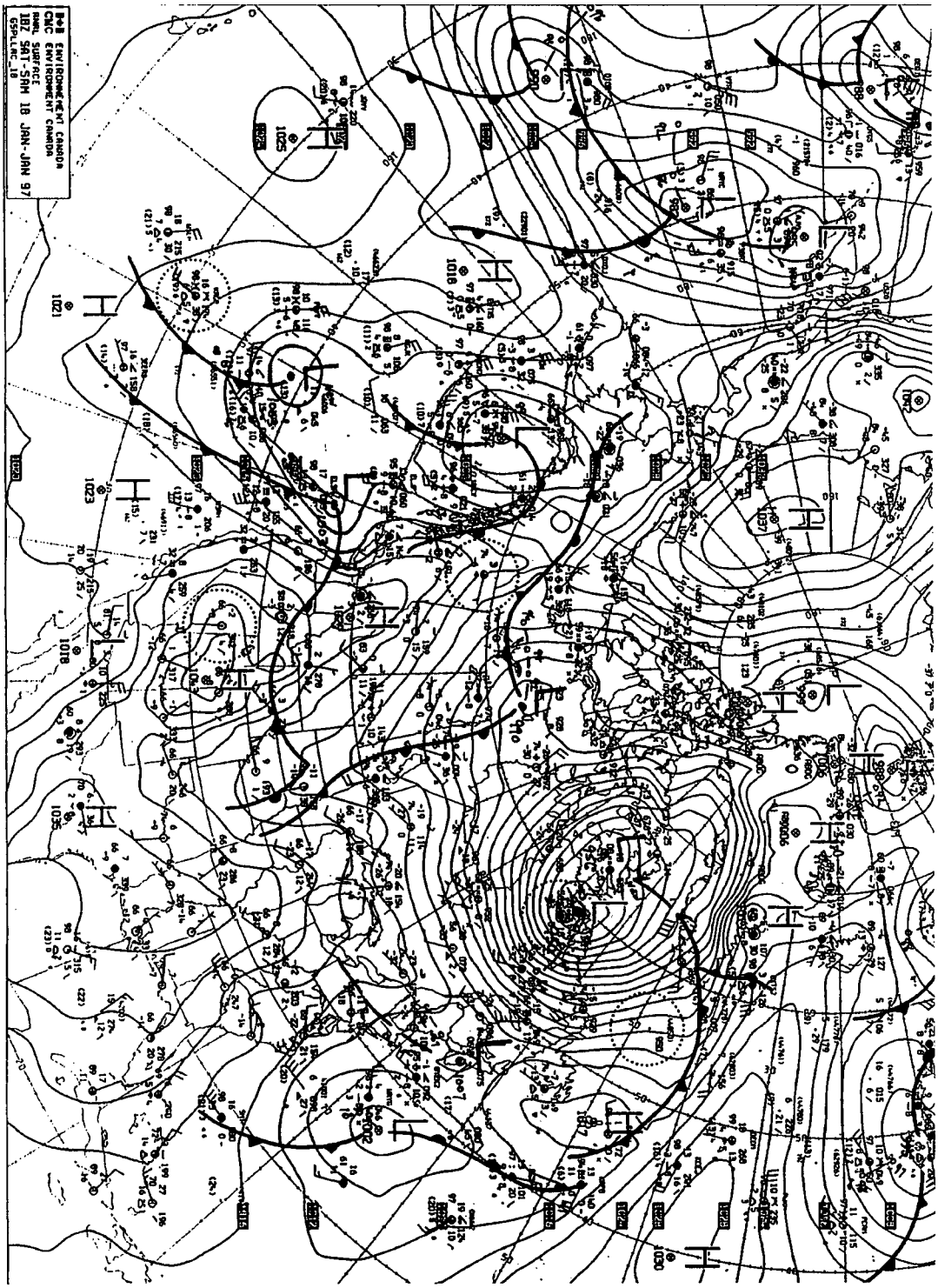
ENVIRONMENT CANADA
CMC ENVIRONMENT CANADA
MSL SURFACE
IBZ 00Z-SAM 18 JAN-JAN 97
GSPLLRC_18

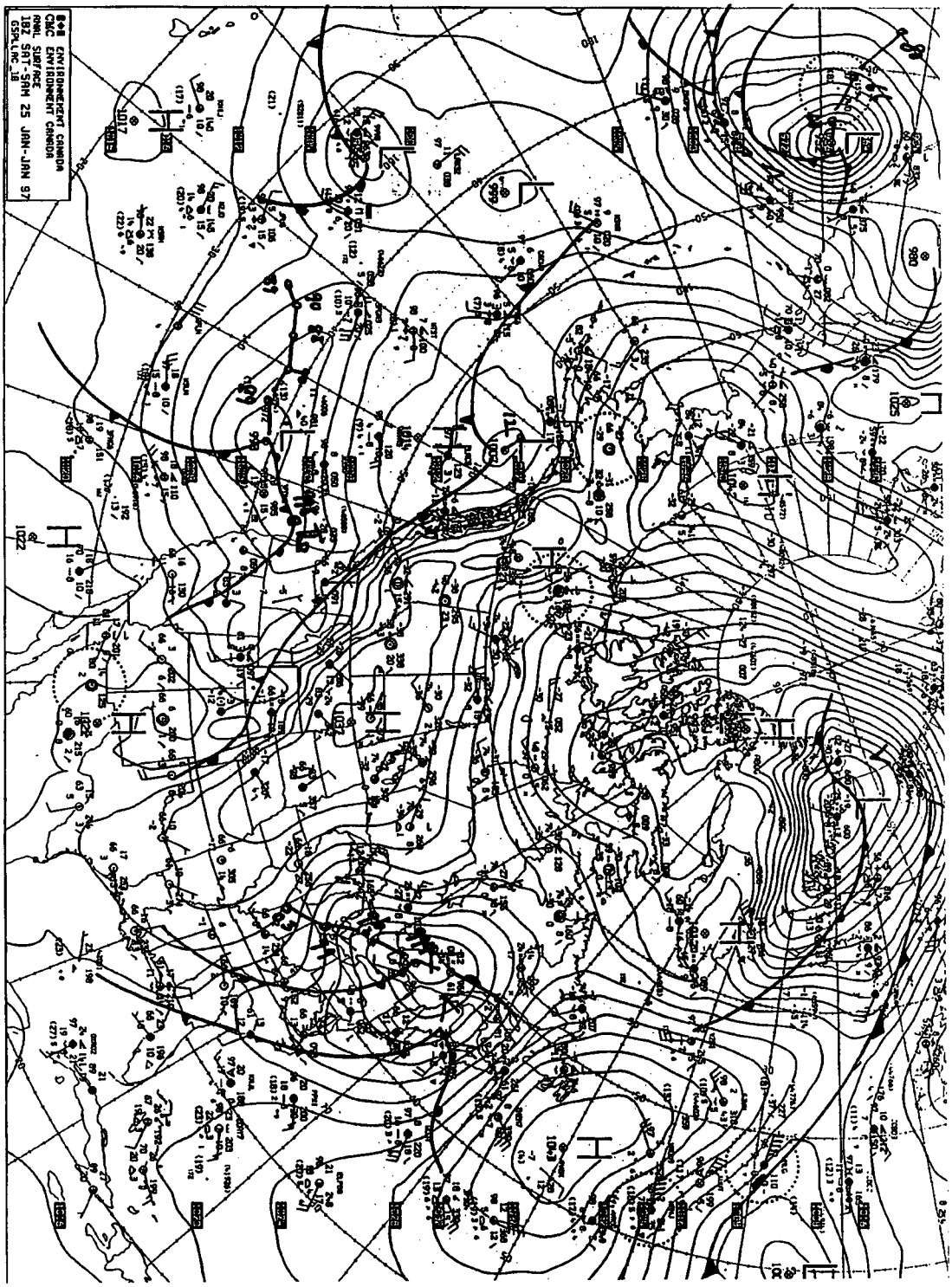
ENVIRONNEMENT CANADA
CMC ENVIRONMENT CANADA
RAWL SURFACE
18Z SAT-SAN 25 JAN-JAN 97
GSPLMC_18

Figure 32 (page 77) – Surface isobaric chart for 18 January 1997 at 1800 UTC. Image courtesy of Environment Canada's Canadian Meteorological Center.

Figure 33 (previous page) – Surface isobaric chart for 25 January 1997 at 1800 UTC. Image courtesy of Environment Canada's Canadian Meteorological Center.

4.3.3.2 Surface O_3 and ^7Be Concentrations and Temperature in the LFV

Between 22 January at 1200 UTC (0400 PST) and 23 January at 0000 UTC (22 January at 1600 PST), elevated ozone concentrations began to be measured at the rural air quality monitoring stations in the LFV (Figure 16c). With the exception of the Hope Airport air quality station, the ozone concentrations exhibited a diurnal pattern between 23 January at 0000 UTC (22 January at 1600 PST) and 25 January at 0800 UTC (0000 PST). Briefly, a normal diurnal pattern of ozone exhibits a morning low in concentration rising to maximum levels in the early afternoon and then decreasing to low nocturnal concentrations around mid-late evening (Figure 12). For the next 72 hours, the elevated ozone concentrations remained constant between 20-30 ppb with no NO_x scavenging during the night time hours (with the exception of the Surrey East station). After 28 January at 0800 UTC (0000 PST), the ozone concentrations began to decrease and exhibit a more diurnal pattern.

At the beginning of the episode, urban ozone concentrations rose sharply in the Kitsilano and Richmond air quality stations from near zero levels to between 15-30 ppb. The Port Coquitlam North and Downtown Vancouver stations did not exhibit a similar increase until two days later (Figure 16c). At about the same time in which the rural ozone concentrations switched to a constant ozone concentration pattern from a diurnal pattern, the urban ozone concentrations sharply fell to near zero values on 25 January at 0000 UTC (24 January at 1600 PST). With the exception of the night time hours on 26 January and 27 January, the ozone concentrations exhibited a

roughly diurnal pattern between 25 January at 0000 UTC (24 January at 1600 PST) and the end of the episode on 28 January.

During the episode, the ADM ozone concentration fluctuated between a maximum of 30 ppb on 23 January and a minimum of 17 ppb on 27 January (Figure 15c). The maximum ADM ozone concentration corresponded to the time at which the hourly ozone concentrations began to sharply increase in the urban and rural stations (Figure 16c). Strangely enough, the minimum ADM ozone concentration corresponded with the maximum daily ^{7}Be measurement taken at UBC. The CV of ozone reached a minimum of 0.15 ppb at the same time that the ADM ozone concentration reached its maximum and vice versa for the minimum CV of ozone (Figure 15c).

Daily ^{7}Be activity concentrations measured at the beginning of the episode (Figure 15c) were low even though ground level ozone concentrations were elevated at this time. Precipitation may have been responsible for these low activity concentrations as total daily accumulations of between 1.5-30 mm were measured at Vancouver International Airport between 16-22 January.

The ADM temperature decreased from 7°C on 22 January to a minimum of -2.9°C on 25 January. Cold easterly outflow winds from the continent behind a stationary front located over the Lower Fraser Valley area may have been responsible for the cold temperatures that occurred on 25 January. ADM temperatures increased to approximately 4°C by the end of the episode on 28 January.

4.3.3.3 Back Trajectory Analysis

Back trajectory analysis revealed that the initial elevated ozone concentrations measured in the LFV may have been the result of two sources. The first source originated either within or just above the boundary layer over the west coast of the United States (Figure 34). As the air associated with this trajectory path traveled up

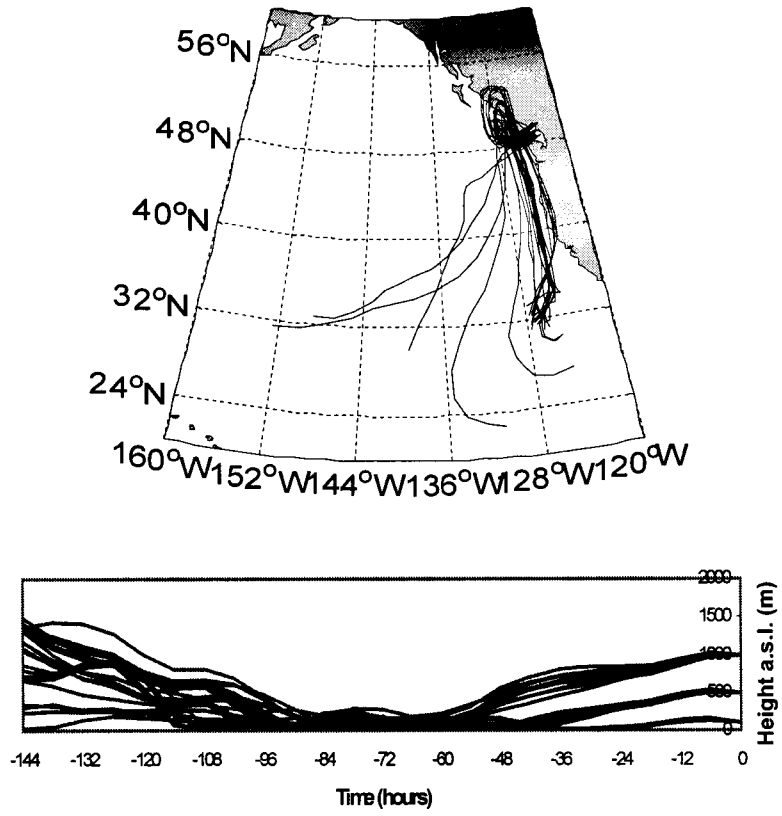

Figure 34 – Three dimensional back trajectories arriving over the LFV area on 23 January 1997 at 0000 UTC using the CANERM model. The three day back trajectory ensemble consists of 27 trajectories starting at 100m a.s.l., 500m a.s.l. and 1000m a.s.l. over the LFV. The lower plot shows the time height profile of the trajectories. Back trajectory data courtesy of Environment Canada's Canadian Meteorological Center.

the coast, it may have encountered polluted boundary layer air from many large urban costal centers including San Diego, Los Angeles, San Francisco, Portland and Seattle. The second trajectory path originated at mid tropospheric levels within a cutoff low centered just to the south of Alaska (Figure 35).

Starting on 24 January at 1800 UTC, the bulk of the trajectories originated at mid tropospheric to lower stratospheric levels in the Arctic region between northern Alaska and north central Siberia (Figure 36). The trajectories that descended from the highest altitudes originated on the eastern side of a trough located over central Siberia six days earlier. The remaining high altitude trajectories originated from a shortwave trough that formed over northeastern Russia on 20 January at 0600 UTC. On 23

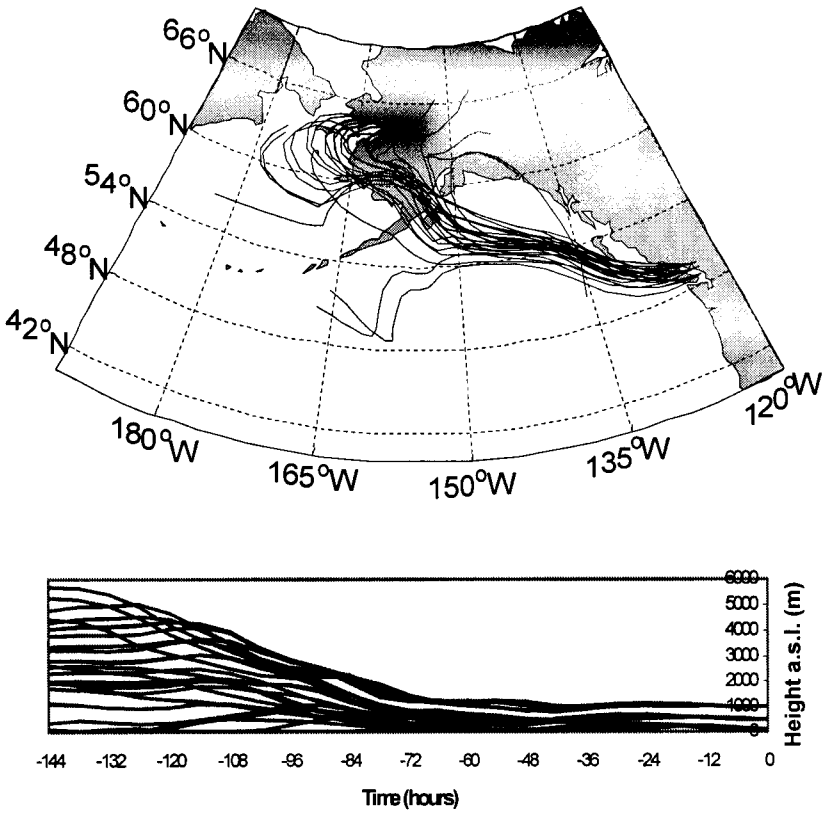

Figure 35 – Three dimensional back trajectories arriving over the LFV area on 23 January 1997 at 1800 UTC using the CANERM model. The three day back trajectory ensemble consists of 27 trajectories starting at 100m a.s.l., 500m a.s.l. and 1000m a.s.l. over the LFV. The lower plot shows the time height profile of the trajectories. Back trajectory data courtesy of Environment Canada's Canadian Meteorological Center.

January at 0000 UTC, the bulk of the high altitude trajectories began to descend into the mid to lower troposphere at an average rate of 1.2-2.2 cms^{-1}. This descent was probably caused by the large region of high pressure that was present over western Canada and Alaska.

Since the tropopause can exist at heights as low as 8000 m above sea level in the polar regions (Stull, 2000), it is entirely possible that the trajectories that originated at around 8000 m in the Siberian trough could have originated in the stratosphere. Similar to Case #1, it is possible that two sources of stratospheric air, both from the Siberian trough and the shortwave located over northeastern Russia, contributed to the

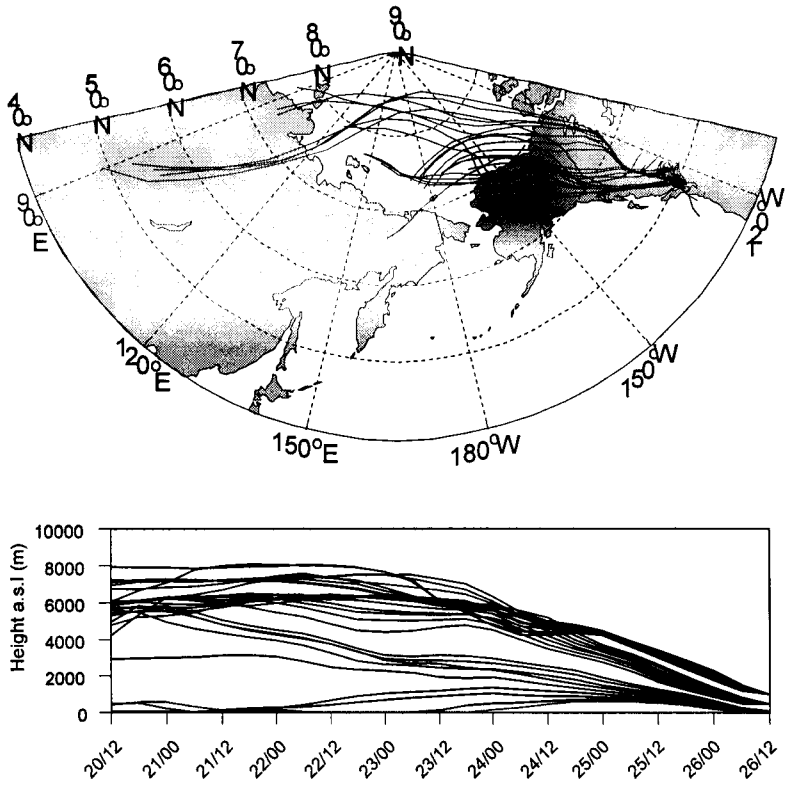

Figure 36 – Three dimensional back trajectories arriving over the LFV area on 26 January 1997 at 1200 UTC using the CANERM model. The three day back trajectory ensemble consists of 27 trajectories starting at 100m a.s.l., 500m a.s.l. and 1000m a.s.l. over the LFV. The lower plot shows the time height profile of the trajectories. Back trajectory data courtesy of Environment Canada's Canadian Meteorological Center.

elevated ground level ozone concentrations in the LFV between 25 January at 0800 UTC and 28 January at 0800 UTC.

As in Case #2, the elevated ozone concentrations in the LFV at the beginning of the episode may have been both stratospheric (south Alaskan cutoff low) and lower tropospheric (boundary layer over the west coast of North America.) in origin (Figures 34 and 35).

4.3.4 Case Study #4 – 05 January 2001 – 11 January 2001

4.3.4.1 Synoptic Overview

On 1 January at 0000 UTC, two troughs were present over the northern Pacific Ocean. The westernmost trough was centered over Japan with an approximately

north - south oriented axis. The second trough covered the entire northeast Pacific, with its axis centered at about 155°W longitude with a north - south orientation. Separating these two troughs was a ridge that extended as far north as northeastern Russia (Figure 37).

The upper air pattern over North America consisted of a ridge extending as far east as Western Ontario, Canada with its axis oriented in a northeast - southwest direction. To the east of this ridge was a trough that extended as far east as Saint John's, Canada with is axis centered over Texas, USA to the south and the Great Lakes to the north (Figure 37).

Over the next 48 hours, the ridge situated over the central Pacific began to separate from the main flow allowing a cutoff high to form on 3 January at 0000 UTC. This cutoff high began to propagate in a northwesterly direction until it rejoined the flow over north central Siberia on 6 January at 0000 UTC.

As the central Pacific ridge began to separate from the main flow, the two Pacific troughs combined to form one large trough that covered the entire north Pacific on 2 January at 1200 UTC. Extending over the entire trough was a jet streak situated at 250 mb in which wind speeds exceeded 150 knots (Figure 38). Over the next six days, a number of shortwave troughs propagated around this Pacific trough, the largest of which occurred on 7 January at 1200 UTC (Figure 39). Between 31 December and 8 January, the North American ridge to the west and trough to the east persisted at various degrees of intensity.

Over the course of the entire episode, the synoptic features corresponded well with the upper air flow. Associated with the western Pacific trough was an intense surface low pressure system centered approximately 800 km east of central Japan with a

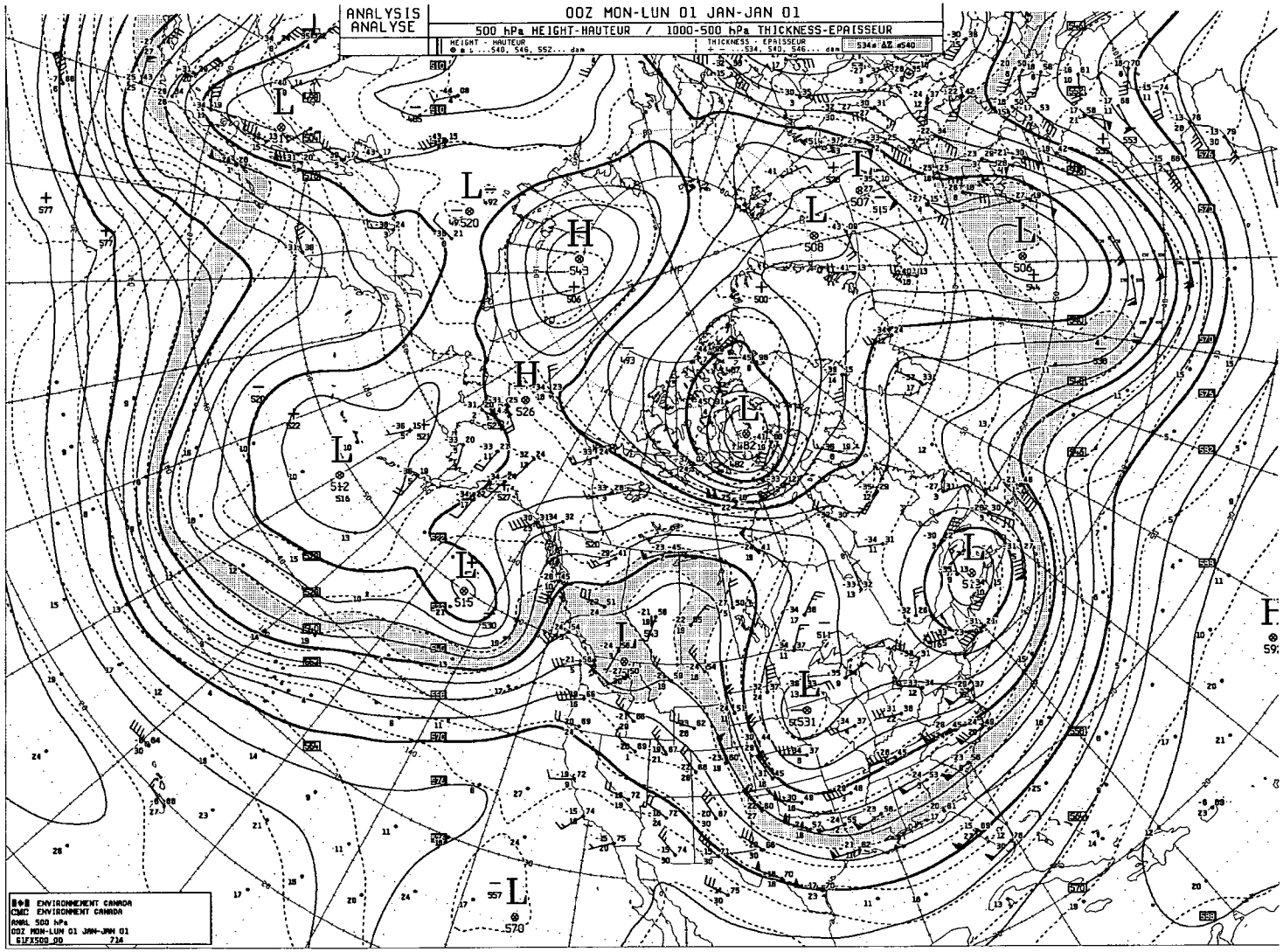
ANALYSIS
ANALYSE
00Z MON-LUN 01 JAN-JAN 01
500 hPa HEIGHT-HAUTEUR / 1000-500 hPa THICKNESS-EPAISSEUR
HEIGHT - HAUTEUR
THICKNESS - EPAISSEUR
ENVIRONNEMENT CANADA
CMC ENVIRONNEMENT CANADA
ANAL 500 hPa
00Z MON-LUN 01 JAN-JAN 01

Figure 37 (previous page) - 500 mb geopotential chart for 1 January 2001 at 0000 UTC. Image courtesy of Environment Canada's Canadian Meteorological Center.

central pressure of 965 mb on 1 January at 0000 UTC (Figure 40). Over the next 24 hours, this surface low tracked northward towards the Kamchatka Peninsula and deepened to 950 mb.

To the east of this low was a large region of high pressure located over the central Pacific (Figure 40). As the corresponding ridge began to separate from the main flow on 1 January at 1200 UTC, this surface high pressure system retreated to the southeast allowing the low pressure systems in the east and west Pacific to join and form a region of surface low pressure covering the entire north Pacific.

The northeastern Pacific was dominated by five surface low pressure systems with central pressures ranging form 979 mb-1000 mb. Most of these low pressure systems were unable to make landfall over the west coast due a large region of high pressure covering the western half of North America. These low pressure centers joined with the west Pacific surface lows as the central Pacific surface high retreated to the southeast (Figure 41). At any one time, the number of lows associated with this large Pacific surface low pressure region ranged from four to eight. As the region of high pressure over western North America began to weaken on 8 January at 1200 UTC, the easternmost low pressure centers made landfall over northwestern Canada where they rapidly dissipated.

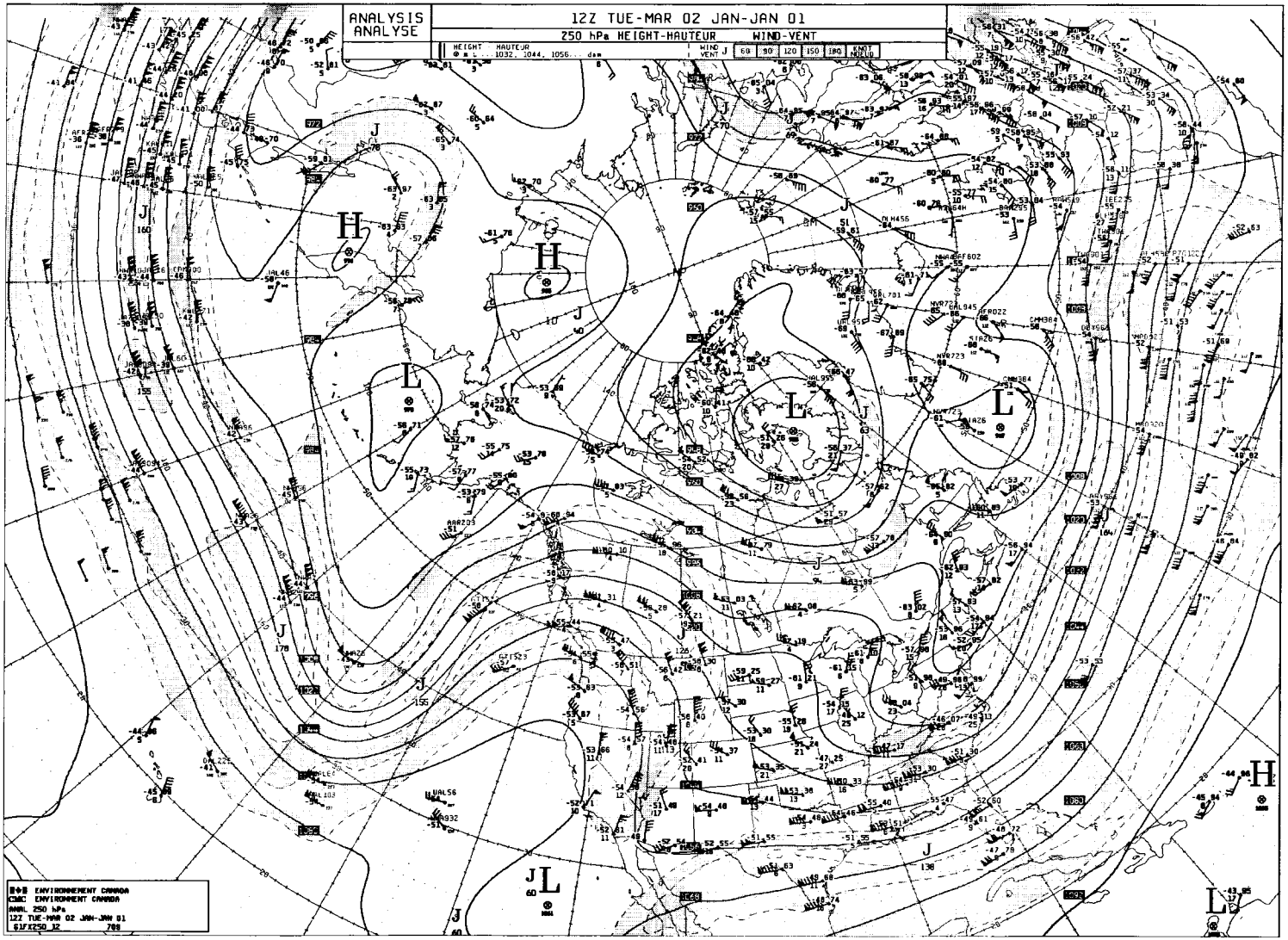
ANALYSIS
ANALYSE
12Z TUE-MAR 02 JAN-JAN 01
250 hPa HEIGHT-HAUTEUR WIND-VENT
HEIGHT HAUTEUR
1032, 1044, 1056 dam
WIND VENT J
60 90 120 150 180 KNOT NOEUD
ENVIRONMENT CANADA
CMC ENVIRONMENT CANADA
ANAL 250 hPa
12Z TUE-MAR 02 JAN-JAN 01
H
L
J

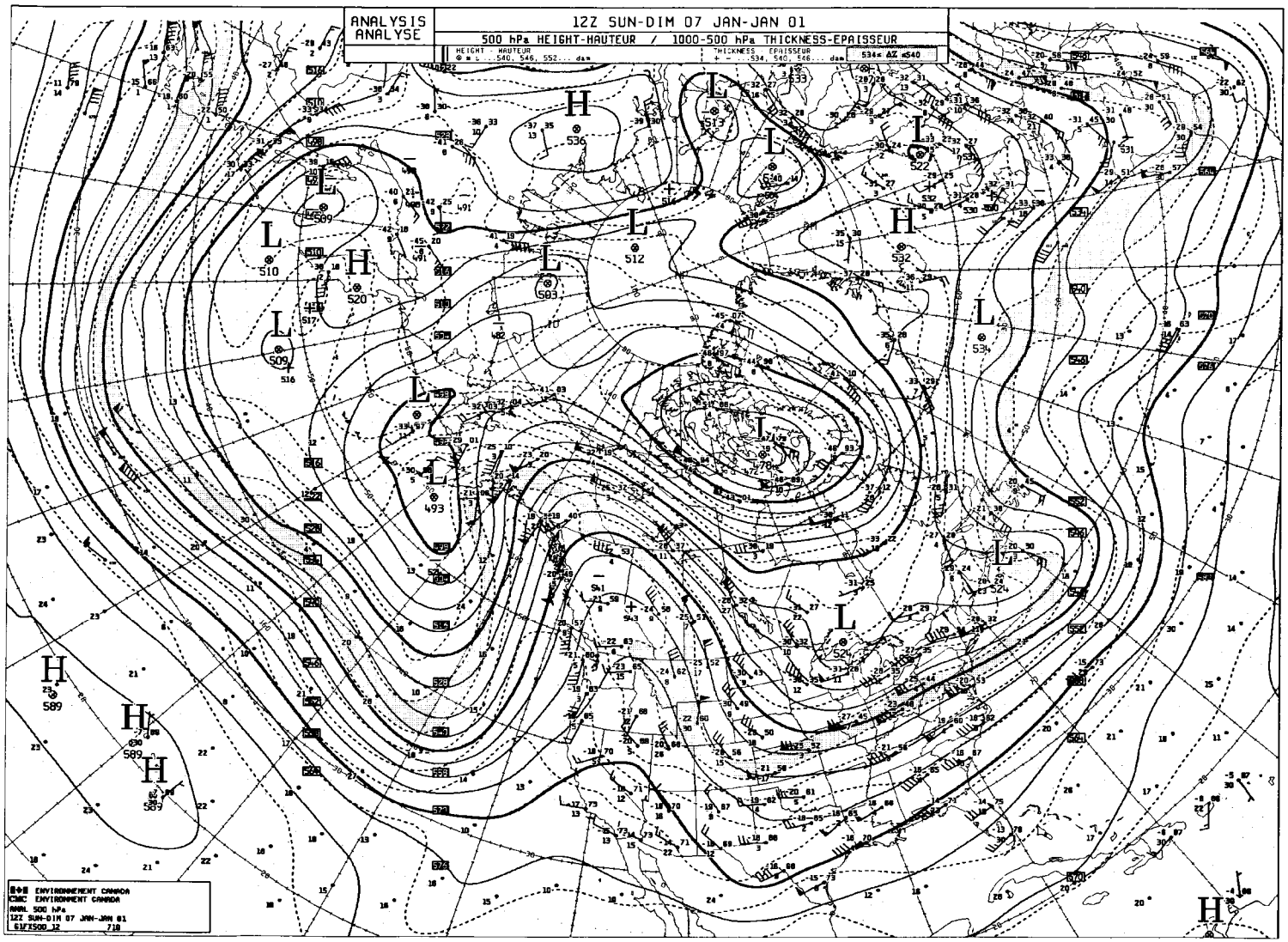
ANALYSIS
ANALYSE
12Z SUN-DIM 07 JAN-JAN 01
500 hPa HEIGHT-HAUTEUR / 1000-500 hPa THICKNESS-EPAISSEUR
HEIGHT - HAUTEUR
⊗ ⊕ : ...540, 546, 552... dam
THICKNESS - EPAISSEUR
+ - : ...534, 540, 546... dam
534= ΔZ =540
ENVIRONNEMENT CANADA
CMC ENVIRONMENT CANADA
ANAL 500 hPa
12Z SUN-DIM 07 JAN-JAN 01
61FX500_12 710

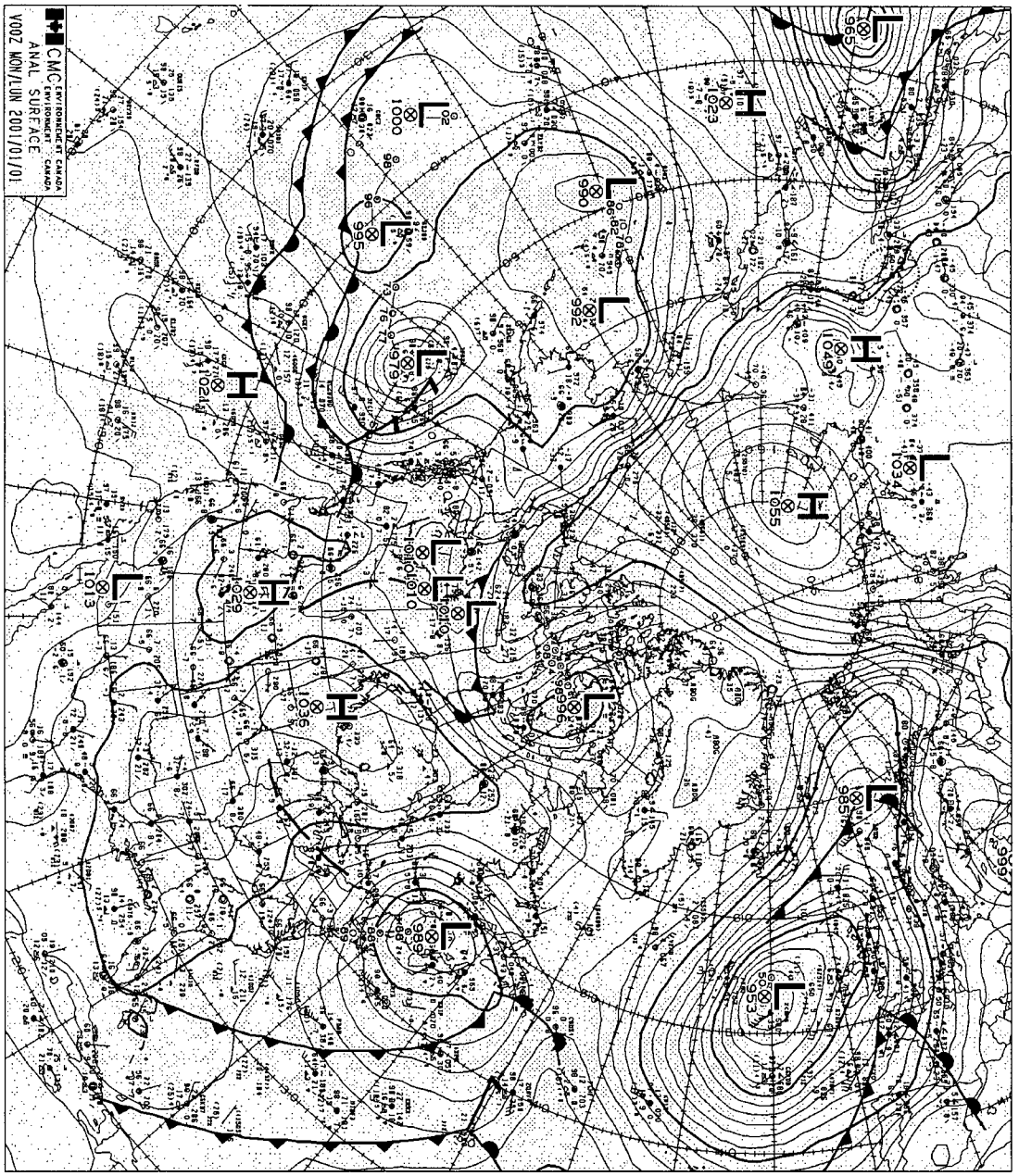
CMC ENVIRONNEMENT CANADA
ENVIRONMENT CANADA
ANAL SURFACE
00Z MON/LUN 2001/01/01

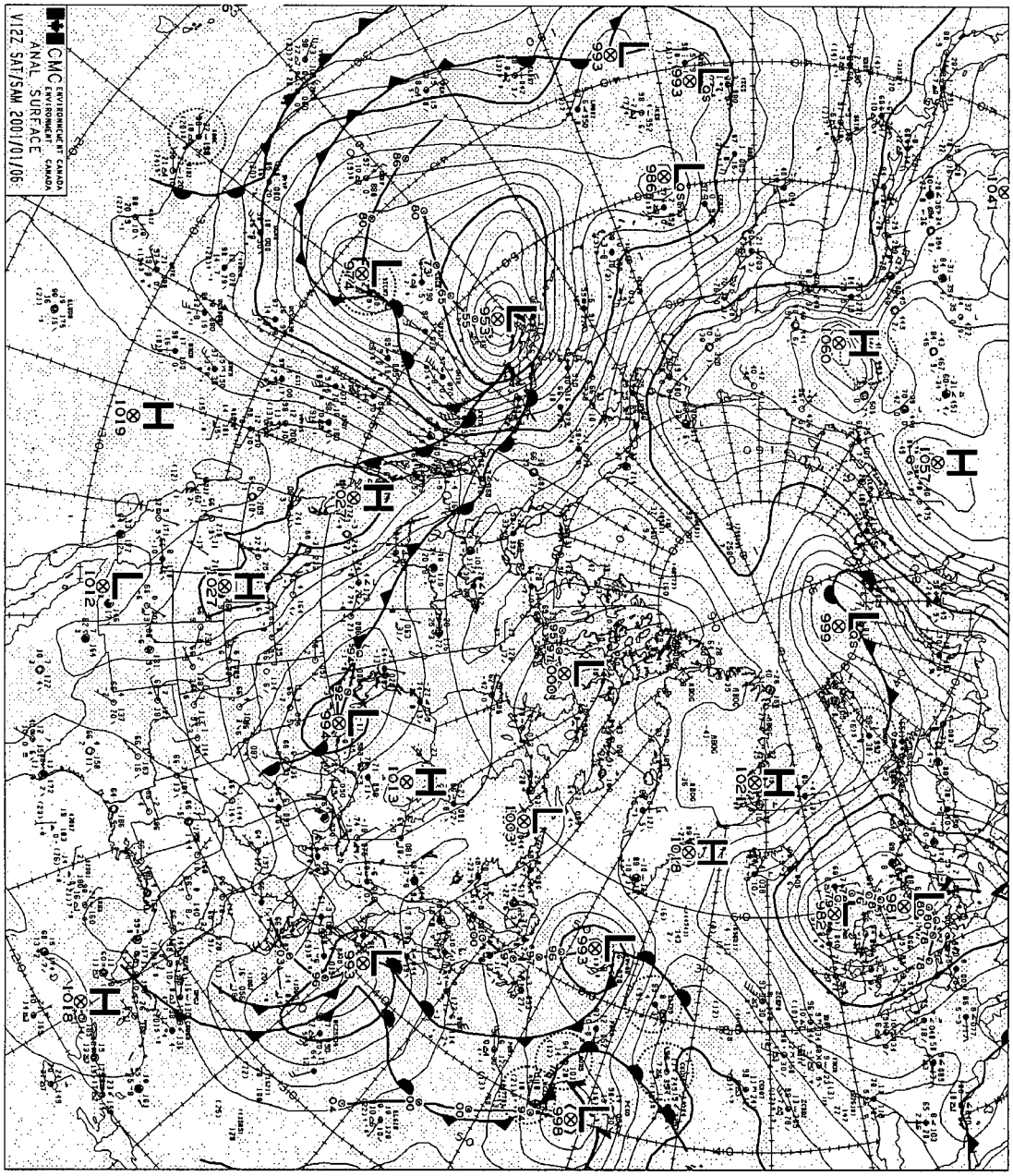
CMC ENVIRONMENT CANADA
ENVIRONNEMENT CANADA
ANAL SURFACE
V122 SAT/SAM 2001/01/06

Figure 38 (page 87) - 250 mb geopotential chart for 2 January 2001 at 1200 UTC. Image courtesy of Environment Canada's Canadian Meteorological Center.

Figure 39 (page 88) - 500 mb geopotential chart for 7 January 2001 at 1200 UTC. Image courtesy of Environment Canada's Canadian Meteorological Center.

Figure 40 (page 89) – Surface isobaric chart for 1 January 2001 at 0000 UTC. Image courtesy of Environment Canada's Canadian Meteorological Center.

Figure 41 (previous page) – Surface isobaric chart for 6 January 2001 at 1200 UTC. Image courtesy of Environment Canada's Canadian Meteorological Center.

4.3.4.2 Surface O_3 and ^7Be Concentrations and Temperature in the LFV

On 6 January between 0000-1000 UTC (5 January at 1600 PST to 6 January at 0200 PST), the rural ground level ozone concentrations exhibited a diurnal pattern at Chilliwack Airport, Langley Central and Surrey East air quality monitoring stations (Figure 16d). Hope Airport was the only station that experienced elevated ozone concentrations on the night of 6 January. After 6 January at 1000 UTC (0200 PST) until 8 January at 0400 UTC (7 January at 2000 PST), elevated ozone concentrations were measured at all of the rural air quality stations with the exception of Surrey East. These elevated ozone concentrations reached concentrations between 30-35 ppb. On 9 January at 0400 UTC (8 January at 2000 PST), the ground level ozone concentrations, with the exception of Langley Central decreased to near zero values before sharply increasing to 25-35 ppb on 9 January at 0600 UTC (8 January at 2200 PST). The ground level ozone concentrations remained elevated at the rural stations, with the exception of Hope Airport, for the rest of the episode.

In the urban areas, the Kitsilano and Richmond South air quality monitoring stations exhibited a diurnal pattern with concentrations reaching 20-25 ppb on 6 January. Downtown Vancouver experienced ground level ozone concentrations of only 5-10 ppb during this time (Figure 16d). For the rest of the episode, only Richmond South experienced elevated ozone concentrations with maximum values

ranging between 15-20 ppb. Downtown Vancouver and Kitsilano had no hourly ground level ozone concentrations greater than 5 ppb during this time.

During the episode, the ADM ozone concentration experienced two relative maxima and one relative minimum (Figure 15d). The first relative ADM ozone concentration maximum occurred on 5 January (33 ppb) and the second occurred on 9 January (29 ppb). The minimum occurred on 7 January (14 ppb). Associated with the relative maxima of ADM ozone concentration, the CV of ozone experienced deep minima of 0.15 ppb on 5 January and 0.2 ppb on 9 January. Conversely, the CV of ozone reached a maximum of 0.9 ppb on 7 January, the same day that the ADM ozone concentration was at its minimum.

The shape of the daily ^{7}Be activity concentration time series for the episode was similar to that of Case #3, with low values at the beginning and end of the episode and a single spike at about 9000 μBqm^{-3} that occurred in the middle of the episode (8 January) (Figure 15d). Although no data was available at this time, any precipitation that might have occurred could explain the single sharp spike in the ^{7}Be time series for the episode (see sections 4.3.1.2, 4.3.2.2 and 4.3.3.2).

The ADM temperature remained fairly constant during the episode with temperatures ranging between 7-10°C.

4.3.4.3 Back Trajectory Analysis

Starting on 6 January at 1800 UTC, trajectories arriving at 1000 m a.s.l. over the LFV originated at altitudes of between 6700 - 7500 m in a trough centered about 500 km south of the Aleutian Islands six days earlier (Figure 42). On 1 January at 0600 UTC, these trajectories experienced a rapid descent of between 2.9-5.8 cms^{-1} for the next 24 hours. On January 2 at 0600 UTC, these trajectories began to ascend to 4500 m before descending into the LFV.

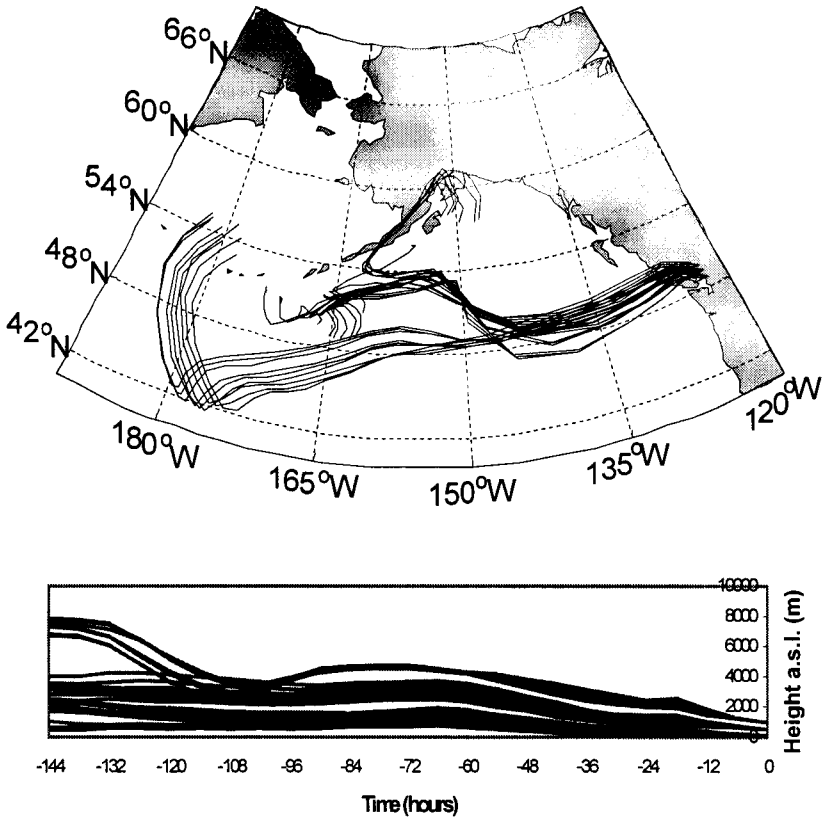

Figure 42 – Three dimensional back trajectories arriving over the LFV area on 6 January 2001 at 1800 UTC using the CANERM model. The three day back trajectory ensemble consists of 27 trajectories starting at 100m a.s.l., 500m a.s.l. and 1000m a.s.l. over the LFV. The lower plot shows the time height profile of the trajectories. Back trajectory data courtesy of Environment Canada's Canadian Meteorological Center.

Between 6 January at 1200 UTC and 8 January at 0600 UTC, at least one third of the trajectories arriving over the LFV originated from altitudes greater than 5000 m. The most notable example occurred on 7 January at 0600 UTC when all but five of the trajectories originated above 5000 m six days earlier (Figure 43). Trajectories arriving over the LFV at an altitude of 500 m a.s.l. originated at heights ranging from 7000 m-9000 m in the Aelutian Island trough six days earlier. Between 1 January at 0600 UTC and 2 January at 0000 UTC, these trajectories experienced a rate of descent of between 1.7-7.0 cms^{-1}. Trajectories arriving over the LFV at an altitude of 1000 m a.s.l. on 7 January at 0600 UTC originated as far west as central Siberia six days earlier. Over this six day period, the trajectories traveled around the large scale

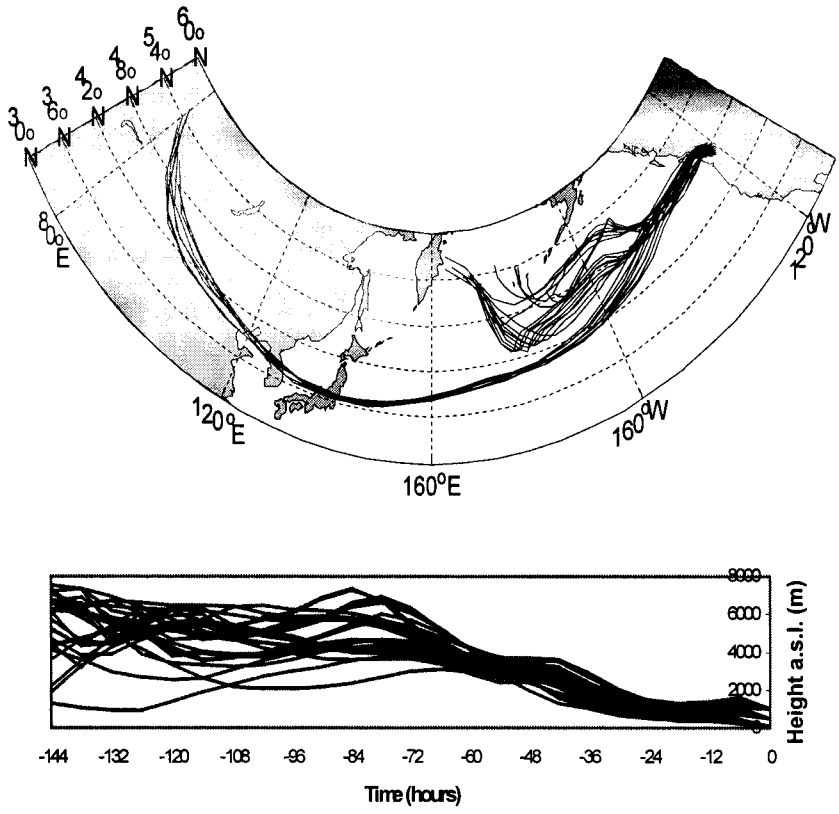

Figure 43 – Three dimensional back trajectories arriving over the LFV area on 7 January 2001 at 1800 UTC using the CANERM model. The three day back trajectory ensemble consists of 27 trajectories starting at 100m a.s.l., 500m a.s.l. and 1000m a.s.l. over the LFV. The lower plot shows the time height profile of the trajectories. Back trajectory data courtesy of Environment Canada's Canadian Meteorological Center.

Pacific trough at mid tropospheric levels between 1 January at 0600 UTC and 5 January 0000 UTC before descending into the LFV. The trajectories arriving over the LFV at 100 m a.s.l. originated in the Aleutian Island trough six days earlier at heights between 5000 m-6000 m.

Because several of the trajectories originated from altitudes between 8000m-9000 m above sea level, some of the air over the LFV may have originated in the lower stratosphere six days prior to their arrival in the LFV. There are two reasons why this could be so. First, the rapid descent experienced by some of the trajectories that arrived over the LFV on 6 January at 1800 UTC and 7 January at 0600 UTC may have been due to the air descending into the troposphere via a tropopause fold.

Second, the locations of suspected tropopause folds can be identified by thin, dark, elongated lines in water vapor satellite images (Appenzeller and Davies, 1992, Stohl *et al.*, 2000). These are possible areas of dry air descending from the stratosphere (Appenzeller and Davies, 1992). Figure 44 shows such a dry line that existed near the Alutian Island trough extending from the Kamchatka Peninsula to 30°N latitude 165°W longitude and then up to 40°N latitude 155°W longitude.

Figure 44 – GOES water vapor satellite image for 1 January 2001 at 0000 UTC. Dark regions denote large radiance values (low moisture content in the mid to upper troposphere). Image courtesy of Environment Canada's Canadian Meteorological Center.

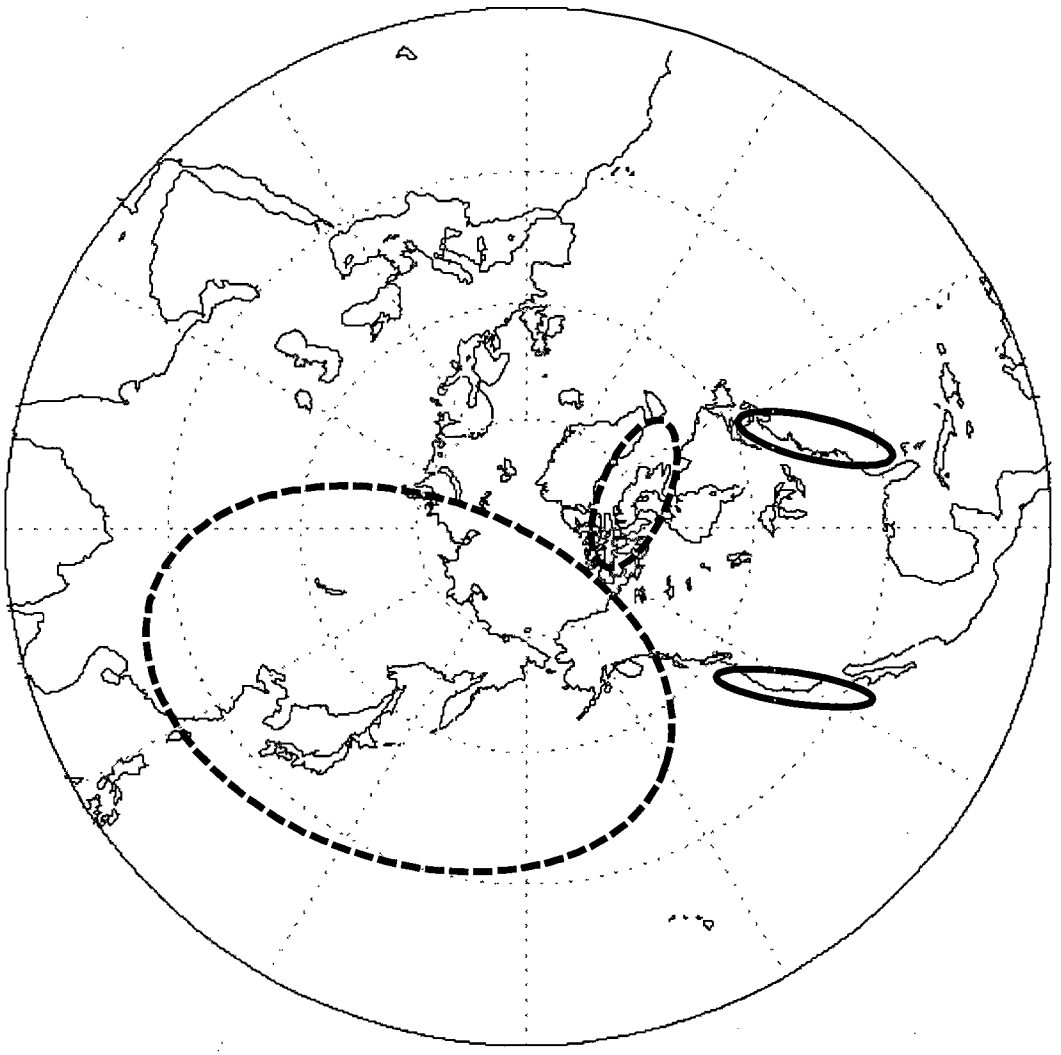

Figure 45 - Possible stratospheric (dashed ellipses) and tropospheric (solid ellipses) source regions of ozone that arrived in the LFV during the four case studies in Section 4.3.

5. Discussion

5.1 Possible Source Regions of Ozone

Using the trajectory figures in Section 4.3 (Figures 26, 30, 34-36 and 42-43), it is possible to draw some conclusions about the general non-local source regions of ozone in the LFV during the four case studies. By non-local source regions, it is meant that this ozone was not produced in-situ, but was transported from another regions by the synoptic and local wind. Figure 45 shows the possible stratospheric and tropospheric source regions of ozone that arrived in the LFV during the four case

studies in Section 4.3. The largest possible source region of stratospheric ozone encompasses an area between the central North Pacific Ocean and the Northern Arctic Ocean in the north south direction and Central Siberia and Eastern Alaska in the east - west direction. With the exception of Figure 30 in Case Study 2 and Figure 34 in Case Study 3, all of the trajectories originated from this source region at altitudes between 0 m a.s.l. to 9000 m a.s.l. It is important to note that this general region was also the location of many of the upper level troughs\cutoff lows and associated synoptic scale surface low pressure systems described in the case studies. It was suggested in Section 4.3 that these synoptic systems could have been responsible for the transport of ozone-rich stratospheric air into the troposphere by various mechanisms (i.e. tropopause folds, decent of stratospheric air into a cutoff low etc.). This region should therefore be the focus of future research into the long range transport of stratospheric ozone to the Pacific Northwest.

Case Study 2 in Section 4.3 produced an interesting example where possibly both stratospheric and anthropogenically/naturally produced tropospheric ozone were encountered along the same trajectory path (Figure 30). During this case study several trajectories originated over the eastern seaboard of the United States at altitudes around 2000 m. As these trajectories moved northwards, they could have encountered stratospheric air in a cutoff low situated over Northern Canada before traveling southwards and descending into the LFV. In Section 4.3.2.3 it was noted that similar multiple source trajectory case studies have been previously identified in the Swiss Alps by Stohl and Trickl (1999). These two possible source regions are indicated in Figure 45 as the circles situated over the eastern seaboard of the United States and over the Arctic region of Canada.

The final possible source region located over the western seaboard of the United States is tropospheric in origin. This occurred during Case Study 3 (Figure 34). Although all of the trajectories in this figure stayed below 1500 m a.g.l. during the entire back trajectory period, this example illustrates that, during an elevated ozone episode, the source regions could be either tropospheric (Figure 34) or stratospheric (Figures 35-36) in origin.

It should be noted that, during the current research, trajectories originating from lower tropospheric levels over the Eurasian continent may be encountering anthropogenically produced ozone that originated in this region. This transport is made possible by the warm conveyor belt (WCB) process whereby ozone and other anthropogenic pollutants are lofted into the upper troposphere by frontal systems, transported over a great distance over several days (in this case, across the Pacific Ocean) and then subsiding to the surface thereby elevating surface level pollutant concentrations. Stohl *et al.* (2002) and Jaffe *et al.* (2003) have investigated WCB case studies and performed modelling in the Eurasian and North Pacific.

5.2 General Trajectory Error – A Brief Discussion

Although meteorological trajectories are used widely in atmospheric science, especially with research involving STE (Stohl *et al.*, 2002, Stohl and Trickl, 1999, Schuepbach *et al.*, 1999, Sorensen and Nielsen, 2001, Viezee *et al.*, 1983, Wakamatsu *et al.*, 1989, Haagenson *et al.*, 1981, Kim *et al.*, 2002, Lamb, 1977, Parrish *et al.*, 2000), the errors associated with trajectories are rarely reported or even acknowledged (Stohl *et al.*, 2002). The lack of acknowledgement of trajectory error has serious consequences, especially if the computed trajectories are taken at face value with no validation against other meteorological data and analysis (Stohl *et al.*, 2002). Rather than go into an in-depth trajectory error analysis, this section will cover some of the

sources of trajectory error and suggest some possible alternatives to simple single meteorological back trajectories.

One of the larger sources of trajectory error can occur before the model is even run. If the meteorological model output being fed into the trajectory model is inaccurate, then the trajectory results will be inaccurate as well (Stohl, 1998). Even if the meteorological model output is of good quality, the grid point resolution of the output may be too coarse. This requires a greater amount of interpolation between grid points when the trajectory model is being run. When using trajectory models that utilize meteorological model output with a fine grid point resolution, one must be aware that the model being used to generate the meteorological model output in the first place may not have sufficient initialization data. This will thus require a fair amount of interpolation as that meteorological model is running. This could result in substantial interpolation errors in the meteorological model output.

While the model is running, two main sources of error can occur. Firstly, error can occur when the wind velocity is interpolated from grid points in the meteorological model output (Rolph and Draxler, 1990, Doty and Perkey, 1993, Stohl *et al.,* 1995). This will lead to errors in the actual trajectory positions especially if the spacing between the grid points is large (Stohl *et al.*, 2002). This error can be kept to a minimum if the quality of the meteorological model output is good and the spacing between the grid points is small. A second error can occur when the numerical solution to the trajectory equation is truncated due to computer memory and storage issues (Walmsley and Mailhot, 1983, Seibert, 1993). Because of the steady improvement in numerical schemes, coupled with increasing computer memory and storage, truncation errors are very small when compared to interpolation errors (Stohl *et al.*, 2002). When all of these factors are taken into account, the resulting trajectory

positional errors are typically on the order of 15%-20%, but can reach as high as 100% (Stohl *et al.*, 2002).

There is one other complication that must be considered when using meteorological trajectories. This complication arises from the fact that trajectories are the paths of infinitesimally small particles of air and are thus not representative of finite volumes (Stohl *et al.*, 2002). The reason for this is that finite volumes of air can be deformed by flowing around physical objects (i.e. flow around a mountain) or by wind shear in both the horizontal and vertical. Thus, a unit volume of air may be stretched by many units in the horizontal and the vertical as it transported by the flow (Seims *et al.,* 2000, Pudykiewicz and Koziol, 1998). Because of this deformation, two infinitesimally small particles, initially close together in a finite volume, could be separated by large distances even over relatively short trajectory run times (Stohl *et al.*, 2002). One possible solution to this problem would be to set up an ensemble of trajectories (Merrill *et al.,* 1985, Kahl, 1993, Kahl, 1996). Using this technique, a number of "supporting" trajectory end point receptors are set up around the main end point receptor so that a more representative sample of a unit finite volume may be realized.

5.3 CANERM and HYSPLIT Model Comparison

During several measurement campaigns involving transport of particulates, pollutants and ionizing radiation, more than one trajectory model was often utilized (Hsu *et al.,* 2003, Lupu and Maenhaut, 2002, N'dri Koffi *et al*, 1998, Baumann and Stohl, 1997). The major benefit of using multiple trajectory models is that it provides an opportunity for multiple agencies, institutions and governments to test and compare their model's output against other models and available atmospheric data such as balloon flight tracks (both manned and unmanned) (Baumann and Stohl,

1997). If large discrepancies occur between the models and/or between the available atmospheric data and the model output, the model can be corrected so that its output agrees more favorably with the available data. One such experiment, ETEX (European Tracer EXperiment) involved the use of radiation and other data collected during and after the Chernobyl nuclear disaster in 1986. Further details on this project can be found in Graziani (1998) and Nodop (1997).

Although a model intercomparison study like ETEX is far beyond the scope of the current research it is still necessary to compare the model output obtained from CANERM with model output from another model even if only at a basic level. The main objective was to determine which of the seven sets of ensemble back trajectories (Figures 26, 30, 34-36 and 42-43) in the case studies in Section 4.3 showed good positional agreement (i.e. latitude, longitude and height) between the two trajectory models and which ensemble back trajectory sets did not show good positional agreement. The trajectory model used for intercomparison was the HYSPLIT model outlined in Section 4.2.1.

In order to compare the positions of the trajectory paths produced by HYSPLIT and CANERM, the HYSPLIT model was first run during the same seven trajectory release times as CANERM indicated in Figures 26, 30, 34-36 and 42-43. Next, for each model run, the latitude, longitude and height of the nine trajectory paths originating at 100 m a.g.l., 500 m a.g.l. and 1000 m a.g.l. respectively were averaged every six hours. This resulted in an average trajectory path for each end point receptor height (100 m a.g.l., 500 m a.g.l. and 1000 m a.g.l.) for each model run. This procedure was carried out for both models. Finally, the positional (latitude, longitude and height) differences between these CANERM and HYSPLIT average trajectory paths were found. The resulting plots (Figure 46) show the absolute positional

differences between the two models over the entire back trajectory time for each of the seven model runs.

Upon inspection of the plots in Figure 46, it is immediately apparent that there is a substantial amount of disagreement between the two models. Generally, this disagreement increases as the trajectory run progresses. The latitudinal disagreement was generally less than 10°, but differences as high as 18° did occur in several cases (Figures 46b and 46e). Typical longitudinal differences were almost twice as high at 20°, but maximum differences did climb to between 30° and 60°. Typically, the height differences were less than 1000 m for the first 24 – 72 hours. After 72 hours, the height differences rose quite sharply to values exceeding 3000 m in some cases. Only Figures 46c and 46f showed relatively small positional differences between the two models during the entire model run time with latitudinal (with one exception), longitudinal and height (with one exception) differences not exceeding 6°, 10° and 1200 m respectively. Figures 46a, 46b and 46e showed the least agreement between the two models in latitude, longitude and height.

Although it is beyond the scope of the current research to speculate why these differences are so large, it is necessary to point out that care must be taken when performing trajectory studies. Trajectory errors and model disagreement can become quite large (Stohl *et al.*, 2002) and supplemental atmospheric data (surface station data, ozone, radiation, synoptic analysis and satellite imagery) and analyses must be utilized to validate the trajectory results.

a).

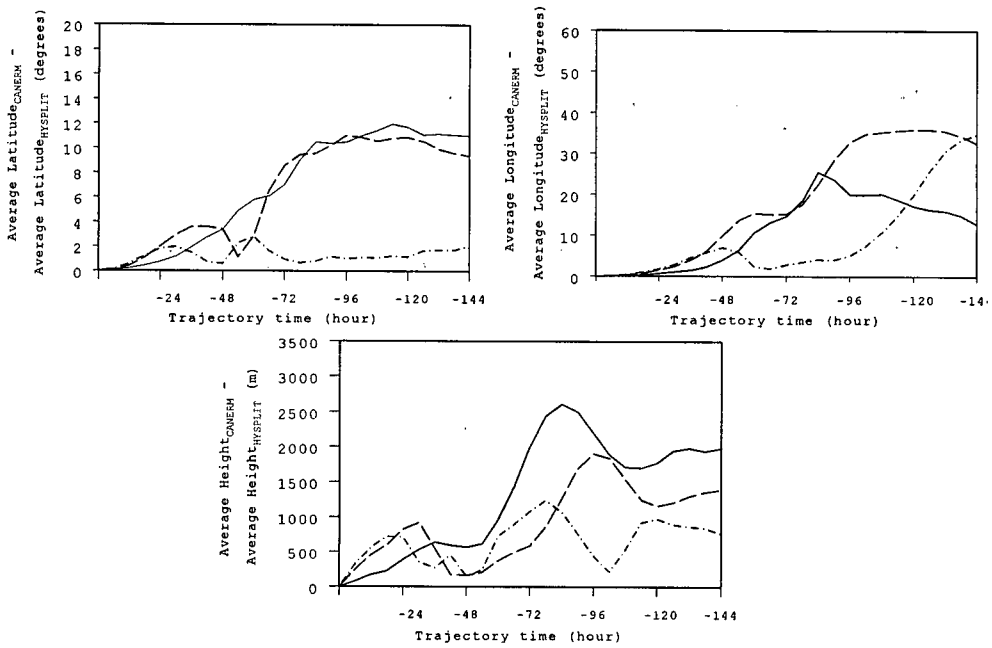

Average CANERM values - Average HYSPLIT values for end point receptors at 100 m a.s.l.
Average CANERM values - Average HYSPLIT values for end point receptors at 500 m a.s.l.
Average CANERM values - Average HYSPLIT values for end point receptors at 1000 m a.s.l.

b).

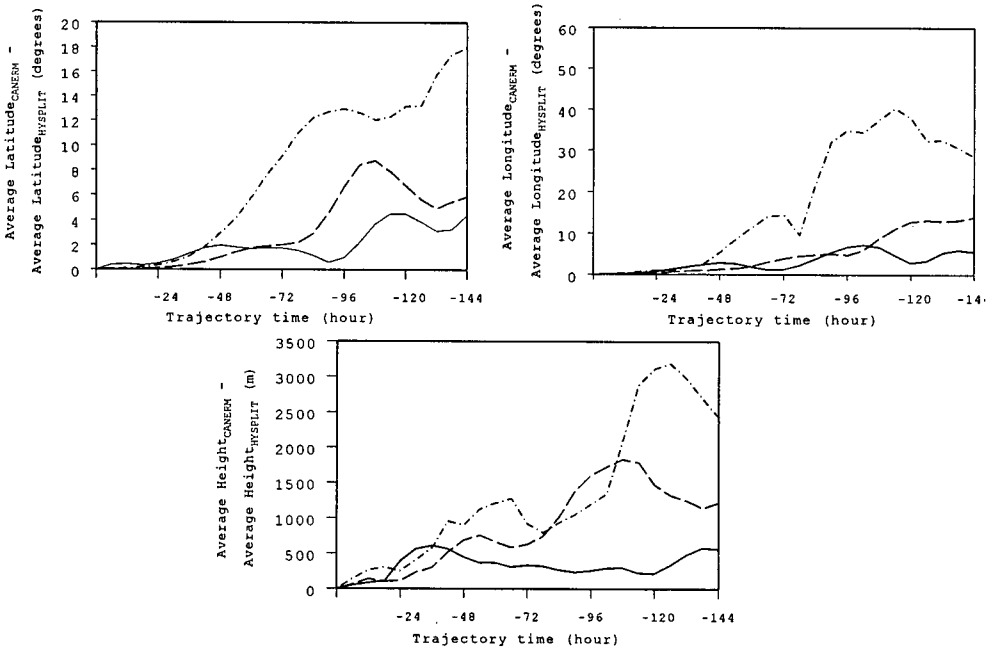

Average CANERM values - Average HYSPLIT values for end point receptors at 100 m a.s.l.
Average CANERM values - Average HYSPLIT values for end point receptors at 500 m a.s.l.
Average CANERM values - Average HYSPLIT values for end point receptors at 1000 m a.s.l.

c).

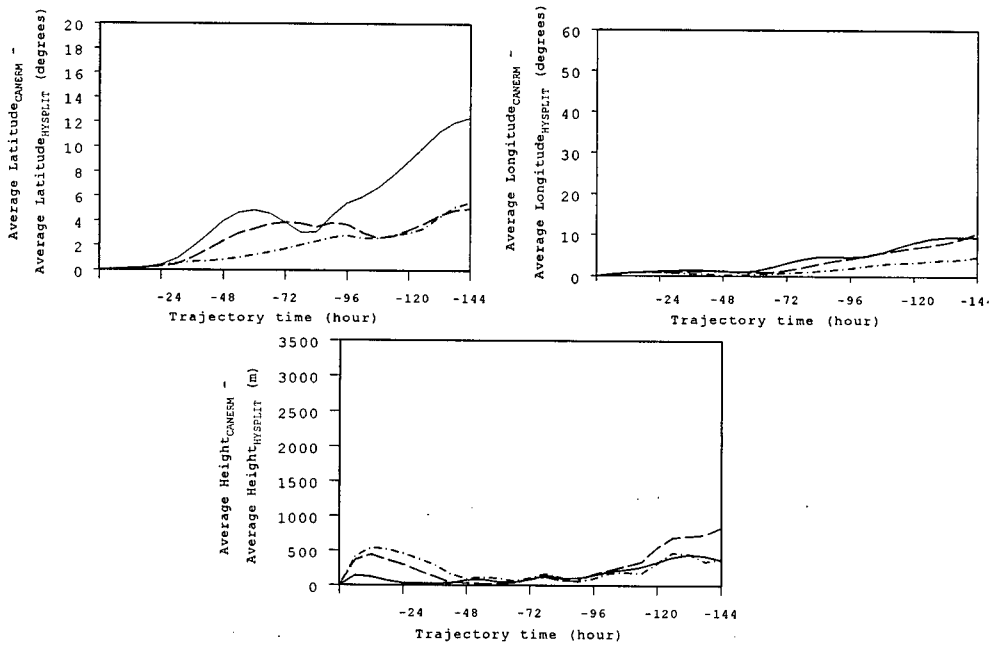
Average Latitude CANERM - Average Latitude HYSPLIT (degrees)
Trajectory time (hour)
Average Longitude CANERM - Average Longitude HYSPLIT (degrees)
Trajectory time (hour)
Average Height CANERM - Average Height HYSPLIT (m)
Trajectory time (hour)
Average CANERM values - Average HYSPLIT values for end point receptors at 100 m a.s.l.
Average CANERM values - Average HYSPLIT values for end point receptors at 500 m a.s.l.
Average CANERM values - Average HYSPLIT values for end point receptors at 1000 m a.s.l.

d).

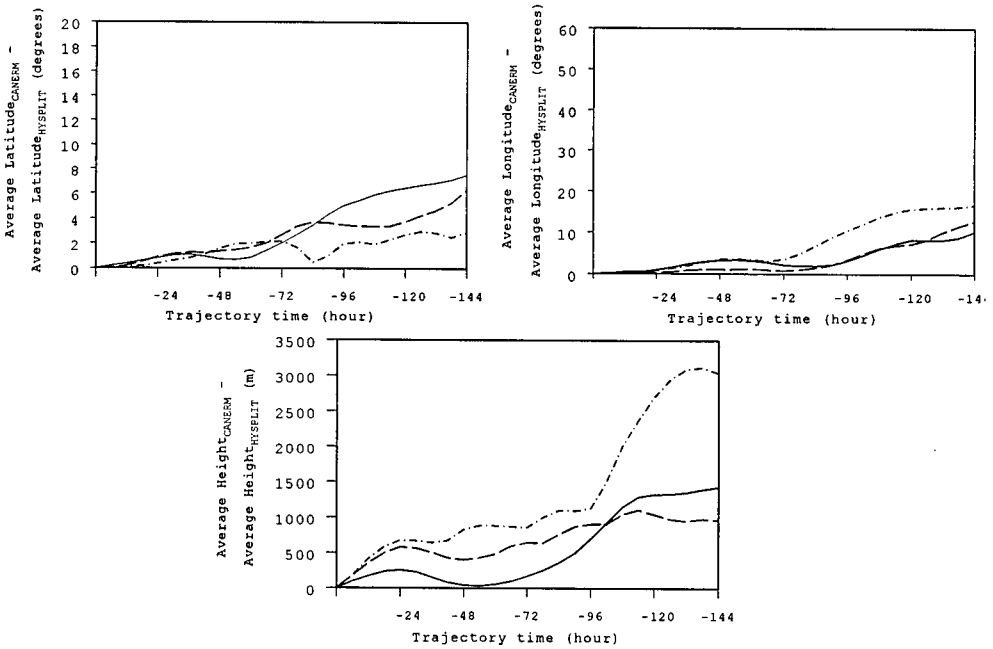
Average Latitude CANERM - Average Latitude HYSPLIT (degrees)
Trajectory time (hour)
Average Longitude CANERM - Average Longitude HYSPLIT (degrees)
Trajectory time (hour)
Average Height CANERM - Average Height HYSPLIT (m)
Trajectory time (hour)
Average CANERM values - Average HYSPLIT values for end point receptors at 100 m a.s.l.
Average CANERM values - Average HYSPLIT values for end point receptors at 500 m a.s.l.
Average CANERM values - Average HYSPLIT values for end point receptors at 1000 m a.s.l.

e).

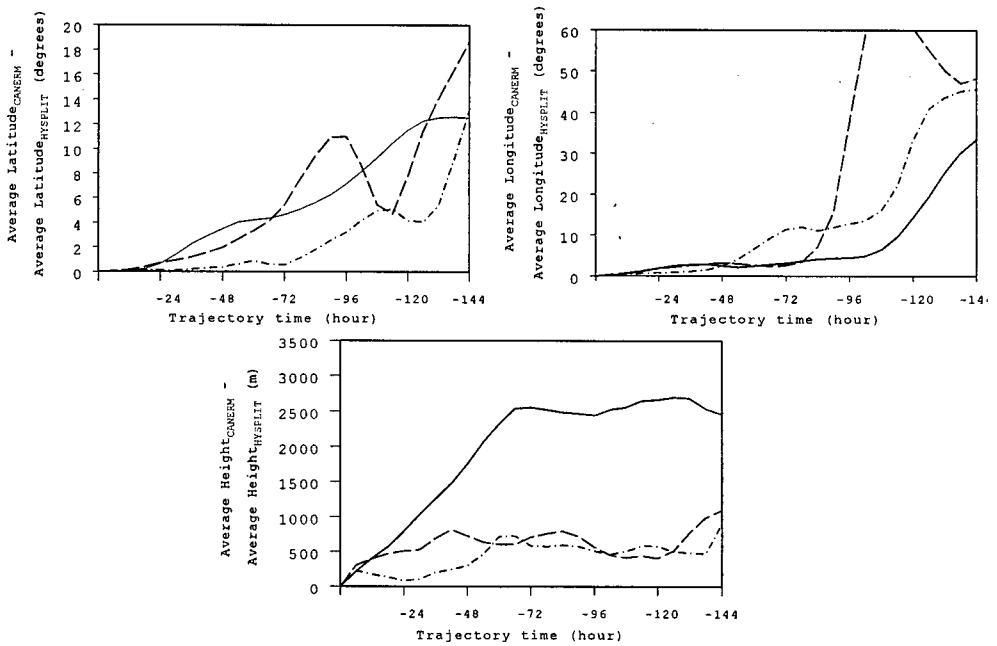

Average CANERM values - Average HYSPLIT values for end point receptors at 100 m a.s.l.
Average CANERM values - Average HYSPLIT values for end point receptors at 500 m a.s.l.
Average CANERM values - Average HYSPLIT values for end point receptors at 1000 m a.s.l.

f).

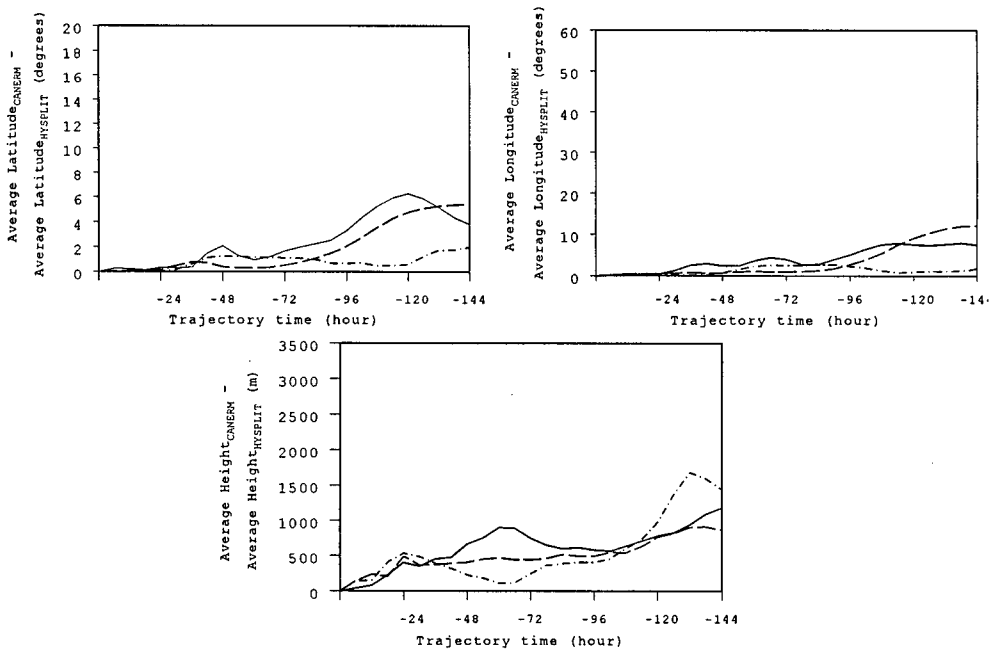

Average CANERM values - Average HYSPLIT values for end point receptors at 100 m a.s.l.
Average CANERM values - Average HYSPLIT values for end point receptors at 500 m a.s.l.
Average CANERM values - Average HYSPLIT values for end point receptors at 1000 m a.s.l.

g).

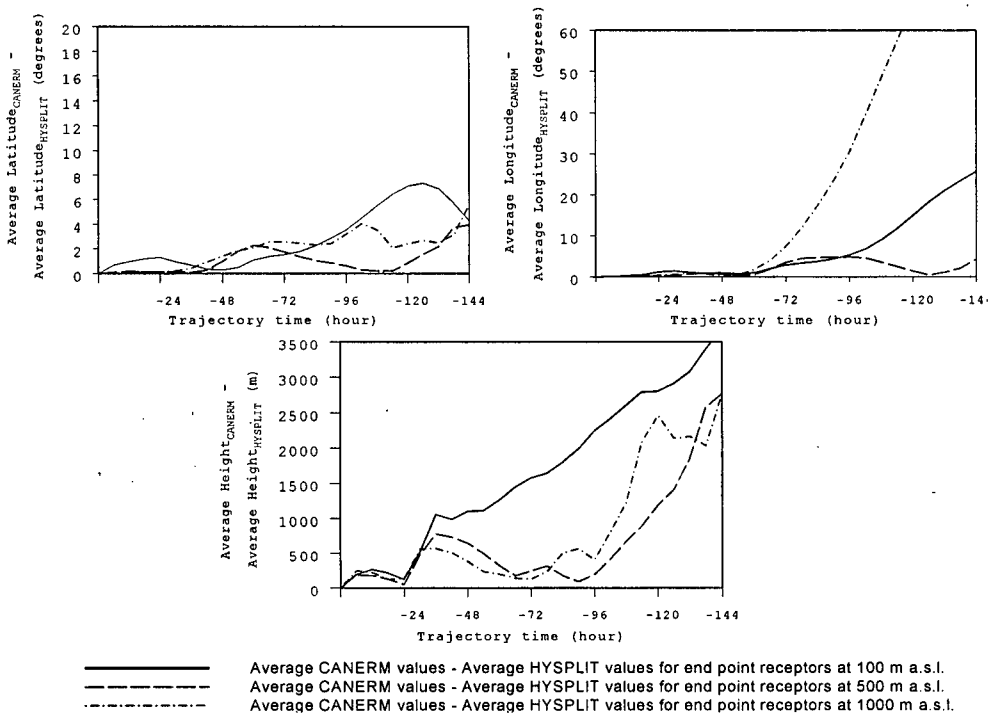

Figure 46 - Absolute latitudinal, longitudinal and height differences between the CANERM and HYSPLIT models for back trajectory runs starting at 100 m a.g.l (solid line), 500 m a.g.l. (dashed line) and 1000 m a.g.l. (stipled line) over the LFV for a) 31 October 1.

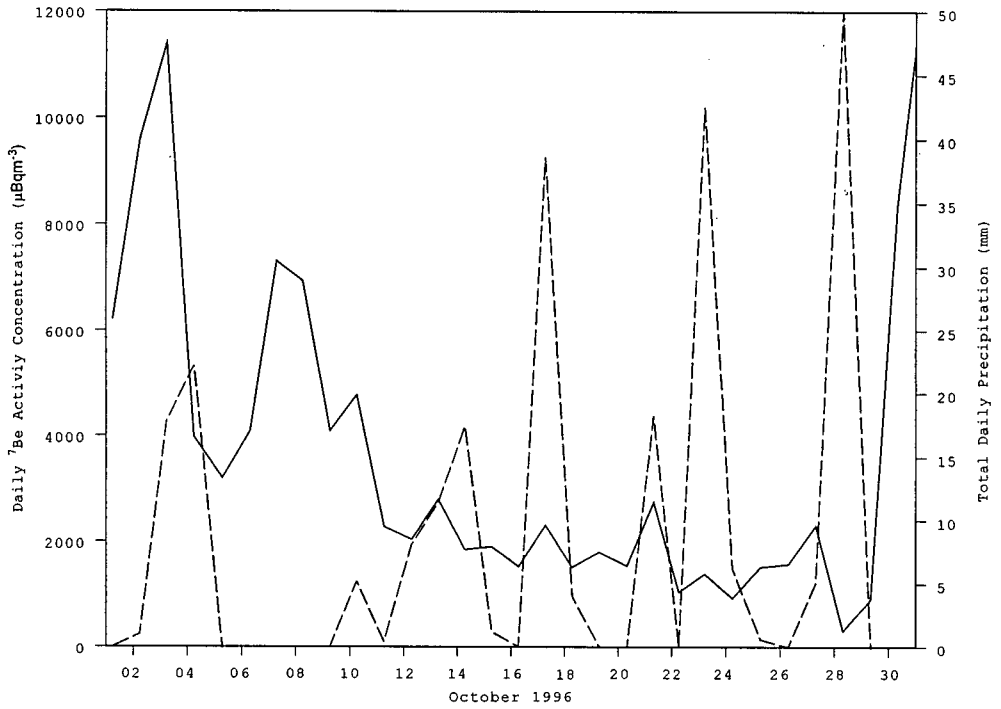

Figure 47 - Daily ^{7}Be activity concentrations measured at the CTBTO IMS station CA002 (solid line) and total daily precipitation measured at Vancouver International Airport (dashed lines) during October 1996.

5.4 Precipitation and it Influence on ^{7}Be Concentrations

In Section 2.1 it was noted that ^{7}Be was susceptible to scavenging by precipitation. Figure 47 illustrates this phenomenon in two different ways. Firstly, when there are frequent precipitation events, the ^{7}Be concentrations remain low. Secondly, the daily ^{7}Be activity concentration drops dramatically even during low to moderate precipitation events. Figure 48 illustrates a period during which there is very little precipitation. Unlike Figure 47, a high ^{7}Be concentration event can be seen in its entirety with concentrations rising from background levels to its maximum and then slowly decreasing to background concentrations again. These examples illustrate the need for both wet and dry deposition measurements at radionuclide stations so that all of the high ^{7}Be events may be captured.

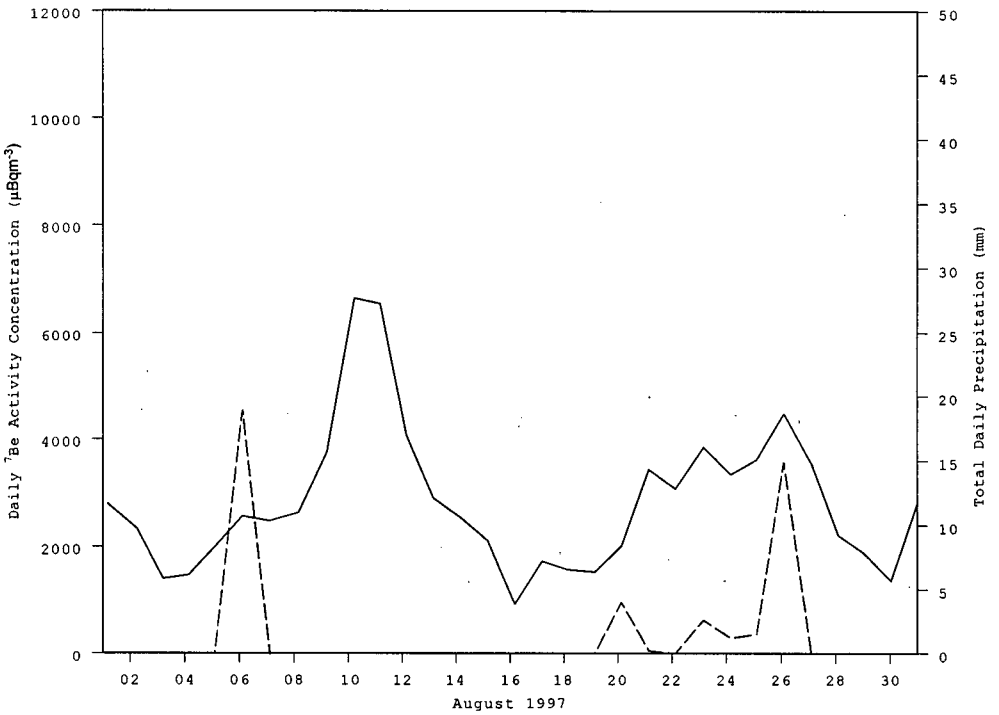

Figure 48 - Daily 7Be activity concentrations measured at the CTBTO IMS station CA002 (solid line) and total daily precipitation measured at Vancouver International Airport (bars) during August 1997.

In order to quantitatively determine whether precipitation reduces the daily ^{7}Be activity concentrations at the CTBTO IMS station CA002 on the UBC campus, a simple one sided t-test was performed. For this t-test, the null hypothesis was that the average daily ^{7}Be activity concentration during days in which there was measured precipitation was equal to the average daily ^{7}Be activity concentration during days in which there was no measured precipitation and that any variation was due strictly to chance. The alternative hypothesis was that the average daily ^{7}Be activity concentration during days in which there was measured precipitation was significantly lower than the average daily ^{7}Be activity concentration during days in which there was no measured precipitation. The standard choice of significance level (or P value) for a one sided test of 2.5% (0.025) was used to accept or reject the null hypothesis (Samuels, 1989). Using a one sided t-test and an unpooled standard error, a P value

of 2.5×10^{-7} was found. Since this P value is much less than the chosen significance level of 0.025, the null hypothesis was rejected in favor of the alternative hypothesis. This means that the difference between the average daily ^{7}Be activity concentration during days in which there was precipitation was significantly lower than days in which there was no precipitation. Thus precipitation does reduce the dry deposition ^{7}Be activity concentrations at the CTBTO IMS station CA002 at UBC.

6. Conclusions

Using hourly ozone and daily ^{7}Be activity concentration data during the period of 10 April 1996 – 12 March 2002, two different detection algorithms uncovered several episodes in which stratospheric ozone may be influencing ground level ozone concentrations in the LFV. The 80^{th} percentile detection algorithm was more effective in uncovering spring and summer episodes because the criteria behind this algorithm depended on both high daily ^{7}Be activity concentrations and high ADM ozone concentrations. Because the ADM ozone concentration was required to be in the 80^{th} percentile, a large number of episodes in which anthropogenically derived ozone may have had a strong influence on ground level ozone concentrations may have been included in these episodes. This argument was supported by Figure 14 which showed that during the months in which the 80^{th} percentile algorithm was selecting episodes, the ADM temperature was high and would thus tend to produce favorable conditions for anthropogenically derived ozone production. The concern about these episodes was that the anthropogenically derived ozone concentration may be so large that it effectively drowns out the stratospheric contribution to the total ground level ozone concentration. In order to partially alleviate this problem, months during which the ADM temperatures were high were eliminated from the data set before the 80^{th} percentile algorithm was applied. Although a few episodes during late

fall and late winter were uncovered (Figures 20-21), the algorithm failed to uncover any episodes between November and January.

The second algorithm relied only on high ^{7}Be activity concentrations in the hope that more episodes would be uncovered during the fall and winter months when the ADM temperatures were low and thus stratospheric ozone would be making a greater contribution to the total ground level ozone concentration. The resulting episodes that were detected by this algorithm took place during all months of the year with several episodes occurring during the late fall and winter months. Although the ozone concentrations were low during this time, a number of interesting episodes were uncovered during which the hourly ozone concentrations, especially in the rural areas, exhibited a classical stratospheric pattern whereby ozone concentrations rose sharply from near zero background levels to values exceeding 30 ppb within the span of only a few hours. These elevated concentrations then remained fairly constant for several days (with very little or no nocturnal NO_x scavenging) before slowly decreasing to background levels again.

Four episodes of the type described above were more fully investigated using meteorological back trajectories, surface temperature and precipitation measurements, synoptic charts and satellite data. The goals of these case studies were to uncover possible source regions of stratospheric ozone and the transport pathways of this ozone from these source regions to the LFV. During these case studies, a large number of back trajectories arriving over the LFV were found to have originated over an area spanning Eastern Russia and China, Japan, the North Pacific and Arctic Oceans and Alaska (Figure 45). Many trajectories within this region reached altitudes between 5000 m to over 9000 m a.g.l. During these case studies, a large number of upper level troughs/cutoff lows and surface low pressure systems were present in this

area. Pervious research has indicated that these synoptic systems are largely responsible for the injection of ozone-rich stratospheric air into the troposphere by way of tropopause folds. These case studies also uncovered situations in which multiple ozone sources were intercepted by the same trajectory.

Using a simple one sided t-test, it was found that precipitation does decrease the daily ^{7}Be dry deposition activity concentrations. This would suggest that wet deposition measurements of ^{7}Be should be taken although the cost may limit these types of measurements to case studies only.

Although a numerical analysis of the absolute contribution of stratospheric ozone to the total ground level ozone concentration is beyond the scope of this research, it is important to note that, during the case studies described in Section 4, two features become apparent. Firstly, the elevated ozone concentrations during the case studies seem to be making an important contribution in the rural areas. Using Figure 16 as a rough guide, a total stratospheric contribution of up to 10-20 ppb may be considered to be a reasonable first guess. Secondly, there is very little nocturnal NO_x scavenging in the rural areas during these episodes. The total nocturnal stratospheric contribution will therefore be greater than during the daytime. Again, using Figure 16 as a rough guide, the total nocturnal stratospheric contribution could be as high as 20-40 ppb. This stratospheric contribution can thus not be ignored when decisions are being made with regards to ground level ozone reduction programs. It addition, the current research raises the question about the health effects resulting from long term (on the order of a few days) exposure to constant moderate ozone concentrations as experienced in the rural areas in Figure 16 as opposed to acute exposure (on the order of a few hours) to high ozone concentrations. This may be an interesting topic of future research.

6.1 Future Research

In the future, the current research may be extended to include the following:

1. Using the methods outlined in the current research, ^{7}Be and ozone data could be made available from other areas of Canada so that the source regions of stratospheric ozone could be determined for those areas.
2. The synoptic types (McKendry 1994, Yarnal 1993) under which stratospheric ozone is detected in the LFV should be investigated using existing synoptic typing techniques. It may be that a sequence of synoptic types will have to be defined since STE that leads to increased surface concentrations of ozone and ^{7}Be in the LFV is suspected to occur far offshore.
3. During periods in which these STE synoptic types are forecasted to occur, wet deposition measurements could be taken at the CTBTO IMS station CA002 at UBC so that the total ^{7}Be and ozone transported from the stratosphere to the surface may be measured.
4. Greater use of water vapor satellite data could be used in conjunction with a long range atmospheric dispersion model to determine the spatial structure and fate of stratospheric air that is injected into the troposphere. This technique has already been utilized by Stohl *et al.* (2000). Briefly, Stohl *et al.* (2000) found good agreement between dry lines in satellite imagery (possible areas of dry stratospheric air descending into the troposphere) and high ozone tracer mixing ratios between 2000 m and 4000 m a.s.l. predicted by the dispersion model.
5. In addition to ^{7}Be, ^{10}Be (1/2 life = 1.5×10^{6} years) measurements could be taken and a $^{10}Be/^{7}Be$ ratio could thus be utilized. Because dry and wet deposition are negligible in the stratosphere and the half life of ^{10}Be is so much larger than ^{7}Be, $^{10}Be/^{7}Be$ ratios are normally higher in the stratosphere compared to the

troposphere. Like ^{7}Be, ^{10}Be also attaches to aerosols which are then susceptible to scavenging. Wet deposition measurements of either species are therefore not necessary. Thus, at the surface, high dry deposition $^{10}Be/^{7}Be$ ratios denote possible STE episodes. Unfortunately ^{10}Be has to be measured using accelerator mass spectrometry (compared to high-resolution gamma spectrometry for ^{7}Be), which can be quite expensive. So far, only short term studies such as those outlined in Zanis *et al* (2003) and Dibb *et al.* (1994).

7. References

Ancellet, G., Pelon, J., Beekman, M., Papayannis, A., Megie, G., 1991: Ground-based lidar studies of ozone exchanges between the stratosphere and the troposphere. *Journal of Geophysical Research*, **96**, 22401-22421.

Appenzeller, C., Davies, H.C., 1992: Structure of stratospheric intrusions into the troposphere. *Nature*, Vol. 358, 570-572.

Bates, D.R., Nicolet, M., 1950: The photochemistry of atmospheric water vapour. *Journal of Geophysical Research*, **55**, 301.

Baumann, K., Stohl, A., 1997: Validation of a long-range trajectory model using gas balloon tracks from the Gordon Bennett Cup 95. *Journal of Applied Meteorology*, **36,** 711-720.

Bonasoni, P., Evangelisti, F., Bonafe, U., Ravegnani, F., Calzolari, F., Stohl, A., Tositti, L., Tubertini, O., Colombo, T., 1999: Stratospheric ozone intrusion episodes recorded at Mt. Cimone during the VOTALP project: case studies. *Atmospheric Environment,* **34**, 1355-1365.

Bovis, P., Steyn, D.G., 2001: Stratosphere-troposphere exchange and its influence on surface ozone concentrations in the Lower Fraser Valley – A preliminary report. *Report published internally to Health Canada.*

Caillet, S., Arpagaus, P., Monna, F., Dominik, J., 2001: Factors controlling ^{7}Be and ^{210}Pb atmospheric deposition as revealed by sampling individual rain events in the region of Geneva, Switzerland. *Journal of Environmental Radioactivity*, **53**, 241-256.

Chapman, S.A., 1930: A theory of upper atmospheric ozone. *Royal Meteorological Society*, **3**, 103.

Cho, J.Y.N., Newwll, R.E., Bui, T.P., Browell, E.V., Fenn, M.A., Mahoney, M.J., Gregory, G.L., Sachse, G.W., Vay, S.A., Kucsera, T.L., Thompson, A.M., 1999: Observations of convective and dynamical instabilities in tropopause folds and their contribution to stratosphere-troposphere exchange. *Journal of Geophysical Research,* **104 (D17)**, 21,549-21,568.

Chung, Y.S., Dann, T., 1984: Observations of stratospheric ozone at the ground level in Regina, Canada. *Atmospheric Environment,* **19**, 157-162.

Danielson, E.F., 1968: Stratospheric-tropospheric exchange based on radioactivity, ozone and potential vorticity. *Journal of the Atmospheric Sciences,* **52**, 502-518.

Danielsen, E., Bleck, R., Shedlovsky, J., Wartburg, A., Haagenson, P., Pollock, W., 1970: Observed distribution of radioactivity, ozone and potential vorticity associated with tropopause folding. *Journal of Geophysical Research*, **75**, 2353-2361.

Danielsen, E.F., Mohnen, V.A., 1977: Project Dustorm report: ozone transport, in situ measurements and meteorological analysis of tropopause folding. *Journal of Geophysical Research*, **82,** 5867-5877.

Davies, T. D., Schuebach, E., 1993: Episodes of high ozone concentrations at the earth's surface resulting from transport down from the upper troposphere/lower stratosphere: review and case studies. *Atmospheric Environment,* **28**, 53-68.

Dibb, J.E., Meeker, L.D., Finkel, R.C., Southon, J.R., Caffee, M.W., Barrie, L.A., 1994: Estimation of stratospheric input into the Arctic troposphere: ^{7}Be and ^{10}Be in aerosols in Alert, Canada. *Journal of Geophysical Research*, **99**, 12855-12864.

Doty, K.G., Perkey, D.J., 1993: Sensitivity of trajectory calculations to the temporal frequency of wind data. *Monthly Weather Review*, **121**, 387-401.

Draxler, R.R., Hess, G.D., 1997: Description of the Hysplit_4 modeling system. *NOAA Tech Memo ERL ARL-224, Dec,* 24p.

Dutkiewicz, V.A., Husain, L., 1985: Stratospheric and tropospheric components of ^{7}Be in surface air. *Journal of Geophysical Research*, **90**, 5783-5788.

Fast, J.D., Berkowitz, C.M., 1997: Evaluation of back trajectories associated with ozone transport during the 1993 North Atlnatic Regiona Experiment. *Atmospheric Environment*, **31**, 825-837.

Feely, H., Larsen, R., Sanderson, C., 1989: Factors that cause seasonal variations in beryllium-7 concentrations in surface air. *Journal of Environmental Radioactivity,* **9**, 223-249.

Gislason, K.B., Prahm, L.P., 1983: Sensitivity study of air trajectory long-range transport modelling. *Atmospheric Environment*, **12**, 2463-2472.

Graziani, G., Galmarini, S., Grippa, G., Klug, W. (Eds.), 1998: Real-Time Long-Range Dispersion Model Evaluation of the Second ETEX Release. Luxembourg, Office for Official Publications of the European Communities.

Gusten, H., Heinrirh, G., Cvitas, T., Klasing, L., Ruscic, B., Lalas, P.D., Petrakis, M., 1988: Photochemical formation and transport of ozone in Athens, Greece. *Atmospheric Environment,* **22,** 1855-1861.

Haagenson, P.L., Shapiro, M.A., Middleton, P., Laird, A.R., 1981: A case study relating high ground level ozone to enhanced photochemistry and isentropic transport from the stratosphere. *Journal of Geophysical Research,* **86**, 5231-5237.

Haagen-Smit, A.J., 1952: Chemistry and physiology of Los Angeles smog. *Industrial Engineering Chemistry*, **44**, 1342-1346.

Haagen-Smit, A.J., Bradley, C.E., Fox, M.M., 1953: Ozone formation in chemical oxidation of organic substances. *Industrial Engineering Chemistry*, **45**, 2086-.

Haagen-Smit, A.J., Darley, E.F., Zaitlin, M., Hull, H., Noble, W., 1951: Investigation on injury to plants from air pollution in the Los Angeles area. *Plant Physiology,* **27**, 18-.

Haagen-Smit, A.J., Fox, M.M., 1954: Photochemical ozone formation with hydrocarbons and automobile exhaust. *Journal of the Air Pollution Control Association,* **4**, 105-109.

Haagen-Smit, A.J., Fox, M.M., 1955: Automobile exhaust and ozone formation. SAE Technical Series No. 550277. Warrendale, Penn.: Society of Automotive Engineers.

Haagen-Smit, A.J., Fox, M.M., 1956: Ozone formation in photochemical oxidation of organic substances. *Industrial Engineering Chemistry,* **28**, 1484-.

Heffter, J.L., Stunder, B.J.B., 1993: Volcanic Ash Forecast Transport And Dispersion (VAFTAD) Model. *Weather Forecasting*, **8**, 534-541.

Hotzl, H., Winkler, R., 1987: Activity concentrations of ^{226}Ra, ^{228}Ra, ^{210}Pb, ^{40}K and ^{7}Be and their temporal variations in surface air. *Jounal of Environmental Radioactivity*, **5**, 445-458.

Hsu, T-K., Holsen, T.M., Hopke, P.K., 2003: Comparison of hybrid receptor models to locate PCB sources in Chicago. *Atmospheric Environment*, **37**, 545-562.

Ishikawa, Y., Murakami, H., Sekine, T., Yoshihara, K., 1995: Precipitation scavenging studies of radionuclides in air using ^{7}Be. *Journal of Environmental Radioactivity*, **26**, 19-36.

Janach, W.E., 1989: Surface ozone: trend details, seasonal variations, and interpretation. *Journal of Geophysical Research,* **94,** 18289-18295.

Johnson, W.B., Viezee, W., 1980: Stratospheric ozone in the troposphere - I. Presentation and interpretation of aircraft measurements. *Atmospheric Environment,* **15**, 1309-1323.

Juarez, A., Gray, C., Bravo, J.L., 1994: Influence of urban ozone in the measurements of the total ozone column in Mexico City. *ATMOSFERA*, **8**, 35-43.

Kahl, J.D., 1993: A cautionary note on the use of air trajectories in interpreting atmospheric chemistry measurements. *Atmospheric Environment*, **27A**, 3037-3038.
Kahl, J.D., 1993: A cautionary note on the use of air trajectories in interpreting atmospheric chemistry measurements. *Atmospheric Environment*, **27A**, 3037-3038.

Kato, H., Fujita, S-I., Nishinomiya, S., 1990: Mechanism of spring high-oxidant episode - a meteorological analysis in and around the Hokuriku District, Japan. *Atmospheric Environment,* **24A**, 2023-2033.

Kim, Y.K., Lee, H.W., Park, J.K., Moon, Y.S., 2002: The stratosphere-troposphere exchange of ozone and aerosols over Korea. *Atmospheric Environment,* **36,** 449-463.

Lal, D., Peters, B., 1967: Cosmic ray produced radioactivity on the earth. *Handbuch der Physik*, **46**, 551-612.

Lamb, R.G., 1977: A case study of stratospheric ozone affecting ground level oxidant concentrations. *Journal of Applied Meteorology*, **16**, 780-794.

Lupu, A., Maenhaut, W., 2002: Application and comparison of two statistical trajectory techniques for identification of source regions of atmospheric aerosol species. *Atmospheric Environment*, **36**, 5607-5618.

Mayer, H., 1999: Air Pollution in cities. *Atmospheric Environment*, **33**, 4029-4037.

McKendry, I.G., 1994: Synoptic circulation and summertime ground-level ozone concentrations at Vancouver, British Columbia. *Journal of Applied Meteorology,* **33**, 627-941.

Measday, D.F., Stocki, T.J., Mason, L.R., Williams, D.L., 2001: Detection of anthropogenic radionuclides by the CA002 monitoring station for the comprehensive test ban treaty. *Health Physics*, **80**, 126-136.

Medici, F., The IMS radionuclide network of the CTBT. *Radiation Physics and Chemistry*, **61**, 689-690.

Megumi, K., Matsunami, T., Ito, M., Kiyoda, S., Mizohata, A., Takeyoshi, A., 2000: Factors, especially suinspot number, causing variations in surface air concentrations and depositions of ^{7}Be in Osaka, Japan. *Geophysical Research Letters*, **27**, 361-364.

Merrill, J.T., Bleck, R., Avila, L., 1985: modeling atmospheric transport to the Marshall Islands. *Journal of Geophysical Research*, **90**, 12927-12936.

Miller, C., Filkin, D.L., Owens, A.J., Steed, J.M., Jesson, J.P., 1981: A two dimensional model of stratospheric chemistry and transport. *Journal of Geophysical Research*, **86**, 1379.

Morison, R.P., Leslie, L.M., Speer, M.S., 2002: Atmospheric modeling of air pollution as a tool for environmental prediction and management. *Meteorology and Atmospheric Physics*, **80**, 141-151.

Murao, N., Ohta, S., Furuhashi, N., Mizoguchi, I., 1990: The causes of elevated concentrations of ozone in Sapporo. *Atmospheric Environment,* **24A**, 1501-1507.

National Research Council, 1992: Rethinking the ozone problem in urban and regional air pollution. Washington, National Academy Press.

N'dri Koffi, E., Nodop, K., Benech, B., 1998: Comparison of constant volume balloons, model trajectories and tracer transport during ETEX. *Atmospheric Environment*, **34**, 4139-4149.

Nodop, K. (Ed.), 1997: Proceedings of the ETEX Symposium on Long-Range Atmospheric Transport, Model Verification and Emergency Response. Luxembourg, Office for Official Publications of the European Communities.

Paatero, Jussi and Juha Hatakka, 2000: Source areas of airborne ^{7}Be and ^{210}Pb measured in Northern Finland. *Health Physics*, **76**, 691-696.

Parrish, D.D., Holloway, J.S., Jakoubek, R., Trainer, M., Ryerson, T.B., Hubler, G., Fehsenfeld, F.C., Moody, J.L., Cooper, O.R., 2000: Mixing of anthropogenic pollution with stratospheric ozone: a case study from the North Atlantic wintertime troposphere. *Journal of Geophysical Research,* **105**, 24363-24374.

Pont, V., Fontan, J., 2000: Local and regional contributions to photochemical atmospheric pollution in southern France. *Atmospheric Environment*, **34**, 5209-5223.

Prinn, R.G., Alyea, F.M., Cunnold, D.M., 1978: Photochemistry and dynamics of the ozone layer. *Annual Review of the Earth and Planetary Sciences*, **6**, 43.

Pudykiewicz, J., 1988 : Numerical simulation of the transport of radioactive cloud from the Chernobyl nuclear accident. *Tellus*, **40B**, 241-259.

Pudykiewicz, J., 1989 : Simulation Of The Chernobyl Dispersion With a 3-D Hemispheric Tracer Model. *Tellus*, **41B**, 391-412.

Pudykiewicz, J.A., Koziol, A.S., 1998: An application of the theory of kinematics of mixing to the study of tropospheric dispersion. *Atmospheric Environment,* **32**, 4227-4244.

Rao, S.T., Sistla, G., Schere, K., Godowitch, J., 1991: Analysis of ozone air quality over the New York metropolitan area. Air Pollution Modeling and its Application, Vol. VIII. Plenum Press, New York, NY, 111-121.

Realtime Environmental Applications and Display System (READY) website. NOAA Air Resource Laboratory (http://www.arl.noaa.gov/ready.html).

Rolph, G.D., Draxler, R.R., 1990: Sensitivity of three dimensional trajectories to the spatial and temporal densities of the wind field. *Journal of Applied Meteorology,* **29**, 1043-1054.

Samuels, M.L., 1989: Statistics for the life sciences. Englewood Cliffs, Prentice Hall.

Schuepbach, E., Davies, T.D., Massacand, A.C., 1998: An unusual springtime ozone episode at high elevation in the Swiss Alps: contributions from both cross-tropopause exchange and from the boundary layer. *Atmospheric Environment,* **33**, 1735-1744.

Seibert, P., 1993: Convergence and accuracy of numerical methods for trajectory calculations. *Journal of Applied Meteorology*, **32**, 558-566.

Seims, S.T., Hess, G.D., Suhre, K., Businger, S., Draxler, R., 2000: The impact of wind shear on observed and simulated trajectories during the ACE-1 Lagrangian experiments. *Australian Meteorological Magazine*, **30**, 579-587.

Seinfeld, J.H., 1986: Atmospheric chemistry and physics of air pollution. New York, John Wiley & Sons, Inc.

Sorensen, J.H., Nielsen, N.W., 2001: Intrusion of stratospheric ozone to the free troposphere through tropopause folds – a case study. *Physical Chemistry of the Earth (B)*, **26**, 801-806.

Stewart, R.W., Hameed, S., Pinto, J.P., 1977: Photochemistry of tropospheric ozone. *Journal of Geophysical Research*, **82**, 3134-.

Steyn, D.G., Bottenhiem, J.W., Thompson, R.B., 1997: Overview of tropospheric ozone in the Lower Fraser Valley, and the Pacific '93 field study. *Atmospheric Environment,* **31**, 2025-2035.

Stohl, A., 1998: Computation, accuracy and applications of trajectories – a review and bibliography. *Atmospheric Environment,* **32**, 947-966.

Stohl, A., Eckhardt, S., Forster, C., James, P., Spichtinger, N., Seibert, P., 2002: A replacement for simple back trajectory calculations in the interpretation of atmospheric trace substance measurements. *Atmospheric Environment*, **36**, 4635-4648.

Stohl, A., Seibert, P., 1998: Accuracy of trajectories as determined from the conservation of meteorological tracers. *Quarterly Journal of the Royal Meteorological Society*, **125**, 1465-1484.

Stohl, A., Spichtinger-Rakowsky, N., Bonasoni, P., Feldmann, H., Memmesheimert, M., Scheel, H.E., Trickl, T., Hubener, S., Ringer, W., Mandl, M., 1999: The influence of stratospheric intrusions on alpine ozone concentrations. *Atmospheric Environment,* **34**, 1323-1354.

Stohl, A., Trickl, T., 1999: A textbook example of long-range transport: Simultaneous observation of ozone maxima of stratospheric and North American origin in the free troposphere over Europe. *Journal of Geophysical Research,* **104 (D23)**, 30,445-30-462.

Stohl, A., Wotawa, G., 1995: A method for computing single trajectories representing boundary layer transport. *Atmospheric Environment*, **29**, 3235-3239.

Stohl, A., Wotawa, G., Seibert, P., Kromp-Kolb, H., 1995: Interpolation errors in wind fields as a function of spatial and temporal resolution and their impact on different types of kinematic trajectories. *Journal of Applied Meteorology,* **34**, 2149-2165.

Talpos, S., Cuculeanu, V., 1997: A study of the vertical diffusion of ^{7}Be in the atmosphere. *Journal of Environmental Radioactivity*, **36**, 93-106.

Tremblay, J., Servranckx, R., 1992: Beryllium-7 as a case of stratospheric ozone: a case study. *Journal of Radioanalytic and Nuclear Chemistry,* **172,** 49-56.

Tulet, P., Crassier, V., Rosset, R., 2000: Air pollution modelling at a regional scale. *Environmental and Modelling Software*, **15**, 693-701.

Viezee, W., Johnson, W.B., Singh, H.B., 1983: Stratospheric ozone in the lower troposphere II – assessment of downward flux and ground-level impact. *Atmospheric Environment,* **17**, 1979-1993.

Wakamatsu, S., Uno, I., Ueda, H., Uehara, Tateishi, K.H., 1989: Observational study of stratospheric ozone intrusions into the lower troposphere. *Atmospheric Environment,* **23**, 1815-1826.

Walmsley, J.L., Mailhot, J., 1983: On the numerical accuracy of trajectory models for long-range transport of atmospheric pollutants. *Atmospheric Ocean*, **21**, 14-39.

Wayne, R.P., 1999: Chemistry of atmospheres. New York, Oxford University Press.

Wunderli, S., Gehrig, R., 1991: Influence of temperature on formation and stability of of surface PAN and ozone. A two year field study in Switzerland. *Atmospheric Environment*, **25A**, 1599-1608.

Yarnal, B., 1993: Synoptic climatology in environmental analysis: a primer. Boca Raton, Belhaven Press.

Zanis, P., Gerasopoulos, E., Priller, A., Schnabel, C., Stohl, A., Zerefos, C., Gaggeler, H.W., Tobler, L., Kubik, P.W., Kanter, H.J., Scheel, H.E., Luterbacher, J., Berger, M., 2003: An estimate of the impact of stratosphere-to-troposphere transport (STT) on the lower free tropospheric ozone over the Alps using ^{10}Be and ^{7}Be measurements. *Atmospheric Environment.* **108**.

Zanis, P., Schuepbach, E., Gaggler, H.W., Hubener, S., Tobler, L., 1999: Factors controlling ^{7}Be at Jungfraujoch in Switzerland. *Tellus,* **51B**, 789-805.

Zannetti, P., 1990: Air pollution modeling: theories, computational methods and available software. Boston, Computational Mechanics Publications.